Engineering Systems to Study Cancer Metastasis

by

Stephen P. Cavnar

A dissertation submitted in partial fulfillment
of the requirements for the degree of
Doctor of Philosophy
(Biomedical Engineering)
in the University of Michigan
2015

Doctoral Committee:

Professor Gary D. Luker, Co-Chair
Professor Shuichi Takayama, Co-Chair
Professor Jennifer J. Linderman
Professor Allen Po-Chih Liu
Professor Jan P. Stegemann

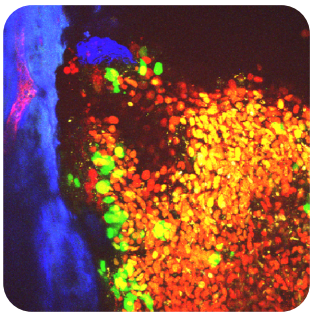

Dedication

This dissertation is dedicated to my family, particularly my mother and father.

To my mother, Mary Cavnar, you taught me creativity, compassion, and to always think outside of the box. Your unconditional love and support will forever be core to my success.

To my father, William Cavnar, you were my first and continuous mentor that sparked and kindled my interest in science, technology, and engineering. Your fateful and successful bouts with cancer drove my dedication towards engineering cancer.

To my brothers and sister, I am humbled to forever adventure in your footsteps.

Acknowledgements

Friends, Mentors, and Colleagues

I am fortunate to have enumerable people to thank from my nearly 27 years in Ann Arbor and 9 years at the University of Michigan. Many ever-encouraging friends, thoughtful mentors, and brilliant colleagues have guided me towards finishing this dissertation. Most of all, I thank my advisors for their patience and compassion while developing me as a scientist and a member of the community.

I would like to say thank you many times over to my co-advisor, Professor Shuichi Takayama. Your open door policy and faith in me as an undergraduate enabled my early and continued success. Your drive to connect people, ideas, and institutions has enabled my multi-faceted work and created an amazingly collaborative lab environment. I thank you for granting me so much latitude to pursue my interests while always asking me the "so-what" questions that are critical to graduate school success and beyond.

I am beyond grateful to my co-advisor, Professor Gary Luker. Your incredible and contagious energy for research, attention to detail, willingness to continually brainstorm new ideas, and daily mentorship have catalyzed my development as a scientist and person. In addition to incredible gains in scientific knowledge and technical knowhow, you imparted integrity, consistency, and enjoyment to my work. It was a pleasure to work side-by-side with you day in, day out.

Thank you to my unofficial lab and life advisor, Dr. Kathy Luker. Your honesty and passion for teaching have challenged me to be a better researcher and person. While gains in science were key, you brought always emphasized the fact that it's the people that matter. Thank you for making the Luker Lab a fun and family atmosphere.

Thank you to my entire committee, Gary Luker, Shuichi Takayama, Jennifer Linderman, Allen Liu, and Jan Stegemann. Your teamwork assisted me through the dissertation and defense preparation process and your diverse viewpoints have vastly improved my work.

To my friends and colleagues in the Luker Lab, we've spent so many hours problem-solving, taking on science headfirst, and getting to know one another. The hours spent in the A level of the BSRB will always hold a special place in my memories. I especially thank Amanda Stacer, Anna Ehrlich, Anna Salomonsson, Anne Gibbons, Annie Xiao, Aron Kandinov, Bradley Schmidt, Drew Rickelmann, Emma Salomonsson, Jack Liu, Joseph Fenner, Kaille Meguiar, Laura Mihalko, Mark Rudolf, Nathaniel Coggins, Paramita Ray, Paras Garg, Pranav Moudgil, Rahul Iyengar, Shashank Chitta, and Sudhu Srinivasan.

Thank you to the many current and former Takayama Lab members that were friends and mentors. I was never at loss for a local expert or someone to join in happy hour. I would like to recognize those of you that worked closely with me over the years, including but certainly not limited to Amy Hsiao, Andreja Jovic, Angela Dixon, Arlyne Simon, Bobak Mosadegh, Brendan Leung, Byoung Choul Kim, Cameron Yamanishi, Cedric Bathany, Chris Moraes, Chungmin Han, David Lai, Geeta Mehta, Hossein Tavana, Jason Kuo, John Frampton, Jonathan Song, Joong Yull Park, Joseph Labuz, Joshua White, Joyce Chiu, Madhuresh Sumit, Minsub Han, Nicholas Douville, Priyan Weerappuli, Ryuji Yokokawa,

Sasha Cai Lesher-Perez, Se Joong Kim, Steven Allen, Sung Jin Kim, Taisuke Kojima, Taylor Petri, Tommaso Bersano-Begey, Toshiki Matsuoka, Wansik Cha, Yi-Chung Tung, Yoko Kamotani, and Yusuke Torisawa.

Thank you to the many collaborators who have provided feedback and expertise for many facets of our work particularly Jennifer Linderman, Laura Chang, Judy Leopold, Joseph Dosch, amongst many others. In particular I would like to say thanks to Laura Chang, who has been a longtime classmate in high school, undergrad, and graduate school.

To those whose work is often unannounced but never unappreciated, there are so many logistics of lab and student life that you make so painless. In particular, I thank Julia Eussen, Maria Steele, Mayte Brown, Susan Bitzer, Susan Montgomery, and Tania Cunningham for their tireless efforts. Furthermore, I thank the many others that manage the inner-workings of Biomedical Engineering Department, Chemical Engineering Department, the Center for Molecular Imaging, and Department of Computational Medicine and Bioinformatics.

Last, but certainly not least, I want to acknowledge the love and support of my family and friends. Thank you for encouraging me through long hours, helping me overcome failures that are part of life, and celebrating many victories with me. There are more to come. Thank you again to my parents, Mary and William Cavnar. Thank you to my brothers and sister, Sam, Tom, Mike, Becky, Dave, Tim, and their families. I cannot imagine being part of a more intellectually challenging, extremely successful, and compassionate family. Thank you to my loving fiancée, Josselyn Frankiewicz, for providing daily inspiration to finish this dissertation and chase our lifelong dreams.

Funding, Publication, and Project-Specific Acknowledgements

Microfluidic Source-Sink Project: This work was supported by U.S. N.I.H. grants R01CA136553, R01CA136829, R01CA142750, and P50CA093990. S.P.C. was supported on Advanced Proteome Informatics of Cancer Training Grant # T32 CA140044 and an NSF Predoctoral Fellowship Project Grant # F031543. We thank ChemoCentryx for generously providing CCX771. This work was published in the Journal of *Integrative Biology.*

Systems for Three Dimensional Spheroid Imaging: This work was supported by U.S. N.I.H. grants R01CA170198, R01CA136553, R01CA136829, R01CA142750, and P50CA093990. S.P.C. was supported on Advanced Proteome Informatics of Cancer Training Grant # T32 CA140044. We thank Sasha Cai Lesher-Perez for discussion of spheroid cultures and their analysis and handling. We also thank Michael Deininger, from the University of Michigan, Medical Innovation Center for discussion of considerations for 3D prototyping. This work was published in the *Journal of Laboratory Automation.*

Bone Marrow Project: This work was supported by United States National Institutes of Health grants R01CA170198. SPC was supported by a NSF predoctoral fellowship F031543 and the Advanced Proteome Informatics of Cancer Training Grant # T32 CA140044. We thank Judith Leopold for her helpful discussion of this work. We thank Aaron Robida and the University of Michigan Flow Cytometry Core for help optimizing analysis of bone marrow samples. We thank the University of Michigan Biointerfaces Institute for access to the Seahorse Extracellular Flux Analyzer. We also thank Ulas Coskun from ISS for assistance on operation and analysis of frequency-domain FLIM data.

Table of Contents

List of Figures

List of Tables

List of Appendices

Abstract

Metastasis causes most late relapses and fatalities from cancer. Investigating mechanisms of metastasis and designing therapies to limit metastatic disease are challenging due to difficulties studying key events that occur before clinical detection, frequently involving small numbers of cells and intercellular interactions within three metastatic compartments (primary tumor, intravascular, and metastatic sites). By combining microfluidic, tissue engineering, and molecular imaging tools to screen therapies and analyze individual steps of metastasis, we further bridge the physiological gap between standard *in vitro* models, animal models, and human disease.

Firstly, we model how multiple cell types form and respond to chemotactic gradients that drive cell migration in a primary tumor. Using microfluidic tools to robustly pattern chemokine CXCL12 secreting cells, $CXCR7^+$ cells that scavenge this chemokine, and $CXCR4^+$ cells that migrate towards resulting gradients, we performed sensitivity analysis to identify functional combinations that are refractory to therapeutic inhibition. We found one high-matrix binding isoform (CXCL12-γ) to robustly promote chemotaxis even at low chemokine levels in the absence of scavenging cells and in the presence of a clinically approved inhibitor. Linking these findings to clinical physiology, we found this high-matrix-binding isoform to only be expressed in late stage breast cancer.

Secondly, we combine tissue engineering and molecular imaging tools to study the response of cancer cells in 3D tissue spheroids. We designed a platform to facilitate

handling and high resolution imaging of 384 well spheroids. Using this platform we developed a bone marrow spheroid model to recreate breast cancer quiescence and resistance to therapies. Using dual-colored bioluminescence imaging we simultaneously measured response of quiescent cancer and bone stromal cells to standard cytotoxic and targeted therapies. Using this strategy we identified therapeutic combinations that selectively eliminated quiescent cancer cells *in vitro* and entirely eliminated bone marrow metastases in mice. We also used this system to visualize metabolic gradients in bone marrow spheroids and measure cancer and stromal response to metabolic perturbations.

Combining microfluidic, tissue engineering, and molecular imaging tools as described herein can improve development of better models that recreate in vivo physiology and allow development of patient-specific therapies that prevent or eliminate metastatic disease.

Chapter One: Systems to Study Cancer Metastasis

1.1 Introduction and Challenges to Studying Metastasis

Cancer is the second leading killer in developed countries, accounting for nearly 1 in 4 deaths in the US (1). The yearly incidence rate of cancer has declined for men (0.6%) but was stable for women. Mortality rates have decreased more rapidly than yearly incidence (1.8% and 1.6% for men and women, respectively) in part due to earlier detection and improved therapies. Mismatched decrease in incidence and mortality shows that more people are living as cancer survivors, which puts the onus on limiting cancer relapse and limiting treatment toxicity. Although these factors are critical to most cancers, we focus on breast cancer. To reduce recurrence of cancer and limit treatment toxicity, we highlight three challenges, including 1) personalized therapy, 2) elimination/prevention of metastasis and relapse, and 3) development of therapies that eliminate cancer but spare normal cells. In this dissertation we aim to develop engineering systems that begin to address these challenges via drug development and mechanistic understanding.

Firstly, treatment must move towards personalized therapies that consider factors including genetic diversity and unique microenvironments that house each cancer cell. Towards personalized therapy, successful effort has been dedicated to defining phenotypic sub-types, their associated risk, and optimized treatment regimens (2, 3). However, recent studies show that even within a single tumor, plurality and plasticity of these classifications may complicate clinical usefulness of these markers (3, 4). Heterogeneous tumor

microenvironments complicate understanding of these phenotypes but also offer novel opportunities for therapy (5). Engineering models of tumor and metastatic microenvironments must capture such biological heterogeneity to better screen for drugs targeting patient-specific disease.

Secondly, we must understand how to entirely prevent and/or eliminate metastatic disease. In breast cancer, distinct relapse peaks occur at roughly 1, 5, and 10 years after diagnosis, and adjuvant therapy substantially diminishes the first of these peaks (Fig. 1.1) (6, 7). These findings suggest metastatic quiescent/dormant cells are refractory to standard cytotoxic therapies, persist for many years, and return to growth after years. Mathematical modeling of a subset of these data suggest prior to clinically detectable relapse at primary sites, tumor cells grow rapidly for ~30 weeks, despite average regression free survival of ~65 weeks (range 19-316 weeks) (8). This model indicates a period of tumor dormancy followed by return to rapid growth. Difficulty monitoring single or clusters of metastatic cells, their quiescent microenvironment, and triggers of their regrowth necessitates experimental models that capture these phenotypes.

Thirdly, we must therapeutically approach the first two challenges in a way that targets cancer cells but spares normal organ function, limits off-target toxicities, and minimizes long-term treatment effects. Treatment of cancers is often terminated due to cardiovascular, renal, and other systemic cytotoxicities. In part these challenges are being met by development of less cytotoxic therapies that are specific to cancer cells and spare normal tissues. The objective of selectively targeting cancer cells necessitates experimental models that include “normal” cells as a therapeutic reference to benchmark “patient” health.

From a practical standpoint meeting these challenges require more comprehensive understanding of the processes of cancer metastasis from primary disease to metastatic outgrowth and how to therapeutically limit them. Progress in such understanding has been hindered due to a paucity of experimental systems that recreate the physiology of cancer metastasis, allow monitoring of rare metastatic events, and/or allow screening of therapies against metastatic steps. The aim of this dissertation is to engineer systems that model steps of metastatic disease that are clinically and experimentally difficult to observe. These systems must better replicate *in vivo* physiology/complexity, allow analysis of very rare cellular events, and facilitate screening for drugs that selectively eliminate cancer cells but spare normal cells. In order to meet these challenges, we utilize tissue engineering tools to bridge the dimensionality gap between *in vitro* assays and *in vivo* physiology, as summarized in Fig. 1.2. Increasing dimensionality refers to the following characteristics: physical (2D vs 3D environments), temporal (endpoint, time point, and continuous observation; short- and long-scale), and biological complexity (multiple cell types, secreted factors, receptor status, etc). We employ diverse tools including: genetic engineering, tissue engineering, multi-modal molecular imaging, microfluidics, and manufacturing of tissue culture tools, amongst others. These tools span multi-scale interactions, from intracellular dynamics, to single cells, small metastases, larger tumors, and animal models. Using these systems we seek to understand how biological systems operate as a whole to create metastatic phenotypes and how we can intervene within these processes.

1.2 Compartments of the Metastatic Cascade

To inform design of systems to study cancer metastasis, we have to first understand the metastatic cascade and challenges associated with each step. Generally speaking, there are three major compartments in which cancer cells exist: the primary site, intravascular compartment, and metastatic sites at multiple organs (Fig. 1.3) (9, 10). Drivers of the metastatic cascade have been verbalized as the "seed and soil" hypothesis, which reflects the characteristics of robust cancer cells exiting a primary tumor, surviving the "elements" throughout the blood stream, and cultivating fertile organ environments for persistence/growth (11). This hypothesis suggests organ-specific metastasis to be an active process, rather than due to circulation-based probability. This simplification considers unidirectional flow of cancer cells (primary to secondary sites), but the order of metastatic steps and the directionality is widely debated. One recent study provided evidence that metastasis is a process in flux, where cancer cells flow to-and-from primary and secondary sites starting at early stages of carcinogenesis (12). This finding suggests the need for experimental models that reproduce primary, intravascular, and secondary steps in metastasis to analyze early, rare cell events that govern metastasis. The engineering challenge is to develop tissue-engineering models to analyze and target few cells operating within multi-cellular microenvironments of these three metastatic compartments. Here we break down a simplified view of the steps within each compartment.

1.2.1 Primary Tumor Microenvironment

Despite seemingly localized disease, upwards of 60% of patients have disseminated tumor cells in other organs, suggesting cancer cells exit the primary tumor early in tumor

formation (13). The primary tumor microenvironment involves multiple cytokine and nutrient gradients that evolve from interactions between cancer cells and associated support cells. As a tumor outgrows it's infrastructure, gradients of nutrients and waste form (14, 15) (Fig. 1.3A). Nutrient limitations (oxygen, carbon, nitrogen sources) and increased waste (lactate, etc) cause many changes in the tumor microenvironment, including: modifying the expression patterns at the core of these tumors, increased reactive oxygen species and sensing thereof, up-regulation/stabilization of hypoxia inducible factor (HIF1α) (16), increased secretion of cytokines (CXCL12, VEGF, etc) (17), and recruitment of immune and vascular endothelial cells, via cytokines/chemokines (18-20). Together these compensatory effects and resultant gradients aid the growth and exit of cancer cells from the primary tumor. Although many studies focus on the primary tumor microenvironment, model systems are lacking to consider how multi-cell type interactions evolve gradient formation and eventual tumor dissemination. Instead, most studies of nutrient and cytokine gradients apply non-physiological, fixed, exogenous gradients. However, systems are needed to study what multi-cellular phenotypes cause gradient formation and sensing.

Here we use microfluidics and spheroid systems to recreate aspects of gradient formation in a primary tumor and use these findings to study system-level impact of therapies. Firstly in Chapter 2, we utilize a microfluidic device to initialize and observe interactions between multiple cells types that participate in gradient formation of the chemokine (chemotactic sub-class of cytokine) CXCL12 (21). Utilizing this device we perform sensitivity analysis to understand interdependence of chemokine production, scavenging, sensing, and inhibition. In Chapter 3 we leverage a hanging drop 3D spheroid culture system to develop an advanced handling/imaging system for spheroids (22). Using

this spheroid analysis system in Chapters 4 and 5, we extend our ability to perform relatively high throughput two-photon microscopy imaging of cancer cells in 3D bone marrow spheroids. In the latter chapter, we use optical metabolic imaging to monitor metabolic gradients in 3D bone marrow spheroids.

1.2.2 Intravascular Compartment

As with detecting onset of primary disease due to small tumor size, it is more difficult to monitor even fewer cells that follow gradients in the primary tumor and intravasate into the vascular compartment (Fig. 1.3A-C). For example, reports of number of circulating tumor cells in blood show enormous variability (0 to 23,618, with average and SD = 84 ± 885), where such rarity and diversity complicates our ability to monitor the intravascular compartment even in animals (23). More so, cancer cells account for less than 1 cell per 10^5-10^6 mononuclear cells, and only a fraction are viable and capable of metastatic outgrowth (24). Recent work has improved our ability to study these intravascular steps via capture of circulating tumor cells (23, 25). However, the link between disease progression, response to therapy, and the existence of circulating tumor cells is improving, but still unclear (26, 27). In part, difficulties with capturing circulating tumor cells may be attributed to plasticity and heterogeneity of cell-surface expression for antibody- or size/stiffness-based capture. Additionally, it is difficult to decouple circulating tumor cells flowing from the primary tumor cells, secondary sites, and their longevity in the bloodstream. Therefore, recreating the physiology of intravascular interactions of cancer cells may provide insight towards capturing, eliminating, and/or decreasing metastatic capacity of circulating tumor cells.

In order to properly study the intravascular steps of cancer metastasis, several biochemical factors, biomechanical flow factors, and multi-cellular interactions must be considered (28, 29). Firstly, cancer cells may exit the primary tumor in isolation, in cancer cell clusters, and/or with associated fibroblasts or platelets (30-32). Once in the circulation, tumor cells must associate with platelets and other blood factors to improve viability, deform through small blood vessels, sense supportive organ environments, and maintain adhesion-independent viability (33-35). Finally, cancer cells must sense supportive organ environments, contact vascular walls, decelerate, firmly adhere, and extravasate. These processes occur under shear forces and biochemical stimuli within the blood stream, which complicates development of physiolocigal models. Therefore, physiological models of the intravascular compartment must include these multi-cellular interactions, biomechanical factors, biochemical factors, and collectively recreate diverse cancer functions.

Although not the focus of this dissertation, we have previously have advanced tissue-engineering tools to study the intravascular compartment of cancer metastasis (36). Using this microfluidic system we interfaced shear flow of breast cancer cells with organ-specific endothelial compartments and measured intravascular adhesion of cancer cells (36). We found basolateral activation of endothelial cells was more important than receptor-ligand interactions on the circulating tumor cells for promoting firm adhesion. Further studies have extended this model to consider perfusable 3D vascular models and the extravasation of cancer cells into various organ environments (37-40).

1.2.3 Metastatic Sites

Up to 60% patients with locally contained breast tumors harbor disseminated tumor cells in their bone marrow (13) and these cells may contribute to late relapse that is largely unaffected by adjuvant chemotherapy (6, 7). These results suggest that early in tumor formation, cancer cells successfully follow gradients out of the primary tumor, survive the circulatory compartment, and colonize secondary sites early in the tumor formation process. Bias towards particular organs (lung, liver, brain, and bone marrow) suggests that within a particular organ environment more cancer cells arrive, have supported growth once there, and/or are protected from therapy. Here we focus on the microenvironment that supports cancer cell growth, protection from cytotoxic therapies, and/or quiescence in metastatic sites.

The organ microenvironment and the molecular subtype of cancer dictate the aggressiveness of malignant cells in metastatic sites, which vary from indefinitely quiescent to immediately proliferating. There are two definitions for quiescence, either cellular quiescence or balanced proliferation and death of a micro-metastases. Single cells enter cellular quiescence and stop dividing by locking in G1 and/or exiting into G0 states of the cell cycle. Unlike rapidly growing metastases that are more susceptible to existing cytotoxic therapies, quiescent metastases are often protected from standard chemotherapeutic drugs. In part the lack of therapies that successfully target quiescent cancer cells is due to our model bias towards studying rapidly dividing cancer cells in a dish. Few systems reproduce the quiescent phenotypes of cancer cells in metastatic bone marrow sites (37, 41). Capturing the complex interactions that govern metastatic growth and/or quiescence is critical to developing therapies to limit cancer fatalities and relapse.

There is no one-size-fits-all model for metastatic sites in cancers, as organ-to-organ and within-organ variability create enumerable combinations of cells, structures, etc. As a starting point we highlight the metastatic diversity of bone marrow, particularly due to the commonality of this site for metastasis of multiple cancers (breast, prostate, pancreas, non-small cell lung, and melanoma) (13, 42), and heterogeneity of this organ in support of cancer cell growth versus quiescence. Generally there are two critical niches within the bone marrow that differently support expansion or maintenance of hematopoietic stem and cancer cells: the endosteal niche and the perivascular niche. These two niches contain many mesenchymal stromal, vascular, and immune cells (43). Several recent models begin to capture the 3D structure and/or cellular heterogeneity of the bone marrow (44-46). However, these studies are lacking in throughput and/or are limited in the ability to monitor viability of stromal cells, cancer cells, and their underlying cellular status (45, 46).

Here we leverage long-term bone marrow spheroid cultures to recreate quiescent and growing populations of metastatic cancer cells *in vitro*. In Chapter 4 we develop these growing and quiescence co-culture models, validate a dual-colored luciferase imaging strategy to capture relative viability of cancer and stromal cells and utilize fluorescence imaging to observe cell cycle status of cancer cells. Using this strategy we identified a drug combination that selectively eliminated quiescent cancer cells *in vitro* and completely eliminated bone marrow metastases in mice. In Chapter 5, we extend this bone marrow model in order to study metabolic interactions that support a quiescent cancer phenotype. We use multiple strategies to image and perturb the metabolic environment produced by different bone marrow stroma types, including frequency-domain fluorescence lifetime

imaging of endogenous metabolic fluorophores, molecular intervention, extracellular flux assays, and bioluminescence imaging.

1.3 Engineering Extracellular, Biomechanical, and Metabolic Sensing

Within each of the three metastatic compartments, cancer cells rely on integration of extracellular signals, biomechanical signaling, and metabolic sensing that are often poorly replicated *in vitro*. Standard tissue culture often employ 2D mono-cultures, a surplus of growth factors (serum), non-physiological rigid plastic substrates (47), and a pathologic surplus of metabolic intermediates (glucose, glutamine, etc). However, *in vivo* situations are uniquely 3D, involving numerous interacting cell types, non-rigid biological substrates, and dynamic levels/gradients of cytokines and metabolic intermediates. In order to better capture the integration of these three factors and improve dimensionality (physical and biological, Fig. 1.2), we use a combination of microfluidic and 3D tissue engineering technologies to model metastatic steps. Successfully engineered model systems will integrate extracellular signals, biomechanical signaling, and metabolic sensing to capture rare cellular events and predict *in vivo* responses, including metastatic tendencies, expression profiles, and drug sensitivities. Here we examine advantageous and opportunities using both microfluidic and 3D tissue engineering technologies to model metastasis.

1.3.1 Microfluidic Technologies

Microfluidic technologies facilitate precise fluidic delivery of reagents (growth factors, metabolites, cells) in order to finely tune control and surveillance of multi-scale cellular events. In particular, microfluidic devices produce highly defined and predictable

extracellular gradients to study chemotaxis of cells towards varying shapes, magnitudes, and combinations of gradients (48, 49). Although highly defined, microfluidic gradients often do not recreate the cellular and physical heterogeneity of *in vivo* physiology. *In vivo* gradients occurs in endocrine, paracrine, and autocrine fashions, which reflect systemic-, local-, and auto-signaling environments (50). Additionally, chemokines often are scavenged by receptors and sequestered on extracellular surfaces by proteoglycans, both of which change the kinetics, dynamics, and magnitudes of gradients (51-53). These complex interactions collectively regulate gradient formation, movement of cells *in vivo*, and must be considered in developing experimental systems.

Improved microfluidic manufacturing techniques are beginning to better recreate these complexities by including multiple cell types, structural arrangements of tissues, and interfaces between molecules, cells, and different organ environments. For example, incorporating flexible, porous membranes within a PDMS device recreates the aveolar interface and mechanics of lungs (54). Additionally, continuous flow between multiple separate organ compartments provided a pharmacokinetic-pharmacodynamic model for drug development (55). In this dissertation we build upon a previously developed microfluidic device (56) to understand how three populations of cells interact with each other and their environment to form and respond to a gradient (21).

1.3.2 3D Tissue Engineering Technologies

Improvements to 3D culture techniques facilitate modeling the biomechanics and mass-transfer limitations of *in vivo* tissues. Integration of biomechanical and biochemical sensing is improved in 3D culture systems (57). For example, gradients of glucose, lactate, and hypoxic factors have been recreated using 3D spheroid systems (15). Additionally,

using 3D systems better recreates *in vivo*-like growth rates (58) and drug sensitivity of tumor cells (59). Four main strategies are used for 3D cell culture techniques, including matrix-independent cultures (spheroids) (60), hydrogel-based cultures (61-63), rigid scaffold-based structures (64), and *ex vivo* organoid cultures (65). While improved synthetic chemistry and manufacturing techniques have aided development of hydrogel and scaffold-based cultures, their wide adoption for high throughput analysis has been hindered by cost, complexity, and assay robustness. Spheroids have gained popularity with recent studies describing simple, high throughput formation of uniform spheroids using hanging drop and low attachment tissue culture plates (66, 67). As these culture systems improve to increase throughput, diversity of cell types, and amenability to standard assays, their popularity will grow for studying tumor and metastasis microenvironments.

In Chapter 3 we build upon development of the 384 hanging drop spheroid array (66, 67) to enable improved analysis and imaging of spheroids (22). Additionally, in Chapters 4 and 5 we capture biochemical, biomechanical, and metabolic effects within multiple co-culture models of quiescent cancer and bone marrow stromal cells. We found different microenvironments to promote cancer cell quiescence or growth, differences in drug susceptibility, and to reflect *in vivo* responses of bone metastases to combination therapies.

1.3.3 Combined Microfluidic and 3D Approaches

Combinations of microfluidic technologies and 3D tissue technologies allow integrated control and surveillance of extracellular signaling, biomechanical stimuli, and metabolic pathways. For instance, within microfluidic cell-laden hydrogels, VEGF gradients and interstitial flow have been shown to govern formation of perfusable vessels *in vitro*

(68, 69). Building on these studies, similar systems have incorporated different underlying organ systems and observed cancer cell adhesion, extravasation, and growth (37, 38). The progression towards "human-on-a-chip" will continue with improvements to microfluidic and 3D technologies, including physiological arrangement of cells, inclusion of additional organ environments, and adaptation to primary cells. The goal of such combined approaches is to replicate normal and pathologic interactions between multiple organ compartments and to screen for drugs that spare the former but eliminate the latter.

1.4 Molecular Imaging Tools to Study Multi-scale Cell Interactions

To observe interactions between multiple receptor-ligand pairs and cell combinations across multiple time-scales and physical dimensions, we employ multi-modal imaging techniques. Each imaging modality has advantages and disadvantages in terms of ease of use, observation timing and scale, and interpretation. These techniques involve two-photon microscopy of fluorescent proteins and endogenous fluorescence (70, 71) and bioluminescence flux (72), which rely on radiant and chemical excitation, respectively. Together bioluminescence and fluorescence imaging provide complementary information about the location, abundance, and status of cells *in vitro* and *in vivo*.

1.4.1 Fluorescence Imaging

We use two-photon microscopy for optical metabolic imaging and imaging engineered fluorophores. The balance between energy-efficient oxidative metabolism and less efficient (often hypoxic) glycolytic metabolism is important to growth and quiescence of both cancer cells and hematopoietic stem cells. Label-free optical metabolic imaging utilizes both intensity-based and frequency-domain lifetime imaging of spectrally

separated fluorescent NADH and FAD metabolites (73, 74). Intensity provides information about abundance and lifetime describes the local environment of the fluorophore. Shifts of levels and lifetimes of these molecules indicate relative glycolytic and oxidative metabolism. Intensity-independent lifetime analysis allows for analysis of metabolic gradients at depth in both 3D tissue cultures and *in vivo.* We also use two-photon microscopy to image the abundance and location of engineered fluorescent receptor fusions (75), cell cycle protein fusions (76), and cytoplasmic fluorophores for cell tracking. Two-photon microscopy allows capture of subcellular and population-scale measures both *in vitro* and cancer foci *in vivo*. Microscopy throughput and time scales are limited by the acquisition times, frame stability, and difficulties with photo bleaching. Engineered fluorophores are also amenable to flow cytometry analysis of population-based variability.

1.4.2 Bioluminescence Imaging

We use multiple bioluminescence reporters to study ligand-receptor kinetics, *in vivo* location and abundance of metastatic foci, *in vitro* abundance of cells. Using complementary luciferase fragments fused to extracellular or intracellular ligands, we can measure receptor-receptor interactions (77) and ligand-receptor signaling events *in vivo* and *in vitro* (77-81). Using bioluminescence fusions of *Gaussia* luciferase, we sensitively measure the secretion and uptake of chemokines (82). We also use dual-colored luciferase imaging to spectrally separate competing receptor-based interactions and/or multiple cell types (83-85). Using bioluminescence we also track the metastatic location of cancer cells *in vivo* and the relative abundance of cancer and stromal cells *in vitro.*

We use complementary bioluminescence and fluorescent imaging to qualitatively and quantitatively assess abundance, location, and status of both cells and molecular

species. For instance, we use bioluminescence to measure growth versus quiescence and viability in response to drugs for cancer cells in bone marrow spheroid cultures and *in vivo.* Subsequent fluorescence imaging reveals microscopic location and cell cycle status cancer cells *in vitro* and *in vivo.* Since fluorescence and bioluminescence are non-overlapping imaging modalities they facilitate multiplexing and imaging of multiple sub-cellular, cellular, population, and whole animal imaging scales. We use both imaging modalities throughout this dissertation.

1.5 Figures

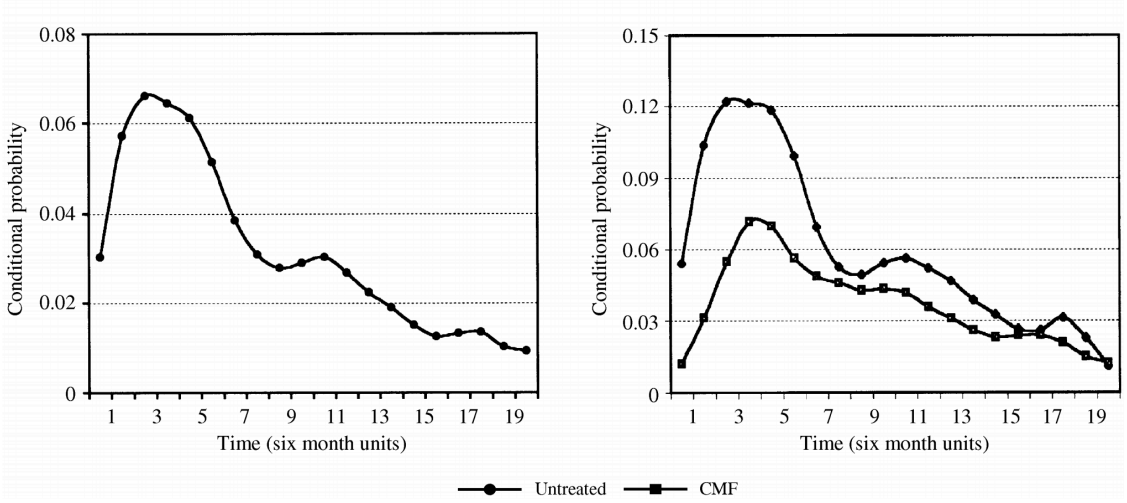

Figure 1.1. Conditional probability of relapse for breast cancer patients. These plots represent the hazard function (conditional probability) of relapse events at (a) any site for 1173 breast cancer patients with mastectomy. For (b) distant metasteses showed a similar relapse profile, with the first peak dampened for treatment with mastectomy alone or adjuvant chemotherapy (CMF = cyclophosphamide, methotrexate and fluorouracil) and mastectomy. These data are reprinted from Demicheli (6).

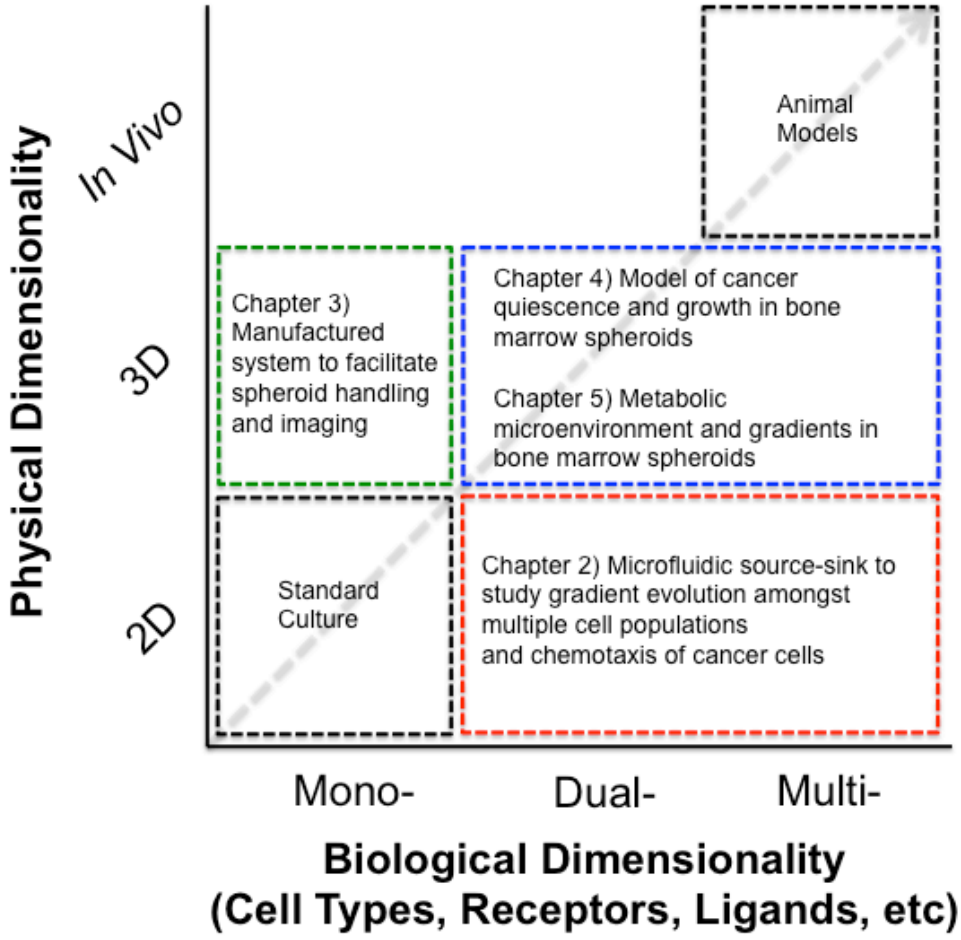

Figure 1.2. Physical and biological dimensionality of experimental models. The goal of experimental model systems is to provide the minimally complex model that best represents *in vivo* physiology. There are two axes by which we can increase the complexity of experimental *in vitro* systems: physical dimensionality (Y-axis: 2D, to 3D, towards *in vivo*) or the biological complexity (X-axis: mono-, to dual-, and multi-interactions). Biological complexity refers to the number of interacting experimental components, including cell types, receptor-ligand pairs, etc). The projects contained in this thesis bridge the experimental gap (gray arrow), between standard 2D mono-cultures, and *in vivo* physiology within animal models.

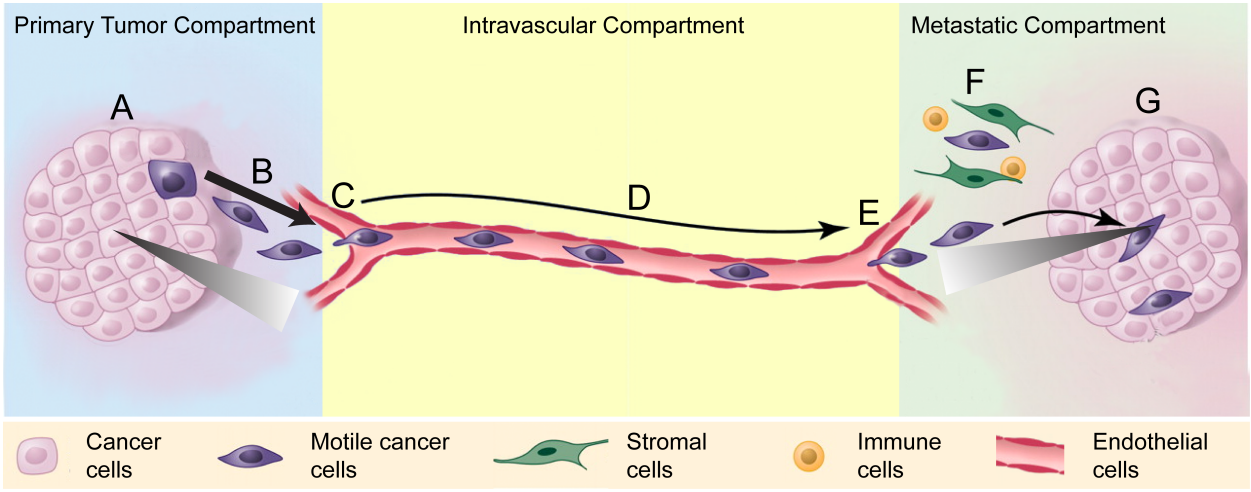

Figure 1.3. Overview of the metastatic cascade. Metastatic cancer cells follow a progression through primary tumor, intravascular, and metastatic compartments. Throughout growth of the (A) primary tumor, metabolic and cytokine gradients are formed towards and away from the vascular compartment (represented by the graded gray triangle). Transformed cancer cells follow gradients to (B) degrade the basement membrane, invade the interstitial space, and migrate towards the vascular compartment. After (C) intravasating into the intravascular compartment, cancer cells must survive (D) circulation, evade immune response, and survive non-adhesive stimuli. Note immune response is critical in primary, circulatory, and metastatic compartments despite being depicted only at metastatic sites. Circulating cancer cells subsequently may (E) adhere to the endothelium and extravasate into underlying organ environment. Within a metastatic site, cancer cells (F) find or create a microenvironment that supports proliferation or survival in a quiescent state. Cancer cells in metastatic sites may remain quiescent indefinitely (F) or (G) grow into large metastatic foci. For both (F) quiescent cancer cells housed with organ-specific stroma or in (G) growing metastatic foci, gradients of metabolites and cytokines are also critical to regulating movement, quiescence, drug resistance, and/or growth. This figure is modified from work by Chaffer and Weinberg (9).

1.6 References

1. Siegel R, Ma J, Zou Z, & Jemal A (2014) Cancer statistics, 2014. *CA: a cancer journal for clinicians* 64(1):9-29.
2. Kennecke H*, et al.* (2010) Metastatic behavior of breast cancer subtypes. *Journal of clinical oncology* 28(20):3271-3277.
3. Stingl J & Caldas C (2007) Molecular heterogeneity of breast carcinomas and the cancer stem cell hypothesis. *Nat Rev Cancer* 7(10):791-799.
4. Marusyk A, Almendro V, & Polyak K (2012) Intra-tumour heterogeneity: a looking glass for cancer? *Nat Rev Cancer* 12(5):323-334.
5. Junttila MR & de Sauvage FJ (2013) Influence of tumour micro-environment heterogeneity on therapeutic response. *Nature* 501(7467):346-354.
6. Demicheli R (2001) Tumour dormancy: findings and hypotheses from clinical research on breast cancer. *Seminars in Cancer Biology*, (Elsevier), pp 297-306.
7. Brackstone M, Townson JL, & Chambers AF (2007) Tumour dormancy in breast cancer: an update. *Breast Cancer Res* 9(3):208.

8. Demicheli R, Terenziani M, & Bonadonna G (1998) Estimate of tumor growth time for breast cancer local recurrences: rapid growth after wake-up? *Breast Cancer Res Treat* 51(2):133-137.
9. Chaffer CL & Weinberg RA (2011) A Perspective on Cancer Cell Metastasis. *Science* 331(6024):1559-1564.
10. Barcellos-Hoff MH, Lyden D, & Wang TC (2013) The evolution of the cancer niche during multistage carcinogenesis. *Nat Rev Cancer* 13(7):511-518.
11. Fidler IJ (2003) The pathogenesis of cancer metastasis: the'seed and soil'hypothesis revisited. *Nature Reviews Cancer* 3(6):453-458.
12. Kim M*, et al.* (2009) Tumor self-seeding by circulating cancer cells. *Cell* 139(7):1315-1326.
13. Alix-Panabières C, Riethdorf S, & Pantel K (2008) Circulating tumor cells and bone marrow micrometastasis. *Clinical Cancer Research* 14(16):5013-5021.
14. Helmlinger G, Yuan F, Dellian M, & Jain RK (1997) Interstitial pH and pO2 gradients in solid tumors in vivo: high-resolution measurements reveal a lack of correlation. *Nature medicine* 3(2):177-182.
15. Hirschhaeuser F*, et al.* (2010) Multicellular tumor spheroids: an underestimated tool is catching up again. *J Biotechnol* 148(1):3-15.
16. Semenza GL (2002) HIF-1 and tumor progression: pathophysiology and therapeutics. *Trends in molecular medicine* 8(4):S62-S67.
17. Santiago B*, et al.* (2011) CXCL12 gene expression is upregulated by hypoxia and growth arrest but not by inflammatory cytokines in rheumatoid synovial fibroblasts. *Cytokine* 53(2):184-190.
18. Carmeliet P & Jain RK (2000) Angiogenesis in cancer and other diseases. *Nature* 407(6801):249-257.
19. Balkwill F & Mantovani A (2001) Inflammation and cancer: back to Virchow? *The Lancet* 357(9255):539-545.
20. Semenza G (2013) Cancer–stromal cell interactions mediated by hypoxia-inducible factors promote angiogenesis, lymphangiogenesis, and metastasis. *Oncogene* 32(35):4057-4063.
21. Cavnar S*, et al.* (2014) Microfluidic source-sink model reveals effects of biophysically distinct CXCL12 isoforms in breast cancer chemotaxis. *Integrative Biology*.
22. Cavnar SP, Salomonsson E, Luker KE, Luker GD, & Takayama S (2013) Transfer, Imaging, and Analysis Plate for Facile Handling of 384 Hanging Drop 3D Tissue Spheroids. *Journal of laboratory automation*:2211068213504296.
23. Allard WJ*, et al.* (2004) Tumor cells circulate in the peripheral blood of all major carcinomas but not in healthy subjects or patients with nonmalignant diseases. *Clinical Cancer Research* 10(20):6897-6904.
24. Ross AA (1993) Detection and viability of tumor cells in peripheral blood stem cell collections from breast cancer patients using immunocytochemical and clonogenic assay techniques. *Age (vs)* 25(39):40-49.
25. Eliane J-P*, et al.* (2008) Monitoring serial changes in circulating human breast cancer cells in murine xenograft models. *Cancer Research* 68(14):5529-5532.

26. Giordano A*, et al.* (2011) Circulating tumor cells in immunohistochemical subtypes of metastatic breast cancer: lack of prediction in HER2-positive disease treated with targeted therapy. *Annals of Oncology*.
27. Cristofanilli M*, et al.* (2004) Circulating tumor cells, disease progression, and survival in metastatic breast cancer. *New England Journal of Medicine* 351(8):781-791.
28. Chambers AF, Groom AC, & MacDonald IC (2002) Metastasis: Dissemination and growth of cancer cells in metastatic sites. *Nat Rev Cancer* 2(8):563-572.
29. Konstantopoulos K, Kukreti S, & McIntire L (1998) Biomechanics of cell interactions in shear fields. *Adv Drug Deliv Rev* 33(1-2):141-164.
30. Molnar B, Ladanyi A, Tanko L, Sréter L, & Tulassay Z (2001) Circulating tumor cell clusters in the peripheral blood of colorectal cancer patients. *Clinical Cancer Research* 7(12):4080-4085.
31. Duda DG*, et al.* (2010) Malignant cells facilitate lung metastasis by bringing their own soil. *Proceedings of the National Academy of Sciences* 107(50):21677-21682.
32. Aceto N*, et al.* (2014) Circulating tumor cell clusters are oligoclonal precursors of breast cancer metastasis. *Cell* 158(5):1110-1122.
33. Mueller BM, Reisfeld RA, Edgington TS, & Ruf W (1992) Expression of tissue factor by melanoma cells promotes efficient hematogenous metastasis. *Proceedings of the National Academy of Sciences* 89(24):11832-11836.
34. Palumbo JS*, et al.* (2002) Spontaneous hematogenous and lymphatic metastasis, but not primary tumor growth or angiogenesis, is diminished in fibrinogen-deficient mice. *Cancer Research* 62(23):6966-6972.
35. Nieswandt B, Hafner M, Echtenacher B, & Männel DN (1999) Lysis of tumor cells by natural killer cells in mice is impeded by platelets. *Cancer Research* 59(6):1295-1300.
36. Song J*, et al.* (2009) Microfluidic endothelium for studying the intravascular adhesion of metastatic breast cancer cells. *PLoS One* 4(6):e5756.
37. Bersini S*, et al.* (2014) A microfluidic 3D in vitro model for specificity of breast cancer metastasis to bone. *Biomaterials* 35(8):2454-2461.
38. Jeon JS*, et al.* (2015) Human 3D vascularized organotypic microfluidic assays to study breast cancer cell extravasation. *Proceedings of the National Academy of Sciences* 112(1):214-219.
39. Zervantonakis IK*, et al.* (2012) Three-dimensional microfluidic model for tumor cell intravasation and endothelial barrier function. *Proceedings of the National Academy of Sciences* 109(34):13515-13520.
40. Chen MB, Whisler JA, Jeon JS, & Kamm RD (2013) Mechanisms of tumor cell extravasation in an in vitro microvascular network platform. *Integr Biol (Camb).* 5(10):1262-1271. doi: 1210.1039/c1263ib40149a.
41. Ghajar CM*, et al.* (2013) The perivascular niche regulates breast tumour dormancy. *Nature cell biology* 15(7):807-817.
42. Leong SP & Tseng WW (2014) Micrometastatic cancer cells in lymph nodes, bone marrow, and blood: Clinical significance and biologic implications. *CA Cancer J Clin.* 64(3):195-206. doi: 110.3322/caac.21217. Epub 22014 Feb 21215.
43. Morrison SJ & Scadden DT (2014) The bone marrow niche for haematopoietic stem cells. *Nature* 505(7483):327-334.

44. Torisawa Y-s, *et al.* (2014) Bone marrow–on–a–chip replicates hematopoietic niche physiology in vitro. *Nature Methods*.
45. Weisberg E, *et al.* (2012) Using combination therapy to override stromal-mediated chemoresistance in mutant FLT3-positive AML: synergism between FLT3 inhibitors, dasatinib/multi-targeted inhibitors and JAK inhibitors. *Leukemia* 26(10):2233-2244.
46. McMillin DW, *et al.* (2010) Tumor cell-specific bioluminescence platform to identify stroma-induced changes to anticancer drug activity. *Nature medicine* 16(4):483-489.
47. Berthier E, Young EW, & Beebe D (2012) Engineers are from PDMS-land, Biologists are from Polystyrenia. *Lab on a Chip* 12(7):1224-1237.
48. Saadi W, Wang S, Lin F, & Leon N (2006) A parallel-gradient microfluidic chamber for quantitative analysis of breast cancer cell chemotaxis. *Biomed Microdevices* 8(2):109-118.
49. Mosadegh B, *et al.* (2007) Generation of stable complex gradients across two-dimensional surfaces and three-dimensional gels. *Langmuir* 23(22):10910-10912.
50. Lodish H, *et al.* (2000) Overview of extracellular signaling.
51. Weber M, *et al.* (2013) Interstitial Dendritic Cell Guidance by Haptotactic Chemokine Gradients. *Science* 339(6117):328-332.
52. Kreuger J, Salmivirta M, Sturiale L, Giménez-Gallego G, & Lindahl U (2001) Sequence analysis of heparan sulfate epitopes with graded affinities for fibroblast growth factors 1 and 2. *Journal of Biological Chemistry* 276(33):30744-30752.
53. Stoler-Barak L, *et al.* (2014) Blood vessels pattern heparan sulfate gradients between their apical and basolateral aspects. *PLoS ONE* 9(1):e85699.
54. Huh D, *et al.* (2010) Reconstituting Organ-Level Lung Functions on a Chip. *Science* 328(5986):1662-1668.
55. Sung JH, Kam C, & Shuler ML (2010) A microfluidic device for a pharmacokinetic–pharmacodynamic (PK–PD) model on a chip. *Lab on a Chip* 10(4):446-455.
56. Torisawa Y, *et al.* (2010) Microfluidic platform for chemotaxis in gradients formed by CXCL12 source-sink cells. *Integr Biol (Camb)* 2(11-12):680-686.
57. Griffith LG & Swartz MA (2006) Capturing complex 3D tissue physiology in vitro. *Nat Rev Mol Cell Biol* 7(3):211-224.
58. Hsiao A, *et al.* (2009) Microfluidic system for formation of PC-3 prostate cancer co-culture spheroids. *Biomaterials* 30(16):3020-3027.
59. Loessner D, *et al.* (2010) Bioengineered 3D platform to explore cell–ECM interactions and drug resistance of epithelial ovarian cancer cells. *Biomaterials* 31(32):8494-8506.
60. Mehta G, Hsiao AY, Ingram M, Luker GD, & Takayama S (2012) Opportunities and challenges for use of tumor spheroids as models to test drug delivery and efficacy. *J Control Release.* 164(2):192-204. doi: 110.1016/j.jconrel.2012.1004.1045. Epub 2012 May 1018.
61. Fischbach C, *et al.* (2007) Engineering tumors with 3D scaffolds. *Nat Methods* 4(10):855-860.
62. Debnath J, Muthuswamy SK, & Brugge JS (2003) Morphogenesis and oncogenesis of MCF-10A mammary epithelial acini grown in three-dimensional basement membrane cultures. *Methods* 30(3):256-268.

63. Lee GY, Kenny PA, Lee EH, & Bissell MJ (2007) Three-dimensional culture models of normal and malignant breast epithelial cells. *Nature Methods* 4(4):359-365.
64. Fong ELS, *et al.* (2013) Modeling Ewing sarcoma tumors in vitro with 3D scaffolds. *Proceedings of the National Academy of Sciences* 110(16):6500-6505.
65. Shamir ER & Ewald AJ (2014) Three-dimensional organotypic culture: experimental models of mammalian biology and disease. *Nature Reviews Molecular Cell Biology* 15(10):647-664.
66. Hsiao AY, *et al.* (2012) 384 hanging drop arrays give excellent Z-factors and allow versatile formation of co-culture spheroids. *Biotechnol Bioeng.* 109(5):1293-1304. doi: 1210.1002/bit.24399. Epub 22011 Dec 24320.
67. Tung Y, *et al.* (2011) High-throughput 3D spheroid culture and drug testing using a 384 hanging drop array. *Analyst* 136(3):473-478.
68. Song J & Munn L (2011) Fluid forces control endothelial sprouting. *Proc Natl Acad Sci U S A* 108(37):15342-15347.
69. Song JW, Bazou D, & Munn LL (2012) Anastomosis of endothelial sprouts forms new vessels in a tissue analogue of angiogenesis. *Integrative Biology* 4(8):857-862.
70. Hoffman RM (2005) The multiple uses of fluorescent proteins to visualize cancer in vivo. *Nat Rev Cancer* 5(10):796-806.
71. Ntziachristos V, Bremer C, & Weissleder R (2003) Fluorescence imaging with near-infrared light: new technological advances that enable in vivo molecular imaging. *European radiology* 13(1):195-208.
72. Contag CH & Ross BD (2002) It's not just about anatomy: in vivo bioluminescence imaging as an eyepiece into biology. *Journal of magnetic resonance imaging* 16(4):378-387.
73. Skala MC, *et al.* (2007) In vivo multiphoton microscopy of NADH and FAD redox states, fluorescence lifetimes, and cellular morphology in precancerous epithelia. *Proceedings of the National Academy of Sciences* 104(49):19494-19499.
74. Walsh AJ, *et al.* (2013) Optical metabolic imaging identifies glycolytic levels, subtypes, and early-treatment response in breast cancer. *Cancer Research* 73(20):6164-6174.
75. Ray P, *et al.* (2012) Carboxy-terminus of CXCR7 regulates receptor localization and function. *Int J Biochem Cell Biol* 44(4):669-678.
76. Sakaue-Sawano A, *et al.* (2008) Visualizing Spatiotemporal Dynamics of Multicellular Cell-Cycle Progression *Cell* 132(3):487-498.
77. Luker K, Gupta M, & Luker G (2009) Imaging chemokine receptor dimerization with firefly luciferase complementation. *FASEB J* 23(3):823-834.
78. Luker G, *et al.* (2002) Noninvasive imaging of protein-protein interactions in living animals. *Proc Natl Acad Sci USA* 99(10):6961-6966.
79. Luker K, *et al.* (2004) Kinetics of regulated protein-protein interactions revealed with firefly luciferase complementation imaging in cells and living animals. *Proc Natl Acad Sci USA* 101(33):12288-12293.
80. Luker K, Gupta M, & Luker G (2008) Imaging CXCR4 signaling with firefly luciferase complementation. *Anal Chem* 80(14):5565-5573.
81. Luker G & Luker K (2011) Luciferase protein complementation assays for bioluminescence imaging of cells and mice. *Methods Mol Biol* 680:29-43.

82. Luker K*, et al.* (2012) *In vivo* imaging of ligand receptor binding with *Gaussia* luciferase complementation. *Nat Med* 18(1):172-177.
83. Coggins NL*, et al.* (2014) CXCR7 Controls Competition for Recruitment of β-Arrestin 2 in Cells Expressing Both CXCR4 and CXCR7. *PLoS ONE* 9(6):e98328.
84. Mezzanotte L*, et al.* (2011) Sensitive Dual Color In Vivo Bioluminescence Imaging Using a New Red Codon Optimized Firefly Luciferase and a Green Click Beetle Luciferase. *PLoS ONE* 6(4):e19277.
85. Villalobos V*, et al.* (2011) Dual-color click beetle luciferase heteroprotein fragment complementation assays. *Chem Biol* 17(9):1018-1029.

Chapter Two: Microfluidic source-sink model reveals effects of biophysically distinct CXCL12-isoforms in breast cancer chemotaxis

2.1 Summary

Chemokines critically regulate chemotaxis in normal and pathologic states, but there is limited understanding of how multicellular interactions generate gradients needed for cell migration. Previous studies of chemotaxis of CXCR4+ cells toward chemokine CXCL12 suggest the requirement of cells expressing scavenger receptor CXCR7 in a source-sink system. We leveraged an established microfluidic device to discover that chemotaxis of CXCR4 cells toward distinct isoforms of CXCL12 required CXCR7 scavenging only under conditions with higher than optimal levels of CXCL12. Chemotaxis toward CXCL12-β and -γ isoforms, which have greater binding to extracellular molecules and have been largely overlooked, was less dependent on CXCR7 than the more commonly studied CXCL12-α. Chemotaxis of CXCR4+ cells toward even low levels of CXCL12-γ and CXCL12-β still occurred during treatment with a FDA-approved inhibitor of CXCR4. We also detected CXCL12-γ only in breast cancers from patients with advanced disease. Physiological gradient formation within the device facilitated interrogation of key differences in chemotaxis among CXCL12 isoforms and suggests CXCL12-γ as a biomarker for metastatic cancer.

2.2 Introduction

Chemotaxis of cells along a concentration gradient is essential for normal development, tissue homeostasis, and pathogenesis of diseases including metastatic cancer, atherosclerosis, and multiple sclerosis (1-6). Chemotaxis controls trafficking of normal stem cells, and there are ongoing efforts to enhance homing of stem cells to injured tissues for regenerative medicine (7, 8). The source-sink model of chemotaxis is one common process to generate gradients and drive cell migration *in vitro* and *in vivo* (9-11). The balance between chemotactic molecule secretion (source) and degradation (sink) critically determines gradient profiles and responsiveness of migrating cells (10-19). Recent studies also demonstrate that gradients of chemokine bound to the extracellular matrix, rather than soluble molecules, drive chemotaxis (20) by increasing local concentrations of chemokine, limiting degradation, and enhancing presentation to receptors (21). Therapeutic targeting of source-sink chemotaxis as an emergent phenotype of multiple cells, receptors, and microenvironmental factors rather than a singular molecular event provides flexibility in drug targets but requires evaluation of the entire integrated system.

Chemokine CXCL12-α and its receptors CXCR4 and CXCR7 are a prominent example of source-sink chemotaxis in normal physiology and pathologic conditions (22-24). CXCR7 functions as a scavenger receptor, controlling availability of CXCL12 by removing it from the extracellular space and degrading it (10-19). Two recent studies highlight that CXCL12 secretion and CXCR7 scavenging are obligate partners in generating sustained, local gradients of CXCL12-α *in vivo*, allowing cells with CXCR4 to migrate toward CXCL12 source cells (25, 26). Loss of CXCR7 in both zebrafish and an *in vitro* device we developed prevented normal migration of CXCR4+ cells due to loss of chemokine gradients and/or

desensitization of CXCR4 from elevated levels of CXCL12-α (10, 11). While prior studies show that CXCR7 is required for CXCR4-dependent migration toward CXCL12-α, these studies overlook the importance of variable interactions of CXCL12 isoforms with receptors and the extracellular space. Studies of CXCL12 isoforms in chemotaxis have been particularly challenging because only the α-isoform efficiently stimulates chemotaxis in conventional transwell assays, while other isoforms require supraphysiologic concentrations to drive cell migration (27).

To investigate interrelationships between a source-sink model and binding of chemotactic molecules to extracellular surfaces, we used our established microfluidic source-sink model of CXCL12, CXCR4, and CXCR7 (Fig. 2.1). We tested three of the six naturally expressed CXCL12-isoforms (α, β, and γ, common to humans, mice, and rats) that span low-to-high affinities for receptors CXCR4, CXCR7, and the extracellular environment (28-30). Secreted forms of these CXCL12 isoforms share a common N-terminal 68 amino acid core that comprises the entirety of CXCL12-α. CXCL12-β and -γ have four and 30 additional amino acids at the C-termini, respectively. C-termini of CXCL12-β and -γ are enriched with basic amino acids that enhance interactions with negatively-charged extracellular molecules and surfaces (27, 29, 31). In particular, CXCL12-γ binds to major components of the extracellular matrix, such as the glycosaminoglycan heparan sulfate, with more than two orders of magnitude greater affinity than the most commonly studied isoform, CXCL12-α. However, CXCL12-γ binds with lower affinity to receptor CXCR4, and scavenging by CXCR7 is also less efficient. Association of chemotactic molecules with extracellular components also may enhance chemotaxis by increasing local concentrations of chemokine, favoring oligomerization that may be necessary for chemokine activity,

limiting proteolytic degradation, and enhancing presentation to receptors (21). These opposing interactions between CXCL12-isoforms and extracellular surfaces or receptors produce marked disparities in bound versus soluble concentrations of each isoform (27, 29). Effects of different isoforms of CXCL12 on gradient formation and chemotaxis within physiological source-sink environments are unknown.

Using unique capabilities of our microfluidic device, we discover that levels of secreted CXCL12 isoforms dictate the requirement for CXCR7-dependent scavenging in chemotaxis of CXCR4+ cells. CXCR7-scavenging is necessary for chemotaxis of CXCR4 cells under conditions with higher levels of CXCL12, while reducing amounts of CXCL12 partially rescues chemotaxis without functional scavenging by CXCR7. Even at concentrations 10 to 20-fold lower, we also show for the first time *in vitro* that CXCL12-γ, an isoform with highest binding to the extracellular environment, drives chemotaxis of CXCR4 cells to an extent similar to CXCL12-β and greater than CXCL12-α. Exploiting capabilities of this device for drug testing, we demonstrate that AMD3100, the only FDA-approved inhibitor of CXCR4, fails to entirely block migration of CXCR4+ cells toward CXCL12-β or -γ. Moreover, we show for the first time expression of CXCL12-γ in primary human breast cancers and suggest that this isoform is associated with metastatic disease. These results demonstrate that intrinsic biophysical and biochemical differences among chemokine isoforms regulate cell migration and emphasize the need for drugs that more effectively target CXCL12-β and -γ.

2.3 Experimental Methods

2.3.1 Plasmid construction

The CXCL12 fusions to Gaussia luciferase (GLuc) were generated by PCR or gene synthesis (supplied in pIDTSMART-Kan blunt, Integrated DNA Technologies) as indicated in Supplemental Table S1, products 1,3-5. These were constructed in pEGFP-N1 digested with XhoI and NotI to remove the EGFP open reading frame. A Gly/Ser linker and EcoRI site were included between the CXCL12 and GL open reading frames. The CXCL12-GL fusions were amplified by PCR with appropriate primers shown in Table S1, products 9,10, and inserted into the PacI sites of FU650W (constructed from FUGW as described (32)) for product 9 or the XbaI and NotI sites of pLVX-EF1α-IRES-mCherry (Clontech) for product 10. Unfused versions of CXCL12 isoforms and secreted Gaussia luciferase were amplified with primers as indicated in Table S1, products 2, 6-8 and cloned into the XbaI and NotI sites of pLVX-EF1α-IRES-mCherry (note that NheI and XbaI have compatible cohesive ends). Vector FUAcGFP-nucW was generated by amplifying nuclear-targeted AcGFP from pAcGFP1-Nuc (Clontech) as indicated in Table S1, product 11, and cloned into the PacI site of FUGW.

2.3.2 Stable cell lines

We transduced MDA-MB-231 cells with lentiviral vectors described above to generate populations of cells expressing fusions of CXCL12-α, β, or γ to GL with co-expressed fluorescent protein FP650 (33). Expression of FP650 and the IRES-linked mCherry enabled flow cytometry sorting and identification of cells within the microfluidic device. We previously described MDA-MB-231 cells stably transduced with CXCR4-GFP

(231-CXCR4) (34). To facilitate imaging and image analysis, we transduced 231 CXCR4 cells with FUAcGFP-nucW. We previously reported MDA-MB-231 cells stably transduced with CXCR7-GFP (231-CXCR7) or CXCR7-Δ322-GFP (231- CXCR7-Δ322) (16). We used MDA-MB-231 cells stably expressing click beetle green and red luciferase complementation reporters for association of β-arrestin 2 and CXCR7 or CXCR4, respectively (35). These reporter cell lines are comparable to the firefly luciferase complementation systems we previously have described for these protein interactions (36, 37).

2.3.3 Murine tumor models

We implanted 2 x 105 E0771 mouse breast cancer cells stably expressing firefly luciferase and GFP along with 1 x 105 immortalized mouse mammary fibroblasts (gift of Harold Moses, Vanderbilt) orthotopically into 4th inguinal mammary fat pads of syngeneic C57Bl/6 mice (Taconic). We harvested 8-10 mm diameter tumors and extracted RNA using Trizol (Life Technologies) according the manufacturer's directions. We also generated human breast cancer xenografts by implanting 5 x 10^5 231-CXCR4 cells co-expressing firefly luciferase into 4th inguinal mammary fat pads of NSG mice (15). We extracted RNA from these tumors as described above.

2.3.4 Western blot analysis

We measured phosphorylation of AKT as we have previously described (38). Synthetic CXCL12 isoforms for this assay were purchased from R&D Systems.

2.3.5 Secreted CXCL12 ELISA analysis

We contracted the University of Michigan Cancer Center Immunology Core to perform CXCL12 ELISA per specifications for R&D Systems CXCL12-α ELISA. We

previously demonstrated complementary ELISA- and bioluminescence-based CXCL12 measurement (38).

2.3.6 Quantitative RT-PCR for CXCL12-isoforms

We measured mRNA levels of CXCL12-α, β, or γ fusions to Gaussia luciferase in stably transduced MDA-MB-231 cells by qRT-PCR using PCR primers common to all isoforms and SYBR Green detection: 5' tgcccttcagattgttgcacg 3' and 5' ctccaggtactcttggatccac 3', based on our prior protocol (32). To analyze expression of CXCL12 isoforms in mouse tumors and bone marrow, we extracted RNA with Trizol reagent (Life Technologies) and further purified RNA with a column-based kit and on-column treatment with DNaseI (Qiagen). We performed qRT-PCR as described above with isoform-specific primers: common forward primer 5'-tgcccttcagattgttgcacg-3', α-reverse primer 5'-ggctgttgtgcttacttgtttaaagc-3', mouse β-reverse primer 5'-ctgactcacacctctcacatcttg-3', human β-reverse primer 5'-ggcgtctgaccctctcacatcttg-3', and γ-reverse primer 5'-gaactagtttttccttttctgggcagcc-3'. The primers are the same for human and mouse except for the reverse primer for CXCL12-β. We used a cDNA array of normal human breast tissue and breast cancers (Origene, Breast Cancer cDNA Array II). Human primers were used for xenograft tumors and the human cDNA array. For both cells and tissues, we amplified GADPH as a control and quantified data as ΔCt values. We defined tissues as positive for an isoform of CXCL12 based on amplification at <40 qRT-PCR cycles and appropriate size PCR product identified by gel electrophoresis.

2.3.7 Microfluidic device fabrication and preparation

We fabricated the microfluidic migration device as described previously (11). We used a top channel with 100μm depth instead of 200 μm. We patterned cells in three 200μm wide strips spaced 200 μm apart. For time course confocal imaging and for imaging of receptor localization within the device, we fabricated the microfluidic device with the total top layer thickness of ~2mm to allow imaging.

2.3.8 Microfluidic device experimental setup

We seeded cells as described previously (11). For treatment with AMD3100, we supplemented both the final batch of cells and parallel medium with 1 μM AMD3100 (Tocris) in DMEM with 10% FBS. Within an hour of seeding the final batch of cells (CXCR4-GFP), we imaged each device to match corresponding phase contrast and epifluorescence images. We matched parallel device conditions among isoforms, dilutions of secreting cells, and treatments for each run.

2.3.9 Bioluminescence imaging

We imaged fusions of CXCL12-isoforms to Gaussia luciferase and luciferase complementation between CXCR4 or CXCR7 and β-arrestin 2 as described previously (36-38).

2.3.10 Image acquisition and analysis

For time point analyses of cells in the microfluidic device, we acquired phase contrast and fluorescence images at 4 and 6 locations along the length of the device channel for t=0 and 24 hours, respectively (n=4-11 device setups per condition). We captured images using an inverted Olympus IX70 microscope with a 10X objective. We

developed a semi-automated NIH ImageJ (64bit) script to measure location of NLS-AcGFP tagged CXCR4+ cells relative to the channel boundaries (Supplemental Info). The script returned coordinates of each CXCR4+ cell based on NLS-GFP (fluorescence) relative to the matched channel boundaries (phase contrast). We measured the average position for each view field in the direction of the source cells. For time-lapse microscopy, we used a custom CO2 and temperature controlled stage for live-cell imaging with a 10X, 0.3 NA objective and upright confocal microscope (Olympus MPE Twin). For each CXCL12-isoform, we imaged a single view field of three separate device setups at 15-minute increments for 20 hours total. Using a modified ImageJ script, we measured position of cells over time. We imaged CXCR4-GFP localization in the microfluidic channel by confocal microscopy using a 60X, 1.0NA objective. We captured z-stack images (2.5μm increments) at 5 positions along the channel length and displayed representative z-compressions that were adjusted identically in parallel for demonstration (n = 2 devices per condition).

2.3.11 Transwell migration experiments

We performed transwell migration assays as reported previously(39). Briefly, we incubated 231-cells overexpressing CXCR4+ in transwells with equal levels of CXCL12-isoforms, based on Gaussia luciferase activity. We observed migrated cells based on crystal violet staining.

2.3.12 Statistical analysis

We made all plots and statistical comparisons using GraphPad Prism. We plotted time point data as mean ± standard error of the mean (S.E.M.). For time course data, we plotted the mean ± standard deviation (S.D.) of percentile lines, which we created in

Microsoft Excel. For all statistical comparisons of migration data we performed paired, two-sided statistical comparisons using the Mann-Whitney U-test (non-parametric) with exact p-values. For analysis of CXCL12-uptake we performed simple two-sided t-test. For analyses of bioluminescence complementation (Figs. 2.1, 2.3, A.6, and A.7) and CXCR4-GFP internalization over time (Fig. 2.4 E) we performed two-way ANOVA and post hoc Tukey multiple comparisons test within rows. For two-way ANOVA we used time as the row effect versus CXCL12-isoform or concentration for the column effect.

2.4 Results

2.4.1 Microfluidic source-sink-migration system

Using a multi-layered device (Fig. 2.1A), we patterned cells that secrete individual CXCL12 isoforms (source) in a geometrically defined location relative to MDA-MB-231 breast cancer cells expressing CXCR7 (CXCR7+, sink) or CXCR4 (CXCR4+, migrating cells) (Fig. 2.1B-D). In this device, intercellular interactions between source and sink cells generate chemotactic gradients in situ in the context of serum-containing medium and other molecules secreted by cells. We also emphasize that the only difference among source cells is the isoform of secreted CXCL12, so differences in chemotaxis of CXCR4 cells arise from distinct biologic effects of each isoform. The device allows us to quantify changes in position of all CXCR4+ cells through time lapse imaging (Fig. A.1) or endpoint analyses to give chemotaxis data as a pooled frequency distribution or mean position per view field (see Fig A.2 A-D or 2.1E-G, respectively, as examples). By changing the percentage of secreting cells mixed in with non-secreting cells, the system also tests the effect of changing the amount of source CXCL12 produced. We also analyzed the role of the

sink cells by either eliminating CXCR7 cells or by patterning cells expressing non-functional forms of CXCR7. CXCL12 conditions did not cause differences in growth in these settings based on the number of 231-CXCR4 cells uniformly doubling over 24 hours (data not shown).

2.4.2 Characterization of secreted Gaussia luciferase CXCL12-isoform-fusions

For the CXCL12-isoform secreting (source) cells we stably transduced MDA-MB-231 breast cancer cells with an isoform of CXCL12 fused to *Gaussia* luciferase (GLuc). We previously described that fusion of CXCL12-α to GLuc provides a sensitive, quantitative measure of chemokine levels without affecting ligand activity (38). We focused on CXCL12-α, -β, and -γ, the most common human isoforms and those shared with mice and rats (28). While we emphasized CXCL12 secretion by cancer cells, previous studies show that both malignant and stromal cells may secrete this chemokine (40, 41). We expressed CXCL12-isoforms using two different vectors (Fig. A.3), allowing us to create GLuc-fused and -unfused chemokines to demonstrate that fusion to GLuc retains biological activity of each isoform (Supplemental Results and Fig. A.3-5). We note that, despite only modest differences in mRNA levels, amounts of secreted CXCL12-γ were 10-fold lower than CXCL12-α and -β by GLuc activity and ELISA reactivity (Fig. A.2E-F). Although the polyclonal ELISA antibodies were developed against CXCL12-α, the assay detects the N-terminal core, which is common to all isoforms. Relatively lower amounts of secreted CXCL12-γ protein as compared with mRNA may reflect previously reported differences in intracellular trafficking of CXCL12-γ (42), and we have observed this effect with multiple vectors and cell types. GLuc-fused CXCL12-isoforms also signalled via AKT at comparable levels as synthetic isoforms based on our ELISA and GLuc concentration estimates (Fig.

A.5). Overall, these data allow us to quantitatively compare levels of CXCL12 isoforms secreted by source cells.

2.4.3 CXCL12-β and -γ have surprisingly high chemotaxis potency in an in vitro source-sink model

Chemotaxis of CXCR4+ cells toward CXCL12-γ was slightly more than CXCL12-β ($p<0.05$) and significantly more than CXCL12-α ($p = 0.0001$) after 24 hours (Fig 2.1E-G, comparison among 100% secreting conditions for each isoform with statistics not marked on plots). These results differ notably from transwell assays in which CXCR4+ cells show higher sensitivity migration toward cell-secreted or recombinant CXCL12-α (Fig. A.2G) (27, 43, 44). Rueda and colleagues previously showed a ten-fold higher concentration of CXCL12-γ was required to drive chemotaxis of CXCR4 cells to the same extent as CXCL12-α in transwells. However, their study required 100nM CXCL12-γ to promote chemotaxis, substantially higher than amounts expected *in vivo* or produced in our system. Using time-lapse microscopy we also show that CXCL12-γ induced more immediate and rapid migration of both leading and trailing edges, followed by continued migration comparable to sustained effects of CXCL12-α and -β (Fig. A.1B-D).

Chemotactic responses of CXCR4+ cells toward CXCL12 can show a bell-shaped curve with reduced effects at both high and low concentrations of chemokine (27). To evaluate such effects, we progressively reduced concentrations of CXCL12 by patterning lower percentages of CXCL12-secreting cells mixed with non-secreting parental cells while keeping the total number of cells in the source region constant ($p<0.0001$; Fig 2.2A-C). Chemotaxis toward CXCL12-α showed no significant peak before dropping off at 1% relative concentration. CXCL12-β elicited a clear bell-shaped response with peak

chemotaxis at 50% and 10% relative concentrations ($p<0.05$ and $p<0.0001$, respectively) (Fig 2.2B), indicating that 100% source cells produce a higher than optimal concentration of chemokine. Chemotaxis towards CXCL12-γ also showed no significant peak before dropping off at 1% ($p<0.0001$). To investigate mechanisms underlying greater responsiveness of CXCR4+ cells toward CXCL12-γ, we quantified activation of CXCR4 by recruitment of the cytosolic adapter protein β-arrestin 2, which is implicated in chemotaxis (45, 46). We treated cells expressing a luciferase complementation reporter for association of CXCR4 and β-arrestin 2 with increasing concentrations of recombinant CXCL12-α, -β, or -γ (36, 47). CXCL12-γ stimulated greater recruitment of β-arrestin 2 to CXCR4 than the other isoforms, potentially contributing to enhanced chemotaxis toward the γ-isoform (Fig 2.1H-J, A.6) (45, 46).

2.4.4 Inhibiting CXCL12-CXCR4 dependent chemotaxis

AMD3100 is a small-molecule competitive inhibitor of CXCL12-CXCR4 binding used clinically to mobilize hematopoietic stem cells (44, 48). Little is known about effects of AMD3100 against different isoforms of CXCL12. Using the microfluidic source-sink model, we found AMD3100 to be less effective than may be expected from transwell studies against just the α-isoform (Fig. 2.2A-C). While AMD3100 effectively eliminated chemotaxis in transwell assays with CXCL12-α (Fig A.2G), in the source-sink device CXCL12-β or -γ secreting cells still drove migration in the presence of AMD3100 ($p<0.0001$ and $p<0.01$, respectively for β- and γ-isoforms). These data indicate that even very low, physiologic levels of CXCL12-β or -γ may continue to drive detectable chemotaxis in the presence of a validated CXCR4 inhibitor.

2.4.5 Limited CXCR7-dependent scavenging of CXCL12-γ

Cells expressing wild-type CXCR7 internalized more CXCL12-α and -β than cells with either CXCR7-Δ322 ($p<0.005$ and $p<0.0001$ for α and β, respectively) or no CXCR7 ($p<0.0001$ for both α and β) (Fig. 2.3A). In cells with wild-type (WT) CXCR7, intracellular accumulation of CXCL12-α was highest and followed by -β, with only minimal CXCR7-dependent accumulation of CXCL12-γ relative to CXCR7-Δ322 or control cells without CXCR7 (Fig. 2.3A). This order was reversed for cells without CXCR7, suggesting that higher binding affinity of CXCL12-γ to glycosaminoglycans on cell membranes confers CXCR7-independent accumulation (Fig 2.3A inset). Likewise, a small molecule inhibitor of CXCL12 binding to CXCR7 (CCX771) decreased CXCR7-dependent internalization for CXCL12-α and -β, but not -γ (Fig. 2.3B). Accordingly, lower amounts of CXCL12-α and -β than -γ induced CXCR7-dependent recruitment of β-arrestin 2, which is involved in CXCR7 internalization, as determined by luciferase complementation (Fig. 2.3C-E, A.7) (16, 37). These data show inefficient scavenging of CXCL12-γ by CXCR7.

2.4.6 Levels of CXCL12 determine requirement for CXCR7 scavenging in chemotaxis

We previously demonstrated that CXCR7 functions as a sink to determine the magnitude and shape of a CXCL12-α gradient in our microfluidic device (11). To investigate to what extent CXCR7 scavenging is required for chemotaxis of CXCR4 cells, we used sink cells that does not internalize CXCL12 (16). When using high numbers of CXCL12 source cells, chemotaxis of CXCR4+ cells toward all CXCL12-isoforms decreased when CXCR7-Δ322 sink cells replaced WT-CXCR7 cells ($p<0.0001$) (Fig 2.4A-C). However, differences in chemotaxis between CXCR7-Δ322 and CXCR7-WT were substantially less with only 10% of the source cells producing CXCL12. For devices with CXCR7-Δ322 sink

cells, we observed greater chemotaxis when the relative concentration was 10% rather than 100% ($p<0.0001$). These data emphasize the dynamic balance between levels of CXCL12 secretion and CXCR7-dependent scavenging in CXCR4-dependent chemotaxis. CXCL12 scavenging by CXCR7 is required for chemotaxis of CXCR4+ cells at higher levels of chemokine, while functioning CXCR7 is less important for chemotaxis with lower levels of CXCL12.

Upon prolonged stimulation with CXCL12, CXCR4 internalizes and is degraded (15, 44). In our experiments, localization and fluorescence intensity of a CXCR4-GFP fusion protein in migrating cells could be used as metrics of CXCR4 signaling and desensitization (Fig 2.4D-E). Using CXCL12-β secreting cells as the source, we found significantly higher CXCR4-GFP internalization when the WT CXCR7 scavenging cells were replaced with the scavenging-deficient CXCR7-Δ322 cells ($p < 0.05$). Such CXCR4 internalization effects, however, were significantly mitigated when using a lower 10% relative concentration of CXCL12-β cells independent of WT or mutant CXCR7 sink cells (Fig. 2.4E). These results show that CXCR7-scavenging prevents degradation of CXCR4 and loss of chemotaxis under conditions with relatively higher levels of CXCL12. Conversely, by lowering the amount of CXCL12, migrating cells retain a signaling pool of CXCR4-GFP at the cell membrane and overall levels of receptor sufficient for chemotaxis even with CXCR7-Δ322 cells.

2.4.7 CXCL12-γ in primary breast tumors

To link our data to breast cancer biology *in vivo*, we analyzed expression of CXCL12-α, -β, and -γ in orthotopic breast tumor implants from syngeneic and human xenograft mouse models and a cDNA array from bulk tissues derived from normal breast and primary human breast cancers. We detected CXCL12-α, -β, and -γ in mouse tumors and with rank

order of frequency of expression being α > β > γ (Fig. A.8), based on the number of samples amplifying at <40 qRTPCR cycles. Despite quantitatively lower levels of CXCL12-β and γ-isoforms, nearly all samples had detectable signal. In human tissues, we detected transcripts for CXCL12-α and -β more consistently in human tissues (normal and tumor) as compared with the γ-isoform. CXCL12-β was expressed slightly more frequently in cancers. Remarkably, we detected CXCL12-γ only in primary tumors from patients with advanced disease (Table 2.1). We note that these data do not assign the cell type(s) in tumors that produce CXCL12 isoforms. While our microfluidic device emphasized secretion of CXCL12 by cancer cells, stromal cells in tumors also are sources of this chemokine (15, 40, 49).

2.5 Discussion

CXCL12 is a homeostatic chemokine that drives many finely tuned, dynamic physiologic and pathologic processes, necessitating multiple levels of regulation. Our study focuses on chemotaxis as a dynamic balance among chemokine secretion, endocytosis by sink cells, binding to extracellular surfaces, and regulating chemokine-sensing receptor numbers. These factors must all be included in models for screening therapeutic agents, as changing one has concerted effects on the entire system.

In the simplest conceptual model, secreted ligands freely diffuse from their source and create a concentration-dependent gradient according to Fick's law of diffusion. We highlight mechanisms that modify the shape and magnitude of this gradient in the extracellular space. CXCR7 removes and degrades CXCL12, which decreases local concentrations of chemokine and sharpens the chemokine gradient to facilitate migration (10, 13-16). The requirement for CXCR7 scavenging in chemotaxis of CXCR4 cells is

contingent upon levels of CXCL12. CXCR7 scavenging is particularly critical for chemotaxis of CXCR4 cells under conditions with relatively high levels of CXCL12. However, when source cells secrete only low levels of CXCL12, CXCR4 cells still migrate in the absence of CXCR7 scavenging, albeit at somewhat reduced efficiency. In devices with reduced numbers of source cells, cells retained sufficient CXCR4 at the cell surface to migrate in response to the CXCL12 gradient. These results highlight an essential balance in gradient formation between relative capacities of the source and sink to produce and scavenge ligand, respectively. Our data also, suggest that therapeutic targeting of CXCR7 in chemotaxis will be contingent on relative CXCL12 levels locally.

Although CXCR7 has been highlighted (25, 26) as a critical mediator of CXCL12 gradient formation and chemotaxis (25, 26), we emphasize CXCL12 isoforms as another largely overlooked mechanism for controlling gradient shape, local chemokine levels, and chemotaxis. CXCL12 exists as six human (α, β, γ, δ, ε, and ϕ) and three mouse and rat (α, β, and γ) isoforms, which are expressed in time and tissue-specific distributions during development and post-natal life (28-30). CXCL12 isoforms share 68 common amino-terminal amino acids, which comprise all of the most studied CXCL12-α isoform and contain one glycosaminoglycan-binding BBXB domain (B denotes basic and X denotes any amino acid, respectively). Other isoforms differ by addition of 1-41 largely basic amino acids to the carboxy-terminus, accounting for one and four additional BBXB motifs in CXCL12-β and -γ, respectively. Differences in carboxy-termini among isoforms alter biologic and biophysical properties of CXCL12, including binding affinities for receptors and extracellular matrix molecules and activation of downstream signaling (27, 29). In our model, despite adjusting the fraction of secreting cells to produce comparable levels of each

isoform, we established for the first time *in vitro* that CXCL12-γ maintains CXCR4 sensitization and chemotaxis despite low chemokine levels and in the presence of AMD3100. Interestingly, CXCL12-γ binds directly to CXCR4 with lower affinity than CXCL12-α or -β, and yet our results show it functions as a high "effective" or multivalent affinity ligand for both CXCR4 and cell surface proteoglycans in chemotaxis (27, 29). We posit two mechanisms for this observation. One is that that CXCL12-β and -γ form sharper gradients due to relatively increased surface adhesion, both to cell and device surfaces. This notion is supported by the lack of absolute requirement for CXCR7 scavenging cells to elicit chemotaxis. Another mechanism is that high affinity interactions between the more positively charged CXCL12-β and -γ and negatively charged cell surface proteoglycans increase local concentrations of chemokine to bind to CXCR4 and drive migration (50). As a result, these isoforms promote chemotaxis at low total abundance and effectively compete with inhibitor AMD3100 (See Appendix A Supplemental Discussion and Table A.2). By concentrating CXCL12 isoforms on cell surfaces, we propose that heparan sulfates function as stable co-receptors for CXCL12-isoforms and CXCR4, enhancing activation of CXCR4-β-arrestin 2 signaling and chemotaxis relative to other isoforms (29, 45, 46, 51-53).

While interactions between CXCL12 and glycosaminoglycans are necessary for optimal chemotactic responses to this chemokine, interrelationships among glycosaminoglycan binding, chemokine oligomers, and chemotaxis remain uncertain (50, 54). CXCL12 bound to heparan sulfates may form dimers at physiologic concentrations of chemokine (39, 55). CXCL12 monomers have been reported to preferentially stimulate chemotaxis in some studies, while others have determined that CXCL12 dimers comprise the more active species (39, 54, 56). Disparate results about potency of CXCL12 monomers

versus dimers in chemotaxis may be due to variable concentrations and presentations of chemokine and/or glycosaminoglycans in assays. Future studies adding heparan sulfates and other glycosaminoglycans to our device, combined with imaging reporters of dimers, may resolve this uncertainty (39).

With the caveat of small sample size, a provocative observation of our study is detection of CXCL12-α, -β, and -γ in human breast cancer with CXCL12-γ only present in primary tumors from patients with metastases to lymph nodes or other organs. This result underscores previous descriptions of alternative splicing as transformative mechanism in cancer (57) and supports further studies of CXCL12-γ as a biomarker for tumor microenvironments that promote metastasis. Similar to CXCL12, alternative splicing of vascular endothelial growth factor produces a functional range of short to long isoforms, with the longest and shortest having the highest and lowest heparan sulfate binding, respectively (58). However, in malignant transformation, alternative splicing switches towards expression of the more diffusible, short isoforms of VEGF in lung and colon cancers. Indeed, limited *in vivo* studies suggest that CXCL12-γ drives chemotaxis to a much greater extent than CXCL12-α or -β, but standard *in vitro* assays fail to capture this phenotype and instead show CXCL12-γ to be comparatively ineffective (27, 59). One study in mice with mutated carboxy-terminal BBXB domains showed exogenous delivery of CXCL12-γ better recruited endothelial progenitor cells and restored vascular repair after acute ischemia as compared with exogenous CXCL12-α (59). We further implicate CXCL12-γ beyond post-ischemic repair as a potential marker of advanced human breast cancer.

We identified interdependence between levels of CXCL12 isoforms and inhibition of chemotaxis with AMD3100. AMD3100 only partially inhibited chemotaxis toward all

isoforms with high levels of CXCL12, but the drug more effectively limited migration toward relatively lower amounts of CXCL12. However, even low levels of CXCL12-β or -γ drove CXCR4-dependent chemotaxis in the presence of AMD3100, suggesting that the drug may be less effective against isoforms other than α. Our results are consistent with prior work showing that 10-fold more AMD3100 is needed to block binding of CXCL12-γ to CXCR4 relative to CXCL12-α (44). As CXCL12-isoforms ostensibly confer signaling through the same CXCR4 binding site, AMD3100 should exhibit equal competitive inhibition of all isoforms. This point suggests that higher local concentrations of CXCL12-β and -γ effectively compete with AMD3100 for binding to CXCR4. Although we detected modest amounts of mRNA for CXCL12 isoforms in human cancers, these results suggest relatively few CXCL12-β and -β producing cells are required to drive migration. Shift of alternative splicing programs towards high potency CXCL12-β and -γ may enhance metastasis and drug resistance in advanced disease. Our results indicate the need for more potent agents to block chemotaxis in response to all isoforms of CXCL12.

Our device facilitates gradient formation in a dynamic and cell-autonomous way, unlike systems in which users introduce external gradients. The low, rising gradients in our device are less defined but more physiological than bolus doses in Boyden chambers and linear gradients generated in microfluidic systems. Nonetheless, we used several methods to quantify and perturb chemokine levels to understand their activities relative to reported dissociation constants for CXCL12-isoforms to their receptors. First, we quantified the maximal soluble level of chemokine with a combination of ELISA, *Gaussia* luciferase assays, and signaling/uptake assays. Second, we varied isoform levels, numbers of cells secreting an isoform, efficiency of CXCR7-dependent scavenging, and specific

inhibitor AMD3100. Using these strategies we defined different qualitative functional regimes of the source-sink components. Without improved real-time chemokine measurement techniques and substantial computational modeling of this complex system, it is difficult to dynamically quantitate the soluble and more importantly bound levels of chemokine. Nonetheless, our device offers middle ground between migration assays of varying complexity: standard Boyden chambers, three-dimensional hydrogel systems conditions (60), and *in vivo* physiology (61, 62).

Our device provides the first *in vitro* system that recapitulates observations in mouse models of enhanced chemotactic effects of CXCL12-β and -γ relative to α-isoforms (27, 63). Importantly, we emphasize that this device detects differences in chemotaxis among CXCL12 isoforms secreted in the context of other molecules secreted by source cells. Our results differ markedly from standard Boyden chamber migration assays in which CXCL12-α is most effective and cells migrate only in response to CXCL12-γ lacking cationic BBXB domains or very high concentrations of wild-type CXCL12-γ (27). We propose several differences between our device and Boyden chambers allow us to replicate CXCL12-β and -γ in physiological conditions. Boyden chamber assays expose cells acutely to high levels of CXCL12, which may cause rapid CXCR4 internalization and desensitization (44). We have shown that our device generates low, sustained gradients of CXCL12 that may prevent CXCR4 desensitization (11). Several studies suggest that low levels of CXCL12 "prime" cells for signaling by recruiting additional cell-surface CXCR4, as evidenced by increased HIV infection or β-arrestin 2 recruitment after pre-treatment with low amounts of CXCL12 (36, 43). The highly cationic C-terminus of CXCL12-β and -γ also confers greater non-specific binding to negatively-charged tissue culture plastic, which may remove these

chemokines from solution in standard Boyden chamber systems, altering the gradient profile and directionality. Binding of CXCL12 to the migration surface of our microfluidic device may contribute to gradient formation in the direction of CXCR4+ cell migration. Finally, observing migration along a longer distance in our device may be more representative of *in vivo* processes as compared to having cells squeeze through small pore over a very short distance in Boyden chambers (20). These and likely other factors allow our device to accurately reproduce *in vivo* chemotactic effects of CXCL12 isoforms, providing a facile system to investigate functions and therapeutic targeting of various isoforms in chemotaxis.

On the other end of assay complexity, extension of our cell-based source-sink model into three dimensions would better facilitate incorporation of glycosaminoglycans within a three dimensional hydrogel, and provide more *in vivo*-like invasion/chemotaxis (60). We expect that incorporating heparan sulphate proteoglycan chemistry within a hydrogel matrix will sharpen gradients and limit gradient length scales, particularly for ligands with high matrix affinity. However, our device highlights the cell-autonomous role in gradient formation due to ligand interactions with receptors, cell-surface proteoglycans, and the device surface. In three dimensional hydrogel systems ligand-matrix interactions dominate gradient formation. Nonetheless, understanding how source-sink interactions facilitate gradient and chemotaxis dynamics in the context of three-dimensional matrices and proteoglycans is an important next step to understanding *in vivo* physiology.

2.6 Conclusions

Our study provides new insights into the chemotactic microenvironment and interdependencies between CXCL12-secretion and bioavailability within the extracellular

space. The microfluidic device utilized in this work is the first cell culture system that reproduces enhanced chemotactic effects of CXCL12-γ reported in living animals. Interestingly, we found that few CXCL12 secreting cells were required to drive migration and that low levels of CXCL12 may largely bypass the need for CXCR7 to form chemotactic gradients and retain CXCR4 sensitization. These data suggest that even low levels of CXCL12, particularly CXCL12-β and -γ, may be relevant for driving chemotaxis *in vivo*. This device provides an ideal platform to identify mechanistic differences among CXCL12 isoforms in chemotaxis and identify new inhibitors that are effective against all isoforms of this chemokine. These studies suggest that the collective microenvironment should be considered a biomarker for metastatic cancer, including the distribution of CXCL12-isoforms and relative levels of CXCR4 and CXCR7.

2.7 Figures

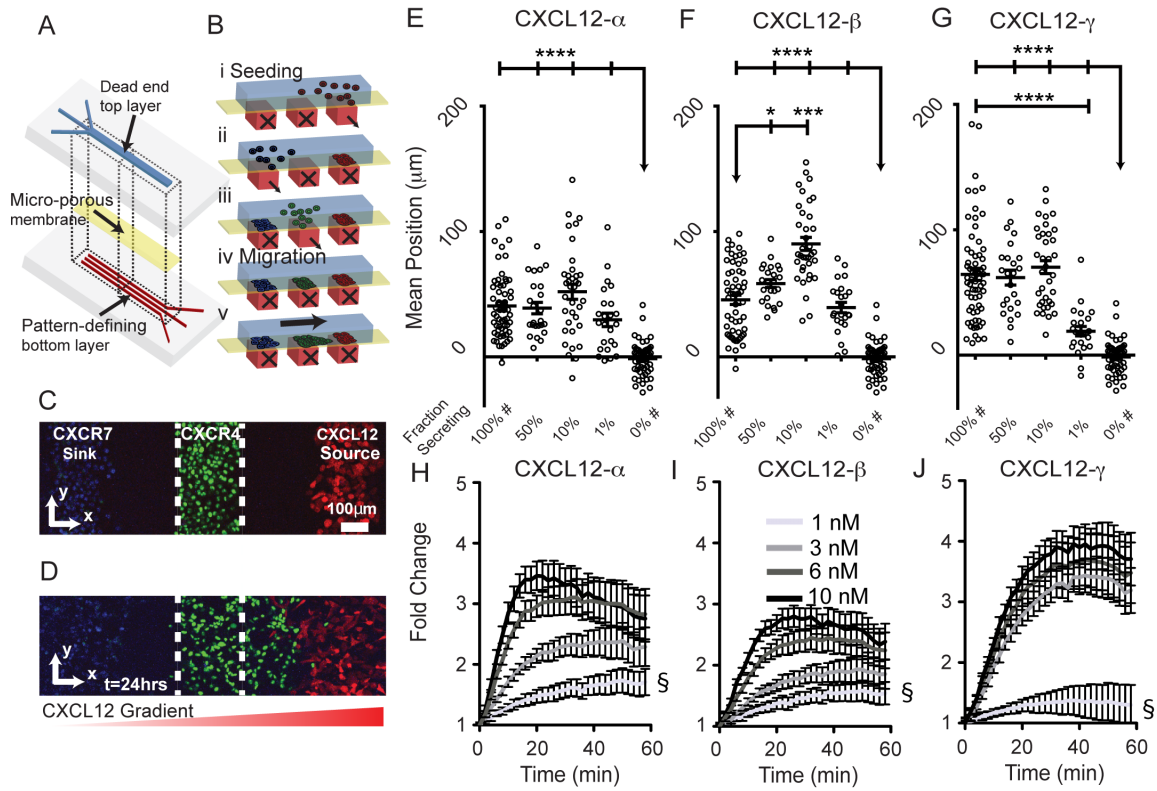

Figure 2.1. Microfluidic source-sink-migration device. *(A, B)* Schematic multi-layered microfluidic device fabrication and representation of patterned cell seeding. Controlled flow through bottom channels results in 200 μm wide cell patterns with 200 μm gaps. Parts i, ii, and iii depict stepwise addition of CXCL12-secreting cells, CXCR7+ cells, and CXCR4+ cells, respectively. Parts iv and v represent conditions before and after migration. *(C, D)* Representative confocal images of patterned cells in the device at t=0 (*C corresponds to B iv*) and after 24 hours (*D corresponds to B v*). The CXCL12 secreting cells co-express FP650 (red); CXCR4+ cells express NLS-AcGFP (green); and CXCR7+ cells are stained with Hoescht 33342 (blue). The dashed white line denotes channel boundaries that define the starting position. The graded red triangle below *(D)* denotes the gradient direction. *(E-G)* Average position of CXCR4+ cells after 24 hours of migration toward CXCL12-α, -β, or -γ. Each point represents the mean position of ~300±50 cells from 1 of 6 view fields from 10-11 devices. Fraction of secreting cells denotes the relative dilution of CXCL12-isoform secreting cells patterned with non-secreting cells. Data are shown as mean values ± S.E.M. (n=6 view fields for 4-11 devices per condition). The bars represent statistical comparison between pairs of conditions. The arrow denotes multiple paired comparisons to the same condition (*p<0.05, ***p<0.005, ****p<0.0001). Data for 100% and 0% secreting cells are marked (#) to designate the same data plotted for comparison in multiple figures. Matched conditions were performed in parallel. *(H-J)* Cells expressing a luciferase complementation reporter for association of CXCR4 and β-arrestin 2 were incubated with increasing equimolar concentrations of synthetic CXCL12-α, β, or γ. Data were graphed as mean values ± S.E.M. (n=4 measurements) from one of two representative experiments. Fold change in bioluminescence is relative to untreated cells at corresponding time points. The symbol § demarcates statistical differences by Tukey *post hoc* test between concentrations for the final time point. For CXCL12-α, 1nM is different from 6nM (p<0.01) and 10 nM (p<0.01). For CXCL12-β, 1nM is different from 6nM (p<0.05) and 10 nM (p<0.01). For CXCL12-γ, 1nM is different from all other concentrations (p<0.0001). Comparisons between isoforms are in supplemental information (Fig. A.6).

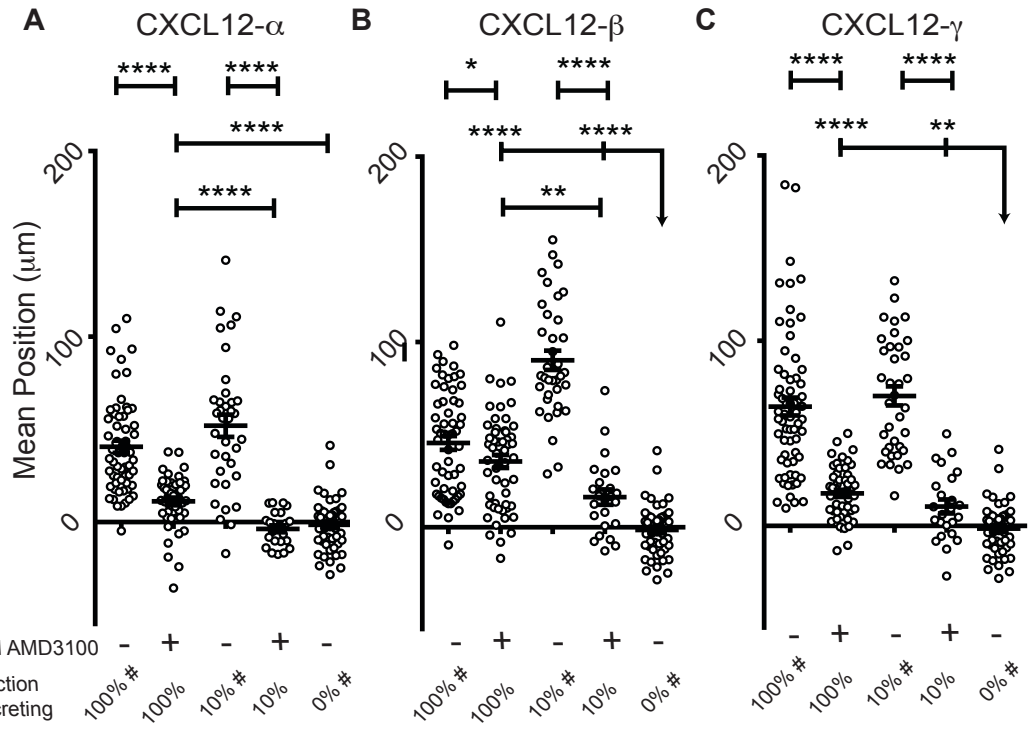

Figure 2.2. AMD3100 limits migration of CXCR4+ cells toward CXCL12 isoforms. *(A-C)* Positions of CXCR4+ cells within migration devices were determined after 24 hours of migration in the absence or presence of 1 μM AMD3100. Data are plotted as average positions ± S.E.M. (n=6 view fields each for 4-11 devices per condition, similar to previous figures). Fraction of secreting cells denotes the relative percent of CXCL12-isoform secreting cells relative to control cells patterned in the source position. The bar represents the statistical comparison between pairs of conditions. The arrow denotes multiple paired comparisons to the same condition (*p<0.05, **p<0.01, ****p<0.0001). Data for 100%, 10%, and 0% secreting cells are marked (#) to designate the same data plotted for comparison in multiple figures. Matched conditions were performed in parallel.

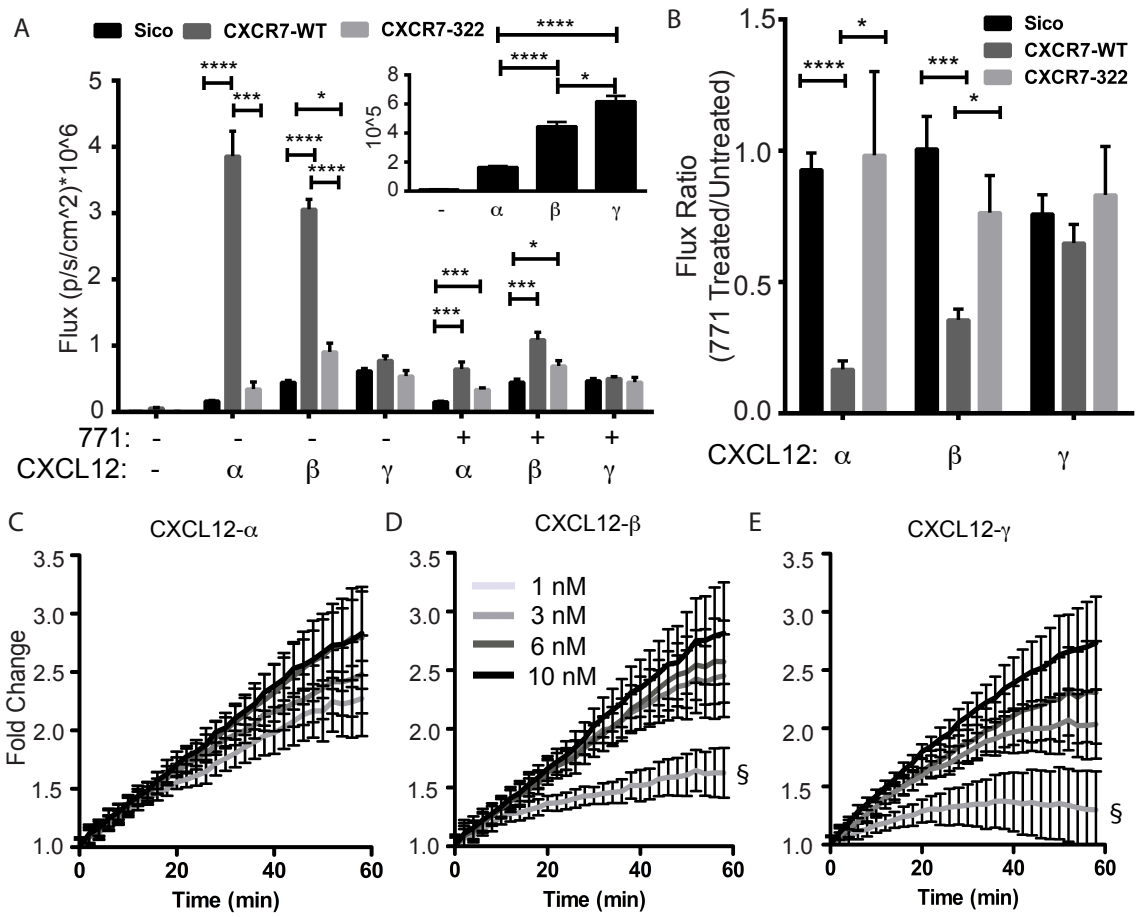

Figure 2.3. CXCR7-dependent scavenging of CXCL12-isoforms. *(A)* 231 cells expressing CXCR7-GFP-WT, CXCR7-Δ322-GFP or no CXCR7 were incubated for 1 hour with equal levels (based on *Gaussia* luciferase activity) of cell-secreted CXCL12- α, β, or γ. Following incubation and acid wash to remove extracellular CXCL12, we measured internal *Gaussia* luciferase activity to quantify internalization of CXCL12. Photon flux values are reported as mean ± S.E.M. (n=4 measurements) from one of three representative experiments. The inset highlights only CXCL12-isoforms binding to CXCR7-negative 231-Sico cells. *(B)* Ratio of internalized bioluminescence signal *(A)* between cells incubated with inhibitor of CXCL12 binding to CXCR7 (771) relative to untreated cells. Statistical demarcations compare data between bars (* $p < 0.05$, ***$p<0.005$, **** $p<0.0001$). *(C-E)* Cells expressing a luciferase complementation reporter for association of CXCR7 and β-arrestin 2 were incubated with increasing equimolar concentrations of synthetic CXCL12-α, β, or γ. Data were graphed as mean values ± S.E.M. (n=4 measurements) from one of two representative experiments. Gray-scale code for concentrations indicated in panel *D* is the same for all isoforms. Fold change in bioluminescence is relative to untreated cells at corresponding time points. The symbol § demarcates statistical differences by Tukey *post hoc* test between concentrations for the final time point. There are no statistical differences between concentrations of CXCL12-α *(C).* For CXCL12-β, 1nM is different from 3nM ($p<0.01$), 6nM ($p<0.01$), and 10 nM ($p<0.0001$). For CXCL12-γ, 1nM is different from 3nM ($p<0.05$), 6nM ($p<0.01$), and 10 nM ($p<0.0001$). Comparisons between isoforms are in supplemental information (Fig. A.5).

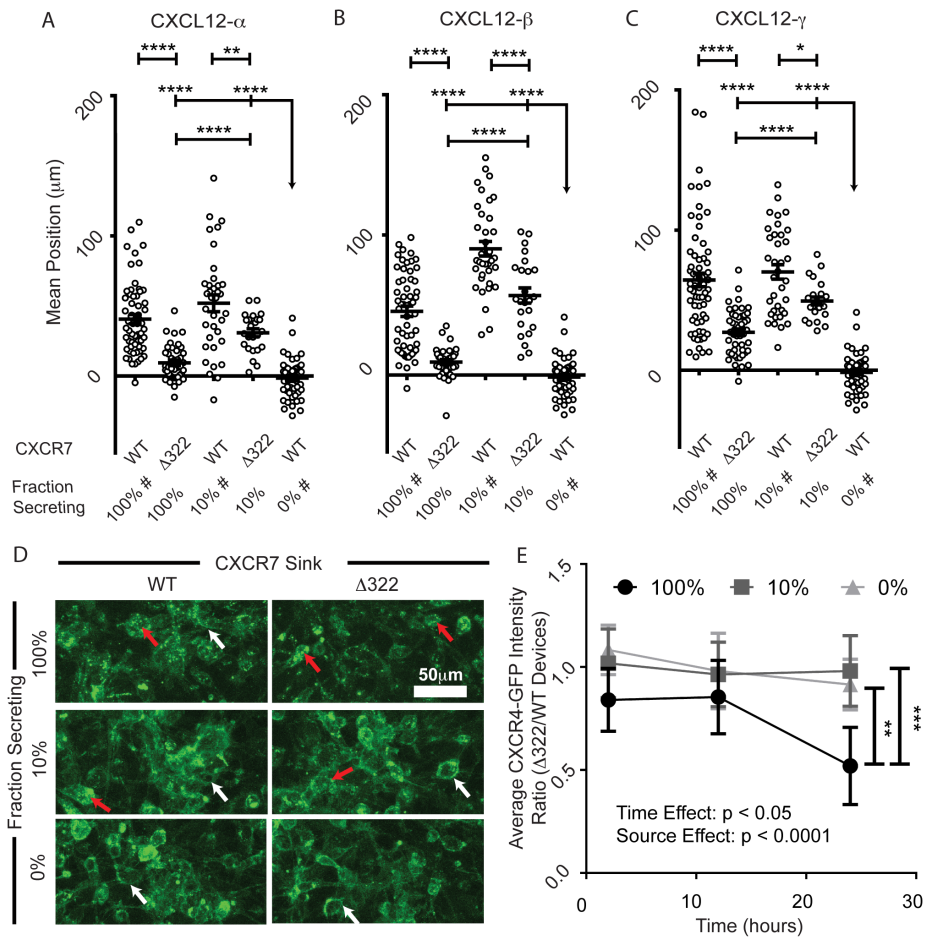

Figure 2.4. CXCR7 scavenging is necessary for chemotaxis of CXCR4+ cells in response to higher levels of CXCL12. *(A-C)* Migration of CXCR4+ cells toward various fractions of cells secreting different isoforms of CXCL12 in the presence of cells expressing either CXCR7-WT or a mutant lacking the carboxy terminus of the receptor (CXCR7-Δ322). Data are graphed as average position ± S.E.M. of migrating CXCR4+ cells after 24 hours (n=6 view fields each for 4-11 devices per condition, similar to previous figures). Fraction of secreting cells denotes the relative dilution of CXCL12-isoform secreting cells. The bar represents the statistical comparison between pairs of conditions. The arrow denotes multiple paired comparisons to the same condition (*p<0.05, **p<0.01, ****p<0.0001). Data for 100%, 10%, and 0% secreting cells are marked (#) to designate the same data plotted for comparison in multiple figures. Matched conditions were performed in parallel. *(D)* Representative Z-stack compressions of confocal images of CXCR4-GFP+ cells after 24 hours patterned in the context of dilutions of CXCL12-β (0, 10, and 100%) and with WT and CXCR7-Δ322 cells. Red arrows highlight intracellular CXCR4-GFP vesicles. White arrows denote cell membrane CXCR4-GFP. *(E)* Time course quantification of CXCR4-GFP intensity in devices patterned in the context of dilutions of CXCL12-β source cells (0, 10, and 100%). The plot depicts the mean ± SEM of the ratio between average CXCR4-GFP fluorescence intensity for devices with Δ322-CXCR7 relative to WT-CXCR7 (n=5 images from one of two representative experiments). Two-way ANOVA reveals significant time and source effects without significant interactions. The bars represent statistical significance by the Tukey *post hoc* test only for the 100% source at the 24 hour time point (** p<0.01, ***, p<0.005).

Table 2.1 CXCL12 isoforms in human breast cancer. Numbers of samples positive for each isoform of CXCL12 as determined by QRT-PCR and total number of samples for normal breast tissue and various stages of primary human breast cancers. Transcripts amplified below 40 qRT-PCR cycles and confirmed by gel electrophoresis were denoted as positive.

	CXCL12-Isoforms		
Tumor Grade:	α	β	γ
Normal	5/5	2/5	0/5
Stage I	11/11	7/11	0/11
Stage II (A+B)	13/14	7/14	0/14
Stage III (A,B,C)	14/14	13/14	1/4
Stage IV	4/4	3/4	4/4

2.8 References

1. Raman D, Sobolik-Delmaire T, & Richmond A (2011) Chemokines in health and disease. *Experimental Cell Research* 317(5):575-589.
2. Burkhardt AM, Homey B, & Zlotnik A (2011) Homeostatic chemokine receptors and organ-specific metastasis. *Nature Reviews Immunology* 11(9):597+.
3. Balkwill FR (2012) The chemokine system and cancer. *The Journal of Pathology* 226(2):148-157.
4. Zhang GX, Baker CM, Kolson DL, & Rostami AM (2000) Chemokines and chemokine receptors in the pathogenesis of multiple sclerosis. *Multiple Sclerosis* 6(1):3-13.
5. Zernecke A, Shagdarsuren E, & Weber C (2008) Chemokines in atherosclerosis: an update. *Arterioscler Throm Vasc Biol* 28(11):1897-1908.
6. Krumbholz M*, et al.* (2006) Chemokines in multiple sclerosis: CXCL12 and CXCL13 up-regulation is differentially linked to CNS immune cell recruitment. *Brain* 129(1):200-211.
7. Wu Y & Zhao R (2012) The Role of Chemokines in Mesenchymal Stem Cell Homing to Myocardium. *Stem Cell Reviews and Reports* 8(1):243-250.
8. Fukuda S & Pelus LM (2008) Chemokine-mobilized adult stem cells; defining a better hematopoietic graft. *Leukemia* 22(3):466+.
9. Yu SR*, et al.* (2009) Fgf8 morphogen gradient forms by a source-sink mechanism with freely diffusing molecules. *Nature.* 461(7263):533-536. doi: 510.1038/nature08391. Epub 02009 Sep 08399.
10. Boldajipour B*, et al.* (2008) Control of chemokine-guided cell migration by ligand sequestration. *Cell* 132(3):463-473.
11. Torisawa Y*, et al.* (2010) Microfluidic platform for chemotaxis in gradients formed by CXCL12 source-sink cells. *Integr Biol (Camb)* 2(11-12):680-686.
12. Scholpp S & Brand M (2004) Endocytosis controls spreading and effective signaling range of Fgf8 protein. *Current biology* 14(20):1834-1841.
13. Naumann U*, et al.* (2010) CXCR7 functions as a scavenger for CXCL12 and CXCL11. *PLoS One* 5(2):e9175.

14. Luker K, Steele J, Mihalko L, & Luker G (2010) Constitutive and chemokine-dependent internalization and recycling of CXCR7 in breast cancer cells to degrade chemokine ligands. *Oncogene* 29:4599-4610.
15. Luker K*, et al.* (2012) Scavenging of CXCL12 by CXCR7 promotes tumor growth and metastasis of CXCR4-positive breast cancer cells. *Oncogene* doi: 10.1038/onc.2011.633. [Epub ahead of print].
16. Ray P*, et al.* (2012) Carboxy-terminus of CXCR7 regulates receptor localization and function. *Int J Biochem Cell Biol* 44(4):669-678.
17. Fredericks Z, Pitcher J, & Lefkowitz R (1996) Identification of the G protein-coupled receptor kinase phosphorylation sites in the human beta2-adrenergic receptor. *J Biol Chem* 271(23):13796-13803.
18. Sanchez-Alcaniz J*, et al.* (2011) Cxcr7 controls neuronal migration by regulating chemokine responsiveness. *Neuron* 69(1):77-90.
19. Wang Y*, et al.* (2011) CXCR4 and CXCR7 have distinct functions in regulating interneuron migration. *Neuron* 69(1):61-76.
20. Weber M*, et al.* (2013) Interstitial Dendritic Cell Guidance by Haptotactic Chemokine Gradients. *Science* 339(6117):328-332.
21. Proudfoot AE*, et al.* (2003) Glycosaminoglycan binding and oligomerization are essential for the in vivo activity of certain chemokines. *Proceedings of the National Academy of Sciences* 100(4):1885-1890.
22. Balkwill F (2004) Cancer and the chemokine network. *Nat Rev Cancer* 4(7):540-550.
23. Balkwill F (2004) The significance of cancer cell expression of the chemokine receptor CXCR4. *Seminars in Cancer Biology* 14(3):171-179.
24. Phillips RJ*, et al.* (2004) Circulating fibrocytes traffic to the lungs in response to CXCL12 and mediate fibrosis. *Journal of Clinical Investigation* 114(3):438-446.
25. Venkiteswaran G*, et al.* (2013) Generation and Dynamics of an Endogenous, Self-Generated Signaling Gradient across a Migrating Tissue. *Cell* 155(3):674-687.
26. Donà E*, et al.* (2013) Directional tissue migration through a self-generated chemokine gradient. *Nature*.
27. Rueda P*, et al.* (2008) The CXCL12gamma chemokine displays unprecedented structural and functional properties that make it a paradigm of chemoattractant proteins. *PLoS One* 3(7):e2543.
28. Yu L*, et al.* (2006) Identification and expression of novel isoforms of human stromal cell-derived factor 1. *Gene* 374:174-179.
29. Laguri C*, et al.* (2007) The novel CXCL12gamma isoform encodes an unstructured cationic domain which regulates bioactivity and interaction with both glycosaminoglycans and CXCR4. *PLoS One* 2:e1110.
30. Gleichmann M*, et al.* (2000) Cloning and characterization of SDF-1γ, a novel SDF-1 chemokine transcript with developmentally regulated expression in the nervous system. *European Journal of Neuroscience* 12(6):1857-1866.
31. Laguri C, Arenzana-Seisdedos F, & Lortat-Jacob H (2008) Relationships between glycosaminoglycan and receptor binding sites in chemokines—the CXCL12 example. *Carbohydrate Research* 343(12):2018-2023.
32. Luker K*, et al.* (2012) *In vivo* imaging of ligand receptor binding with *Gaussia* luciferase complementation. *Nat Med* 18(1):172-177.

33. Smith M, *et al.* (2004) CXCR4 regulates growth of both primary and metastatic breast cancer. *Cancer Res* 64(23):8604-8612.
34. Song J, *et al.* (2009) Microfluidic endothelium for studying the intravascular adhesion of metastatic breast cancer cells. *PLoS One* 4(6):e5756.
35. Coggins NL, *et al.* (2014) CXCR7 Controls Competition for Recruitment of β-Arrestin 2 in Cells Expressing Both CXCR4 and CXCR7. *PLoS ONE* 9(6):e98328.
36. Luker K, Gupta M, & Luker G (2008) Imaging CXCR4 signaling with firefly luciferase complementation. *Anal Chem* 80(14):5565-5573.
37. Luker K, Gupta M, Steele J, Foerster B, & Luker G (2009) Imaging ligand-dependent activation of CXCR7 *Neoplasia* 11(10):1022-1035.
38. Luker K, Gupta M, & Luker G (2009) Bioluminescent CXCL12 fusion protein for cellular studies of CXCR4 and CXCR7 *Biotechniques* 47(1):625-632.
39. Ray P, *et al.* (2012) Secreted CXCL12 (SDF-1) forms dimers under physiologic conditions. *Biochem J* 442:433-442.
40. Orimo A, *et al.* (2005) Stromal fibroblasts present in invasive human breast carcinomas promote tumor growth and angiogenesis through elevated SDF-1/CXCL12 secretion. *Cell* 121(3):335-348.
41. Boimel P, *et al.* (2012) Contribution of CXCL12 secretion to invasion of breast cancer cells. *Breast Cancer Res* 14(1):R23.
42. Torres R & Ramirez JC (2009) A Chemokine Targets the Nucleus: Cxcl12-Gamma Isoform Localizes to the Nucleolus in Adult Mouse Heart. *PLoS ONE* 4(10):e7570.
43. Altenburg J, *et al.* (2007) A naturally occurring splice variant of CXCL12/stromal cell-derived factor 1 is a potent human immunodeficiency virus type 1 inhibitor with weak chemotaxis and cell survival activities. *J Virol* 81(15):8140-8148.
44. Altenburg J, Jin Q, Alkhatib B, & Aklhatib G (2010) The potent anti-HIV activity of CXCL12γ correlates with efficient CXCR4 binding and internalization. *J Virol* 84(5):2563-2572.
45. Lagane B, *et al.* (2008) CXCR4 dimerization and {beta}-arrestin-mediated signaling account for the enhanced chemotaxis to CXCL12 in WHIM syndrome. *Blood* 112(1):34-44.
46. Drury L, *et al.* (2011) Monomeric and dimeric CXCL12 inhibit metastasis through distinct CXCR4 interactions and signaling pathways. *Proc Natl Acad Sci U S A*:Oct 11 [Epub ahead of print].
47. Villalobos V, *et al.* (2011) Dual-color click beetle luciferase heteroprotein fragment complementation assays. *Chem Biol* 17(9):1018-1029.
48. Fricker SP, *et al.* (2006) Characterization of the molecular pharmacology of AMD3100: a specific antagonist of the G-protein coupled chemokine receptor, CXCR4. *Biochem Pharmacol* 72(5):588-596.
49. Miao Z, *et al.* (2007) CXCR7 (RDC1) promotes breast and lung tumor growth in vivo and is expressed on tumor-associated vasculature. *Proc Natl Acad Sci U S A* 104(40):15735-15740.
50. Netelenbos T, *et al.* (2002) Proteoglycans guide SDF-1-induced migration of hematopoietic progenitor cells. *J Leukoc Biol* 72:353-362.
51. Valenzuela-Fernandez A, *et al.* (2001) Optimal Inhibition of X4 HIV Isolates by the CXC Chemokine Stromal Cell-derived Factor 1alpha Requires Interaction with Cell Surface Heparan Sulfate Proteoglycans. *J. Biol. Chem.* 276(28):26550-26558.

52. Murphy J, *et al.* (2007) Structural and functional basis of CXCL12 (stromal cell-derived factor-1) binding to heparin. *J Biol Chem* 282(13):10018-10027.
53. Sun Y, Cheng Z, Ma L, & Pei G (2002) Beta-arrestin2 is critically involved in CXCR4-mediated chemotaxis, and this is mediated by its enhancement of p38 MAPK activation. *J Biol Chem* 277(51):49212-49219.
54. Fermas S, *et al.* (2008) Sulfated oligosaccharides (heparin and fucoidan) binding and dimerization of stromal cell-derived factor-1 (SDF-1/CXCL 12) are coupled as evidenced by affinity CE-MS analysis. *Glycobiology* 18(12):1054-1064.
55. Veldkamp C, Peterson F, Pelzek A, & Volkman B (2005) The monomer-dimer equilibrium of stromal cell-derived factor-1 (CXCL 12) is altered by pH, phosphate, sulfate, and heparin. *Protein Sci* 14(4):1071-1081.
56. Veldkamp C, *et al.* (2008) Structural basis of CXCR4 sulfotyrosine recognition by the chemokine SDF-1/CXCL12. *Sci Signal* 1:ra4.
57. Venables JP (2004) Aberrant and Alternative Splicing in Cancer. *Cancer Research* 64(21):7647-7654.
58. Cheung N, Wong MP, Yuen ST, Leung SY, & Chung LP (1998) Tissue-specific expression pattern of vascular endothelial growth factor isoforms in the malignant transformation of lung and colon. *Human pathology* 29(9):910-914.
59. Rueda P, *et al.* (2012) Homeostatic and Tissue Reparation Defaults in Mice Carrying Selective Genetic Invalidation of CXCL12/Proteoglycan Interactions / Clinical Perspective. *Circulation* 126(15):1882-1895.
60. Kim BJ, *et al.* (2013) Cooperative roles of SDF-1α and EGF gradients on tumor cell migration revealed by a robust 3D microfluidic model. *PLoS ONE* 8(7):e68422.
61. Condeelis J & Segall J (2003) Intravital imaging of cell movement in tumours. *Nature Rev Cancer* 3:921-930.
62. Kedrin D, *et al.* (2008) Intravital imaging of metastatic behavior through a mammary imaging window. *Nat Methods* 5(12):1019-1021.
63. Rueda P, *et al.* (2012) Homeostatic and Tissue Reparation Defaults in Mice Carrying Selective Genetic Invalidation of CXCL12/Proteoglycan InteractionsClinical Perspective. *Circulation* 126(15):1882-1895.

Chapter Three: Systems for Three Dimensional Spheroid Imaging

3.1 Summary

Three-dimensional culture systems bridge the experimental gap between *in vivo* and *in vitro* physiology. However, non-standardized formation and limited downstream adaptability of three-dimensional cultures have hindered mainstream adoption of these systems for biological applications, especially for low- and moderate-throughput assays commonly used in biomedical research. Here we build upon our recent development of a 384 well hanging drop plate for spheroid culture to design a complementary spheroid transfer and imaging (TRIM) plate. The low aspect ratio wells of the TRIM plate facilitated high fidelity, user-independent, contact-based collection of hanging drop spheroids. Using the TRIM plate, we demonstrated several downstream analyses including bulk tissue collection for flow cytometry, high-resolution low working-distance immersion imaging, and timely reagent delivery for enzymatic studies. Low working distance multi-photon imaging of spheroids revealed cell-type dependent, macroscopic spheroid structure. Unlike ovarian cancer spheroids, which formed loose, disc-shaped spheroids, human mammary fibroblasts formed tight, spherical, and nutrient-limited spheroids. Beyond the applications we describe here, we expect the hanging drop spheroid plate and complementary TRIM plate to facilitate analyses of spheroids across the spectrum of throughput, particularly for bulk collection of spheroids and high-content imaging.

3.2 Introduction

Many cell culture applications are moving towards more physiological three dimensional model systems to bridge the gap between non-physiological two-dimensional platforms and *in vivo* conditions. Mass transport of drugs, nutrients, and metabolites in these systems is more representative of profiles of parameters such as hypoxia and metabolism. Despite these advantages, previous technologies for spheroid cultures were not used extensively due to lack of throughput (e.g. microfluidics), limited spheroid uniformity (e.g. rotating flasks), and cumbersome non-standardized handling and analysis. Challenges to standardization, implementation, and analysis of three-dimensional tissue cultures, have limited widespread adoption (1). Comparison and standardization of spheroid formation systems is also necessary to reconcile observed differences in gene expression and respiratory status for spheroids formed in hanging as compared to microfluidic systems (2).

To address many of these issues, we developed a 384 hanging drop plate for high throughput formation and analysis of individual and uniform spheroids (3, 4). Our hanging drop system consists of 384 through-holes to facilitate formation of uniform spheroids and ready access to the medium via the through-hole to exchange media, add treatments, or add cells at a defined time points. Other groups have developed systems for hanging drop formation that rely on gravity-enforced cell assembly (5). The simplest but least stable strategy for hanging drop formation is to plate droplets on the underside of non-adherent culture dishes (6). The company, InSphero also developed a 96 well gravity-driven hanging drop system that uses a similar through-hole strategy as our 384 well plate (7, 8). Many imaging-based analyses, however, require a spheroid to be transferred to a secondary dish

for stable focusing. High fidelity transfer of hanging drop spheroids to a fixed substrate for downstream analysis requires highly parallel and consistent pipetting, which is inefficient and time consuming by hand and costly to automate. While the InSphero GravityTrap system enables transfer of 96-well array format hanging drop spheroids to a secondary 96 well plate substrate, it disallows immersion-based imaging and facile bulk collection.

Here we report the development of a transfer and imaging (TRIM) plate to expand the usefulness of the 384 hanging drop system and facilitate these previously difficult downstream analyses. We differentiate our system from the InSphero system based on increased throughput (384-well array format vs 96) and low aspect transfer wells that facilitate high-fidelity spheroid capture, immersion-based imaging, bulk spheroid collection, and timely enzyme-substrate kinetic studies.

3.3 Materials and Methods

3.3.1 Plate design

We used SolidWorks to conceptualize the TRIM plate in three dimensions. We fabricated the TRIM plate in the material Accura ® 60 (3DSystems) using the SLA Viper si2 dual resolution SLA system, which is conducted by the University of Michigan Medical Innovation Center. The dimensions of the 384 wells are a total depth of 1.25 mm, which serves as the optical working distance, and a total well diameter of 4 mm. The wells are formatted as a standard 384 well plate to match the 384 hanging drop plate with a 16 by 24 array spaced every 4.5 mm. The inner-wall dimensions of the original 384 hanging drop plate match the outer-wall of the TRIM plate and serve as physical guides for high fidelity matching between droplets and wells. We developed a multi-radial well contour to

facilitate settling of the spheroid in the center of the well while limiting spheroids sticking in corners due to surface tension (Fig. B.2). Around the periphery of the plate there is a 2 mm ridge that guides medium overflow during bulk spheroid collection.

3.3.2 Cells and spheroid cultures

We cultured all cells in DMEM supplemented with 10% fetal bovine serum and 1% antibiotic. We used several cell types to form spheroids, including MDA-MB-231 breast cancer cells (ATCC), HeyA8 ovarian cancer cells (gift of Gordon Mills, MD Anderson Cancer Center), and a human mammary fibroblast cell line expressing green fluorescent protein (GFP) (9). We transduced HeyA8 ovarian cancer cells with a lentiviral vector for GFP and sorted for a population of stably transduced cells by flow cytometry (10). We previously have described MDA-MB-231 cells stably expressing eqFP650, GFP, or firefly luciferase (11). We formed and maintained spheroids in 25 μl of culture medium as we described previously using the 384 hanging drop plate (3, 4).

3.3.3 Contact based spheroid transfer and collection

To transfer hanging drop spheroids we aligned the TRIM plate based on designed plate guides and lowered the hanging drop plate to contact the TRIM plate (Fig. 3.1A-D). We allowed spheroids to settle into the transfer wells for 1-2 minutes to improve transfer efficiency. We evenly lifted and separated the hanging drop plate from the recipient TRIM plate for spheroid transfer.

3.3.4 Spheroid analysis and imaging

For two-photon imaging of spheroids, we used a 25X objective (XLPLN, NA: 1.05) and upright confocal and two-photon microscope (Olympus MPE Twin) as we have

described before (12). We imaged individual HeyA8 spheroids and HMF spheroids both containing 15,000 cells per droplet. We very gently immersed the TRIM plate in growth medium after spheroid transfer for upright immersion microscopy. For imaging we maintained resolution and z-step increment but varied the laser intensity between HMF and HeyA8 spheroids due to differences in their overall fluorescent intensity.

We collected 100 spheroids containing 10,000 cells total with different ratios (1:1 and 1:9) of 231 cells expressing either nuclear-GFP or FP650 for flow cytometry analysis (Fig. 3.2). To collect spheroids we transferred them to the TRIM plate and used ~50 ml of DMEM culture medium to wash spheroids from the TRIM plate into a 50 ml conical tube. We centrifuged the spheroids and resuspended the pellet in 0.25% trypsin with EDTA. Once spheroids were dissociated, we neutralized trypsin with full DMEM medium, centrifuged the sample, and resuspended the cells in phosphate buffered saline for flow cytometry analysis. Flow cytometry was done using a Becton Dickinson FACS DiVa Flow Cytometer. We set the sort quadrants with excitation at 488 and 633 nm based on fluorescence negative MDA-MB-231 cells (Fig. 3.2B - Negative Control). The quadrant statistics were determined with the Becton Dickinson software.

For bioluminescence imaging we seeded 154 spheroids (every other well in 384 wells) containing 10,000 cells per drop total at a ratio of 9:1 HMF cells and MDA-MB-231 cells expressing firefly luciferase. We plated water in the outer wells to minimize evaporation. Prior to transfer of spheroids to the TRIM plate, we added 3 µl of 15 mg/ml luciferin diluted 4X in phosphate buffered saline to each corresponding well on the TRIM plate. Contact between the spheroid droplet and the pre-plated luciferin caused

simultaneous mixing of all transferred droplets. We quantified the number of wells with detectable bioluminescence of firefly luciferase as we have described before (Fig. B.1) (13).

We stained HMF spheroids with trypan blue after 3-4 days of culture to increase contrast by staining for dead cells. To stain the cells we added 2 µl of 4X dilution of trypan blue in PBS to each droplet for 4 hours prior to transfer. We exchanged 10 µl of media twice to remove the residual trypan blue in each droplet. After transfer we imaged the TRIM plate with a white light back light using a 5MP camera (Fig. 3.1F).

3.4 Results and Discussion

3.4.1 Spheroid transfer and imaging

The TRIM plate structure is complementary to the 384 hanging drop plate designed by our group with designs to enable: 1) gentle, high-fidelity contact-based drop and spheroid transfer, 2) bulk spheroid collection, and 3) high-resolution imaging with short optical working distance objectives (Fig. 3.1, 3.2, and 3.3, respectively). The low aspect ratio of our plate is markedly different from the InSphero GravityTrap system, which disallows immersion imaging and bulk collection (7). We designed low aspect ratio wells less than 2 mm in depth, which is less than the height of the hanging 25 µl droplets for contact-based drop transfer and low working distance immersion imaging (Fig. 3.1D). A visual demonstration with dyed droplets illustrates the simple high-fidelity transfer process using 384 droplets (Fig. 3.1E-F). The residual volume of liquid (~5µl) remains in the 384 hanging drop plate (Fig. 3.1E top), but spheroids localize to the bottom of the droplet by gravity and transfer robustly (Fig. 3.1F).

We demonstrate 100% spheroid capture efficiency (154/154) based on the number of bioluminescent spheroids that transferred to TRIM plate wells containing pre-plated enzymatic substrate, luciferin (Fig. B.1). The benefit of measuring bioluminescence in spheroids was two-fold. First we provided a quantitative demonstration of robust spheroid transfer, where only existing spheroids expressing firefly luciferase that transferred to wells with pre-plated luciferin emitted a signal. Second, we highlighted the simultaneous initiation of bioluminescence kinetics for all spheroids via addition of enzymatic substrate to the spheroids at a discrete time. The timing and kinetics of enzyme-substrate interactions are critical to many assays. Also, the magnitude and trajectory of the signal from an enzymatic assay in spheroids may be limited by enzyme concentration, substrate or ligand concentration, diffusion into the cell, or diffusion into the spheroid. For researchers performing time-sensitive kinetics assays without access to an automated liquid handler, simultaneous administration of reagents is a distinct advantage. Rather than pipetting substrate or ligand into individual hanging drop wells in a time-dependent manner, the TRIM plate enables facile and simultaneous administration of luciferin substrate to initiate measurements for kinetic assays. We envision using this strategy for administration of ligand and or luciferase substrate for more advanced bioluminescence applications, such as quantifying ligand-receptor interactions or intracellular signaling in spheroids (14). In this situation we could use a multi-channel or single pipette to dispense the ligand into the receiving plate, followed by initiation of signaling at the time of spheroid transfer.

One challenge with analysis of adherence-independent cultures like spheroids is to physically but reversibly immobilize the sample to minimize movement and facilitate

organized downstream analysis. We highlight these challenges particularly for immersion imaging, where sample stability is at a premium and imaging in the hanging drop plate is impossible. Transfer of spheroids to a rigid substrate enhanced stability and allowed for immersion imaging. Although transfer to standard culture dishes is possible, movement due to flow in standard culture formats disrupts imaging. To improve this we implemented a multi-curvature well contour (Fig. B.2) to facilitate settling of the spheroid to the direct center of each well (Fig. 3.1F), rather than to the peripheral edges of standard flat bottom dishes. We found our well depth was optimal for low working distance objectives, but provided adequate resistance to spheroid movement by fluid flow. Organized transfer maintains the experimental setup of multiple conditions and enables imaging of spheroid conditions sequentially without losing track of particular conditions and the experiment organization.

3.4.2 Spheroid collection and analysis

Standard two-dimensional cell culture platforms are amenable to subcellular, single cell, and population analysis. While three-dimensional and high-resolution imaging applications discussed above address the two former analysis scales, population analysis for population-, DNA-, RNA-, protein-, and metabolite-level assays requires high efficiency recovery of many cells, which is difficult in most three-dimensional culture formats. We used the TRIM plate to collect bulk spheroids simultaneously for dissociation and analysis using flow cytometry. After transfer of spheroids, we released them by tilting the TRIM plate, directing flow from a pipette down into the wells, and collecting the overflow in a 50 ml conical tube (Fig. 3.2A). Following enzymatic dissociation of the spheroids with trypsin, we analyzed spheroids containing 1:9 and 1:1 ratios of 231 cells expressing either GFP or

FP650 (Fig. 3.2C-D). We note that the FP650 cells were not homogeneously expressing, causing them to show up in both bottom quadrants of the flow cytometry plot. However, these are still intensity shifted for FP650 relative to the negative control (Fig. 3.2C-E). Our flow cytometry analysis closely matched the proportion of 1:1 and 1:9 for GFP to FP650 by summing the bottom quadrants for the FP650 cells and top quadrants for the GFP cells (Fig. 3.2E-F).

3.4.3 High resolution three dimensional imaging

Since the spheroid settles to the lower curvature and is relatively fixed, we demonstrate imaging of the three-dimensional volume of large spheroids using two photon microscopy (Fig. 3.3A-D) for HeyA8 ovarian cancer (Fig. 3.3A-B) and HMF spheroids, both expressing GFP. We note the hemispherical disc shape of the ovarian cancer "spheroid" to be striking (Fig. 3.3B), as the perception of a spheroid is understandably spherical. The HMF cells formed a smaller, tight structure with largely spherical morphology. The density of the HMF spheroid also led to metabolic limitations in the center of the spheroid, which we speculate decreased protein synthesis and resulted in lower GFP intensity. Based on the morphology of the spheroids, the shape of the HeyA8 spheroid seems to be physically dictated by the droplet radius (Fig. 3.3E,G). Others have observed disc-like ovarian cancer spheroids that were formed in hanging droplets and cite the importance of defining the geometric spheroid morphology (15). The strong intracellular forces between the HMF cells, on the other hand, lead to a tight spherical shape (Fig. 3.3F,H). Others have defined nutrient transfer limitations and hypoxia in three dimensional cell spheroids for structures above ~100-200 μm in diameter (16). However, nutrient limitations are very much cell-type and spheroid-shape dependent and must be characterized for new cells at the onset of

a project. For defining nutrient limitations and hypoxia the complementary hanging drop and TRIM plates enable three-dimensional multi-photon image-based screening of many combinations of cell types and conditions in parallel.

3.5 Future directions and opportunities

Widespread adoption of three-dimensional tissue culture is dependent on three aspects: ease-of-use, standardization, and scale. We previously developed a 384 well hanging drop plate to improve standardization of spheroid culture and spheroid uniformity. However, it is biased towards facilitating high-throughput analyses, such as robotic automation and standard plate reader assays. Efficient tools for recovery of spheroids will broaden applicability of hanging drop spheroids and encompass the full spectrum of throughput, from high-throughput analysis to low- and moderate-throughput analyses, such as high-resolution imaging and flow cytometry. We used the TRIM plate to demonstrate facile handling for high resolution imaging of individual spheroids and flow cytometric analysis of bulk-collected spheroids. The TRIM plate improves compatibility of hanging drop spheroids with low and moderate throughput analyses that are bioassay staples. We believe these systems substantially improve the utility of spheroid cultures for biomedical research, bridging the gap between low-throughput *in vivo* models and standard two dimensional tissue culture systems.

3.6 Figures

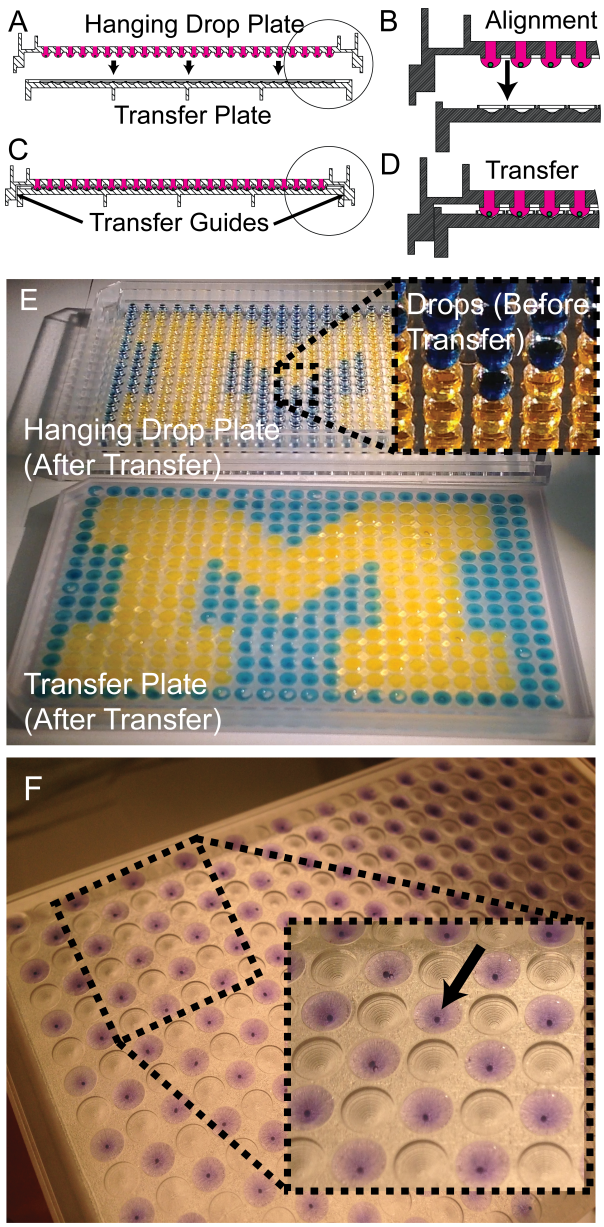

Figure 3.1. Transfer and imaging of 384 hanging drop spheroids. (A) Schematic representation of the hanging drop plate and complementary TRIM plate. The circle in (A) defines the region detailed in panel (B). (C) Schematic depiction of hanging drop plate transfer with user-independent alignment guides. The circle in (C) defines the region detailed in panel (D), showing contact dependent drop transfer. (E) Example images of the residual dye in the hanging drop plate (top) after transfer to the TRIM plate (bottom). The inset shows the bottom view of the hanging droplets prior to transfer. (F) Example image of 500 μm spheroids transferred from the hanging drop plate to the TRIM plate. Spheroids were stained with trypan blue for 4 hours prior to transfer to improve image contrast.

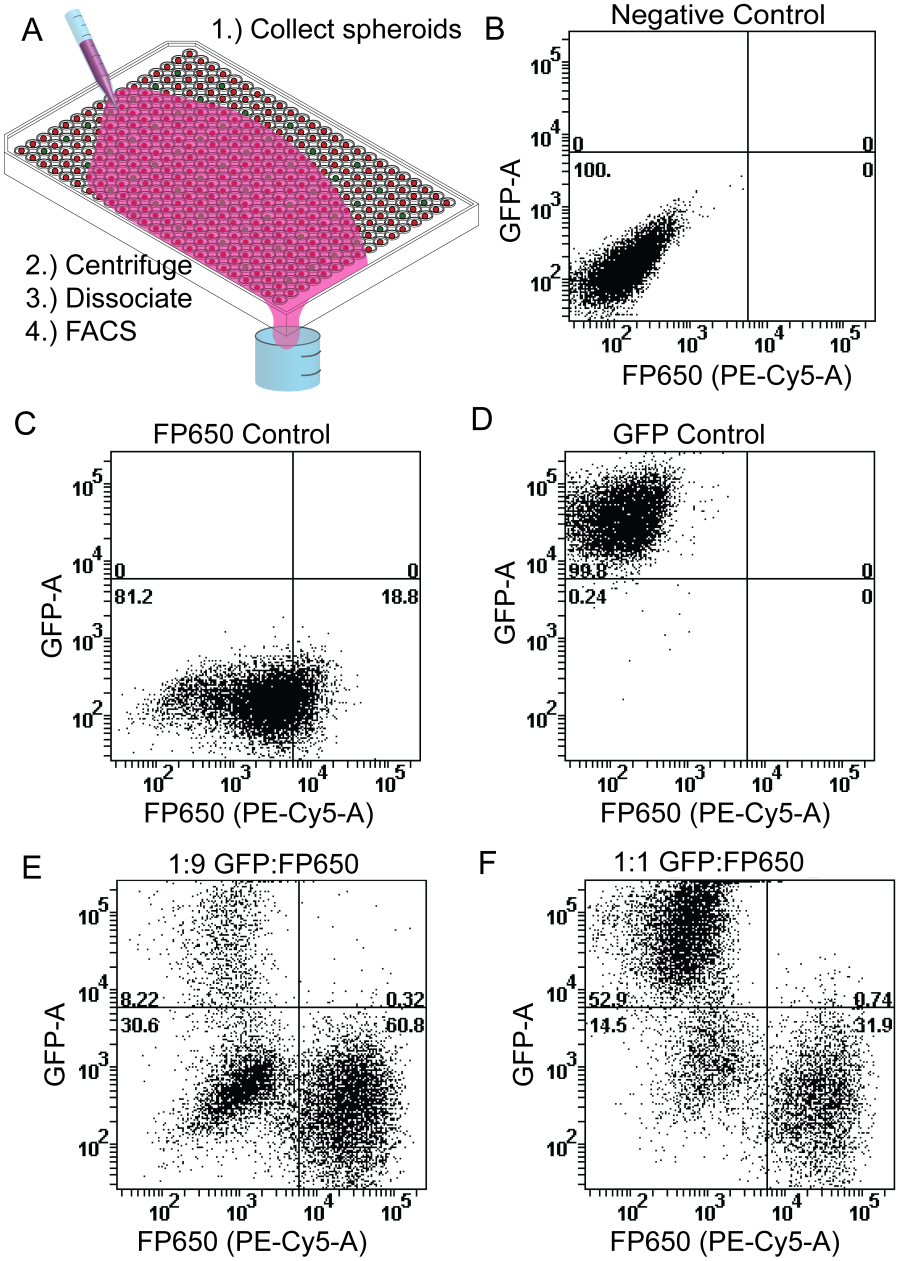

Figure 3.2. Spheroid collection for analysis by flow cytometry. (A) We co-seeded spheroids with MDA-MB-231 cells at ratios of 9:1 and 1:1 of cells expressing FP650 or GFP, respectively. Schematic of spheroid collection by directing pipette flow into each well and collecting the overflow. After collection, centrifugation, and spheroid dissociation, we performed flow cytometry. (B-F) Flow cytometry scatter plots show MDA-MB-231 cells with no fluorescent protein (B), FP650 only (C), GFP only (D), and 9:1 (E) and 1:1 (F) ratios of FP650 and GFP cells, respectively. Note that we compare the top two quartiles to the bottom quartiles to estimate the relative seeding of FP650 and GFP cells in order to capture the heterogeneity of the FP650 cells.

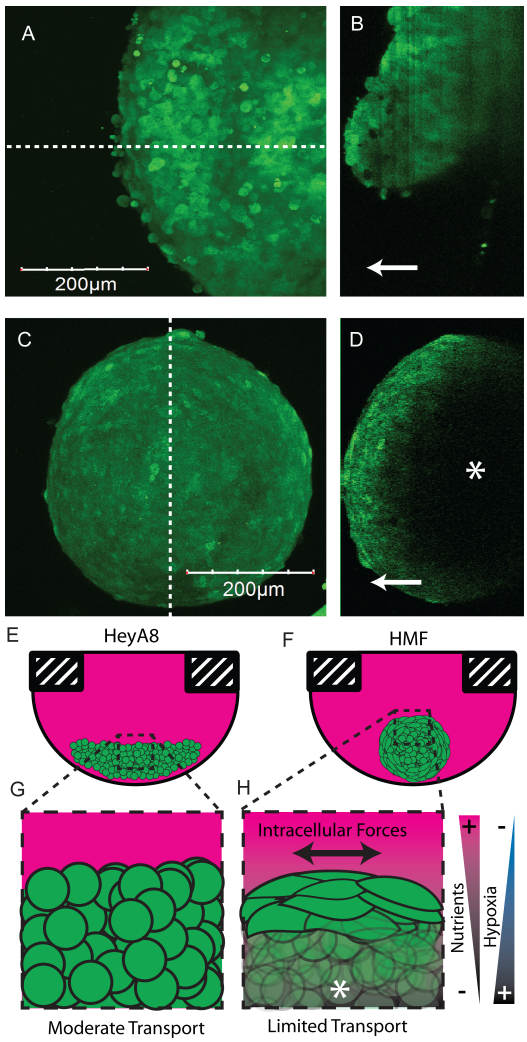

Figure 3.3. Three dimensional imaging with the TRIM plate. (A) Example two-photon z-stack image of a large spheroid of HeyA8 ovarian cancer cells expressing GFP and (B) the corresponding cross section with the location denoted by the dotted line in (A). (C) Example two-photon z-stack image of a large spheroid of HMF expressing GFP spheroid and (D) the corresponding cross section with the location denoted by the dotted line in (A). Arrows (B and D) denote the upward direction towards the objective. Unlike the ovarian cancer spheroid, the HMF spheroid is dense and nutrient limited resulting in lower internal fluorescence intensity denoted by * (D,H). Schematics of the spheroid morphology show HeyA8 spheroids to curve with the droplet radius (E) and the HMF spheroid to be spherical (F). Loose interactions between HeyA8 cells are permissive to nutrient transport within the spheroid (G), but tight intracellular forces limit transport into the spheroid (H).

3.7 References

1. Mehta G, Hsiao A, Ingram M, Luker G, & Takayama S (2012) Opportunities and challenges for use of tumor spheroids as models to test drug delivery and efficacy. *J Control Release* May 18 [Epub ahead of print].

2. Zhou Y, *et al.* (2013) Multi-parameter analyses of three-dimensionally cultured tumor spheroids based on respiratory activity and comprehensive gene-expression profiles. *Anal Biochem* 26(13):00194-00192.
3. Hsiao AY, *et al.* (2012) 384 hanging drop arrays give excellent Z-factors and allow versatile formation of co-culture spheroids. *Biotechnol Bioeng.* 109(5):1293-1304. doi: 1210.1002/bit.24399. Epub 22011 Dec 24320.
4. Tung Y, *et al.* (2011) High-throughput 3D spheroid culture and drug testing using a 384 hanging drop array. *Analyst* 136(3):473-478.
5. Kelm JM & Fussenegger M (2004) Microscale tissue engineering using gravity-enforced cell assembly. *Trends in biotechnology* 22(4):195-202.
6. Laib AM, *et al.* (2009) Spheroid-based human endothelial cell microvessel formation in vivo. *Nature protocols* 4(8):1202-1215.
7. Drewitz M, *et al.* (2011) Towards automated production and drug sensitivity testing using scaffold‐free spherical tumor microtissues. *Biotechnology Journal* 6(12):1488-1496.
8. Waschow M, Letzsch S, Boettcher K, & Kelm J (2012) High-content analysis of biomarker intensity and distribution in 3D microtissues. *Nature Methods* 9(9).
9. Orimo A, *et al.* (2005) Stromal fibroblasts present in invasive human breast carcinomas promote tumor growth and angiogenesis through elevated SDF-1/CXCL12 secretion. *Cell* 121(3):335-348.
10. Smith M, *et al.* (2004) CXCR4 regulates growth of both primary and metastatic breast cancer. *Cancer Res* 64(23):8604-8612.
11. Luker K, *et al.* (2012) *In vivo* imaging of ligand receptor binding with *Gaussia* luciferase complementation. *Nat Med* 18(1):172-177.
12. Salomonnson E, Mihalko LA, Verkhusha VV, Luker KE, & Luker GD (2012) Cell-based and in vivo spectral analysis of fluorescent proteins for multiphoton microscopy. *J Biomed Opt.* 17(9):96001. doi: 96010.91117/96001.JBO.96017.96009.096001.
13. Miao Z, *et al.* (2007) CXCR7 (RDC1) promotes breast and lung tumor growth in vivo and is expressed on tumor-associated vasculature. *Proc Natl Acad Sci U S A* 104(40):15735-15740.
14. Luker K, Gupta M, & Luker G (2008) Imaging CXCR4 signaling with firefly luciferase complementation. *Anal Chem* 80(14):5565-5573.
15. Das T, *et al.* (2013) Empirical chemosensitivity testing in a spheroid model of ovarian cancer using a microfluidics-based multiplex platform. *Biomicrofluidics* 7:011805.
16. Serganova I, *et al.* (2004) Molecular imaging of temporal dynamics and spatial heterogeneity of hypoxia-inducible factor-1 signal transduction activity in tumors in living mice. *Cancer Research* 64(17):6101-6108.

Chapter Four: Bone Marrow Co-Culture Model to Selectively Eliminate Quiescent Cancer Cells

4.1 Summary

Patients with many types of malignancy commonly harbor quiescent cancer cells in bone marrow. These cells ultimately may resume proliferation, causing late onset recurrences. Quiescent cells in bone marrow frequently resist current treatments because anticancer drugs typically are screened against dividing cancer cells. To meet the challenge of eliminating quiescent cancer cells from bone marrow while minimizing toxicity to stromal cells, we developed a 384-well 3D spheroid model with few breast cancer cells co-cultured with bone marrow stromal cells. Fluorescence and bioluminescence imaging revealed that cancer cells became reversibly arrested in G1 phase of the cell cycle when co-cultured with HS5 bone marrow stromal cells, but proliferated rapidly with HS27A stromal cells. We identified individual and combinations of compounds that preferentially eliminated quiescent cancer cells but not stromal cells, establishing a new platform for analyzing and targeting quiescent cancer cells. We found that within quiescent co-cultures and under cytotoxic stress, MDA-MB-231 breast cancer cells become more sensitive to MEK inhibition. Extending this finding to a mouse model, we more effectively diminished bone marrow metastases using a combination of doxorubicin and MEK inhibition. This bone marrow co-culture model provides a new platform to identify compounds that selectively target quiescent cancer cells.

4.2 Introduction

Current anticancer drugs typically target proliferating cells but have lower efficacy against quiescent cancer cells, leaving residual cancer cells that ultimately may cause recurrent disease even decades later. A major challenge in cancer therapy is eliminating quiescent cancer cells while limiting toxicities to normal tissues. To identify drugs and drug combinations that eradicate residual quiescent cancer cells, there is an unmet need for platforms that reproduce reversible cancer cell quiescence; allow simultaneous monitoring of cancer and stromal cells; and enable testing in formats amenable to high throughput testing. We meet these needs with a novel combination of multi-modal imaging, a multi-well format, and a 3D spheroid co-culture model that replicates quiescence of cancer cells.

We focus on quiescent cancer cells in bone marrow, a major reservoir for single or microscopic foci of malignant cells in patients. Bone marrow biopsies show that as many as 60% of patients with malignancies including breast, prostate, pancreas, non-small cell lung, and melanoma have detectable cancer cells even in the absence of overt metastases (1, 2). Interactions between cancer and bone marrow stromal cells critically regulate quiescence of malignant cells, potentially allowing malignant cells to remain viable for decades (3). Quiescent cancer cells ultimately may resume proliferation, contributing to established correlations of cancer cells in bone marrow with higher risk of disease recurrence and mortality (4, 5).

In addition to inducing quiescence of cancer cells, bone marrow is a key determinant of efficacy and side effects of chemotherapy. Bone marrow stromal cells confer drug resistance to malignant cells (6-8), allowing cancer cells to survive standard chemotherapy. Ten to 15% of patients with breast cancer have detectable malignant cells

in bone marrow after adjuvant therapy, and these patients have a greater than three-fold higher risk of disease recurrence (9). Conversely, damage to cells and the environment of bone marrow commonly complicates cancer chemotherapy, limiting dosing of many drugs and the ability to cure patients. Therefore, a drug-testing platform to target cancer cells in bone marrow must model cancer-stromal interactions and account for viability of malignant and stromal cell populations during treatment.

The many cellular components of the bone marrow make modeling its physiology very difficult. Similar to the dichotomous maintenance or expansion of the hematopoietic stem cell (HSC) population, cancer cells' quiescence or growth takes place in different marrow niches, including the endosteal niche and/or the perivascular sinusoid. These marrow niches contain mesenchymal stroma, vascular, and immune cells, to name a few (10). We began with a simpler model by creating 3D stromal spheroids of bone marrow derived mesenchymal stromal cell lines. The human stromal cell lines that we use (HS-5, and HS-27A) have divergent properties in their gene expression (11), secreted cytokines, extracellular matrix production, and morphology (12). These differences determine maintenance, growth, differentiation (12), apoptosis (13), engraftment (14), and drug sensitivity (15) of HSCs and/or cancer cells *in vitro* and *in vivo.*

Existing *in vitro* models capture some aspects of the bone marrow environment but lack features needed for drug targeting of quiescent cancer cells. Two recent studies used a 2D bone marrow co-culture system or stromal conditioned media to identify compounds that overcome stromal-mediated drug resistance. However, these studies did not consider cancer quiescence or toxicity to stromal cells (15, 16). Studies in 2D models also minimize or eliminate key aspects of bone marrow, including intercellular contacts, hypoxia and

mass transport limitations of drugs (17-19). Marlow et al used Gelfoam™ 3D biomatrix co-cultures with different stromal cells to support growth or quiescence of cancer cells (20). While useful for mechanistic studies, the assay format precludes large-scale screening of compounds to selectively eliminate cancer but not stromal cells. Our group and others also have shown cancer cell growth is diminished in 3D co-cultures, which also may also contribute to quiescent phenotypes (21). Therefore, both stromal co-culture and the dimensionality of the assay control the growth of cancer cells.

We developed a new 3D spheroid co-culture spheroid model of breast cancer cells and bone marrow stromal cells, using a combination of fluorescence and bioluminescence imaging to verify that cancer cells were in a quiescent or growing state. To quantify viability of both cancer and stromal cells in the same spheroid, we implemented a dual-color click beetle luciferase assay in which cancer and stromal cells express green and red spectral variants, respectively. We demonstrated use of this dual-color luciferase method to identify combinations of compounds that preferentially eliminate breast cancer cells from spheroids while minimizing toxicity to stromal cells. Importantly, a combination therapy identified in our spheroid model effectively eliminated quiescent breast cancer cells from bone marrow in a mouse tumor model, establishing that our spheroid assay models treatment efficacy *in vivo*.

4.3 Materials and Methods

4.3.1 Reagents

We purchased all cell culture reagents from Life Technologies (Carlsbad, CA, USA) unless otherwise stated. We obtained drugs, compounds, and hormone supplements from

the following sources: AG-490, PD0325901, CP724714, MK-2206 2HCl, MK-8669, GDC-0941, Bazedoxifene HCl, Trametinib (GSK112021), and Fulvestrant from SelleckChem (Houston, TX, USA); AMD3100 from Tocris Bioscience (Bristol, UK); SB-431542 from Caymen Chemical (MI, USA), 4-hydroxytamoxifen and β-estradiol from Sigma Aldrich (St. Louis, MO, USA); and Cisplatin (NDC-0703-5748-11), Paclitaxel (NDC-55390-304-50), and Doxorubicin (NDC-0069-3030-20), from the University of Michigan Hospital Pharmacy as clinical formulations. We prepared 10 mM stocks of estrogen in ethanol, while we used other drugs in formulations supplied or specified by manufacturers. Accumax was purchased from Innovative Cell Technologies (San Diego, CA, USA).

4.3.2 Cell lines and reporters

All cells were maintained in 10% FBS (HyClone, ThermoScientific, Waltham, MA, USA) DMEM (#11995, Life Technologies) supplemented with penicillin, streptomycin, and glutamine (Life Technologies). We passaged cells every two to four days by trypsinizing and resuspending. We received immortalized human mammary fibroblasts (HMF) as a gift from R. Weinberg (22). We obtained immortalized human bone marrow stromal cell lines HS-5 and HS27A, and breast cancer cell lines MDA-MB-231, MDA-MB-468, SKBR3 and T47D from the American Type Culture Collection.

Plasmid contructs: CBRed was amplified from plasmid pCBR-Basic (Promega, WI, USA) with PCR primers XbaI CBR forward 5'-ATTATCTAGAACCGCCATGGTAAAGCGTGAGAAAAATGTC-3' and XbaI CBR reverse 5'-ATTATCTAGATTACTAACCGCCGGCCTTCACCAAC-3' and CBG99 was amplified from plasmid pCBG99-Basic (Promega, WI, USA) with primers XbaI CBG99 forward 5'-ATTATCTAGAACCGCCATGGTGAAGCGTGAGAAAAATGTC-3' and XbaI CBG99 reverse 5'-

ATTATCTAGACTAACCGCCGGCCTTCTCCAACAATTG-3'. These products were digested with XbaI and cloned into the XbaI site of FUW (gift of D. Baltimore). Clones were screened for forward orientation of the cDNA. Luc2 was PCR amplified from the pGL4.10 vector (Promega, WI, USA) with EcoRI and BamHI compatible ends and the resulting PCR product was digested and ligated into the EcoRI and BamHI multiple cloning site of pLVX-EF1a-IRES-mCherry (Clontech, CA, USA). Plasmids Fucci C mKO2-hCdt1(30/120)/pCSII-EF-MCS and Fucci D mAcGFP-hGeminin(1/110)/pCSII-EF-MCS were a gift of A. Miyawaki (23).

4.3.3 Spheroid co-culture model

We formed spheroids in 384-well low volume, non-adhesive, round bottom plates (Corning Incorporated #3676, Corning, NY, USA), which we sterilized with UV radiation. To form spheroids, we collected cells via trypsinization, neutralized trypsin with serum-containing growth medium, centrifuged cells and aspirated medium to remove trypsin and serum, and re-suspended cells in low serum phenol red free spheroid medium. Spheroid medium contains phenol red free DMEM (#31053, Life Technologies) supplemented with 1% FBS (HyClone), 0.1nM estrogen, penicillin/streptomycin/glutamine (Life Technologies), and pyruvate to match all but the serum content and phenol in standard growth medium. We seeded each well with 1% MDA-MB-231 or 5% T47D cells expressing CBGreen FUCCI cells and the balance HS5s or HMFs expressing CBRed totaling 3,000 cells (200-300μm diameter spheroids). The difference in percentage of cancer cells is based on initial viability of cells after seeding spheroids and brightness of CBGreen expression to optimize dual-color measurements. For both spheroid maintenance and drug treatments, we replaced spheroid media in each plate every other day for the duration of an experiment by removing up to 20μl from each well and replacing it with 20μl fresh

spheroid medium. For long-term culture, we filled the outside wells around the periphery of the plate with medium only to minimize evaporation within experimental wells. We replicated each experimental condition in 4-7 wells and performed experiments at least twice. We distributed controls both on the interior and exterior of each plate.

We highlight the simplicity and flexibility of using existing, relatively low-cost, low-binding 384 round bottom plates to form co-culture spheroids and induce cancer cell quiescence. Facile, long-term culture is necessary for following quiescent cells, as changes in growth or death are prolonged. While the plates we selected were developed for chemical assays, the low-binding surface and optimal geometry facilitate singular uniform spheroid formation. Spheroids in this format form rapidly (<24 hours); are stable at least 16 days; and are amenable to high throughput robotic manipulation and/or analyses (bioluminescence, fluorescence, colorimetric, etc). Historically, multiple spheroids have been formed in lower-throughput, non-adherent 96 well plates. However, the larger volumes of these wells and movement of spheroids within a well limited the ease of exchanging medium, spheroid collection, and imaging. With our system, spheroids are geometrically restricted to the bottom and center of the small wells, facilitating rapid, albeit incomplete media exchange. We have adapted this spheroid culture to multiple cell types, including multiple cell-type co-cultures as we have described here. The flexibility of this system can be applied to many cell types, including, but not limited to, HS5 and HMF stromal cells, as we show here. We highlight the ability to control growth kinetics of cancer cells depending on the stromal cell type.

4.3.4 In vitro drug treatments

We formed spheroids for two days in spheroid medium before beginning treatments with compounds at indicated concentrations. To establish baseline bioluminescence before treatment, we quantified bioluminescence in 2-4 columns of each plate before adding compounds to remaining wells. We exchanged medium with fresh compounds diluted in spheroid medium every other day. For the treatment and recovery experiments, we imaged bioluminescence after 8 days of treatment and then exchanged 20 µl of media three times, which removes >99% of luciferin and drugs from each well. For recovery we continued exchange with fresh medium every other day.

4.3.5 Quiescence, dissociation, and colony outgrowth

To test reversibility of cancer cell quiescence, we formed spheroids of MDA-MB-231 or T47D cells as described above. After 2 and 10 days in spheroid culture, we performed two-photon fluorescence microscopy of spheroids cell cycle status based on FUCCI reporters (orange, G1; green, S/G2/M). On the same days, we dissociated parallel spheroids for colony outgrowth in optimal 2D growth conditions with full serum medium. To dissociate spheroids, we collected spheroids from a 384 well plate, washed in excess PBS, aspirated PBS, trypsinized briefly, and plated dissociated cells in 6 well plates containing full growth medium. After allowing 1, 4, and 8 days in adherent culture we imaged FUCCI status of colonies using epifluorescence and subsequent bioluminescence. For bioluminescence in 2D cultures, we used 1:100 final dilution of 150 µg/ml luciferin. We note that faster outgrowth of cancer cells in 2D cultures required discounting the CBRed image due to substantial CBGreen signal. After bioluminescence imaging, we replaced medium to remove luciferin.

4.3.6 Animal models of bone metastasis and drug treatment

All animal procedures were approved by the University of Michigan Committee for the Use and Care of Animals. To model bone metastases in mice, we delivered 1 x 10^5 MDA-MB-231 cells expressing CBRed and FUCCI in 100 µl 0.9% NaCl solution via intracardiac injection into the left ventricle of 5-9 week old female NSG mice. We quantified bone metastases by bioluminescence imaging (24).

We followed three separate protocols for dosing and observing mice. For monitoring the effect of trametinib on cell cycle status of MDA-MB-231 cells in bone marrow, we allowed metastases to establish for 16 days. Thereafter, we treated daily with trametinib (1 mg/kg by oral gavage) or vehicle control for 11 days at which time we recovered tissues for flow cytometry and/or *ex vivo* microscopy. For treatment with trametinib and/or doxorubicin, we began dosing either 3 or 7 days after intracardiac injection of cancer cells in experiments with few cancer cells or larger metastases, respectively. We administered a single dose of doxorubicin (5 mg/kg i.p.) or vehicle control. We used only a single dose of doxorubicin because multiple doses of this drug are toxic to NSG mice. We treated mice with 1 mg/kg trametinib by oral gavage daily for 5 days beginning at the same time as dosing with doxorubicin. For all experiments, we formulated trametinib for gavage as described (25, 26). Control mice received vehicle for both doxorubicin and trametinib in combination treatment studies.

4.3.7 Flow cytometery for FUCCI analysis

To analyze the cell cycle status of cancer cells expressing the FUCCI reporter using flow cytometry, we collected spheroids from 384 wells of each stromal culture condition (HS5 and HS27A). We allowed spheroids to settle, aspirated excess media, washed with an

excess of PBS, allowed the cells to settle again, aspirated, and gently dissociated spheroids in Accumax per the manufacturer's protocol. As a benchmark for FACS gating, MDA-MB-231 cells that were plated 24 hours prior were collected at ~80% confluence. Gating was set such that ~50% of the single positive cells (mKO only or AcGFP only) from 2D mono-culture were in S/G2/M. This gating matches our microscopy-based measure of cell cycle distributions. For flow cytometry analysis of bone marrow, we used PBS to flush bone marrow from the femur and tibia as described (27). We analyzed $1x10^4$ events for spheroids and 5×10^5 events for bone marrow samples. Flow cytometry was performed on a BD FACS Aria II (Becton Dickenson, Franklin Lakes, NJ).

4.3.8 Click Beetle Red and Green Bioluminescence Imaging

We captured all bioluminescence images with an IVIS Lumina Series III (Perkin Elmer, Waltham, MA, USA) and analyzed data with Living Image 4.3.1. We separated signals from click beetle red and green luciferase as discussed previously (28). Briefly, we replaced 5 µl of each 384 well with a 1:4 dilution of 150 µg/ml luciferin, resulting in 1:20 final dilution of luciferin. After incubating at 37°C for 5 minutes, we captured a 3-5 minute exposure with medium binning and either 520nm or 680nm band pass filters. For imaging in 2D standard culture conditions we used 1:100 final dilution of luciferin.

4.3.9 Fluorescence Microscopy

We captured all microscopic images of spheroids with an upright Olympus MPE using a 25X NIR corrected objective (XLPLN25XWMP, NA=1.05, Olympus, Tokyo, Japan). To facilitate semi-high-throughput upright immersion microscopy, we transferred spheroids from 384 well plates to low aspect ratio wells as we described previously (29). For images

of hCDT-mKO and hGeminin-AcGFP (FUCCI) cells, we used 920nm excitation and collected emitted light in green (495-540nm) and red (575-630nm) channels. For imaging cells expressing mCherry, we used 740 nm excitation. To limit signal attenuation throughout 150 μm stacks (5μm step size), we used the Olympus Bright-Z function to adjust laser transmission to the sample and detector gain to maximize signal per slice as we have demonstrated previously (29). We used the same acquisition parameters for all spheroids compared within a single experiment. For epifluorescence images, we used an Olympus IX70 microscope with a 10X objective, imaging red and green channels as we have described previously (30).

For imaging of mouse bone metastases, we removed femurs and rapidly cleaned the bone of adherent soft tissues. Using a Dremel Stylus and a small rounded tip, we gently removed cortical bone overlying sites of breast cancer cells identified by bioluminescence imaging. We imaged breast cancer cells by two photon microscopy as described for spheroids.

4.3.10 Data processing, plotting, and statistics

We used Microsoft Excel (Seattle, WA, USA) to process bioluminescence photon flux data before plotting data using GraphPad Prism (San Diego, CA, USA). GraphPad Prism was also used for calculating statistics. Using GraphPad Prism, we also estimated IC_{50}'s using four-parameter non-linear regression without weighting on log-transformed concentration data. We generated surface plots with the surf function in MATLAB. All graphs display mean values ± standard error of the mean (S.E.M.) unless stated otherwise. We normalized curves to photon flux measurements obtained 2 and 10 days post seeding for growth and cytotoxicity assays, respectively. We propagated errors along each point for normalization.

We calculated well-by-well selectivity of compounds by taking the log2 transform of CBRed flux (R) divided by CBGreen flux (G). The log2 transformation normalizes the distribution and facilitates visualization of results. We then subtract the log2 ratio of the untreated control, which adjusts for differences in baseline CBRed and CBGreen brightness. Negative selectivity corresponds to either preferential growth of the CBGreen cancer cells or death of the CBRed HS5s.

To quantify the fraction of cells in S/G2/M cells using the FUCCI reporter, a person blinded to experimental conditions manually counted the number of red or green cells using images with pseudo-colored overlay. For 2D cultures, we quantified a single slice for multiple view fields. For spheroids, we quantified a slice every 15 μm through a 150 μm volume. We calculated the ratio of cells in G1/0 by dividing the number of green (G) cells divided by total orange and green (R+G) for each image. We noted very few cells with both green and orange, and we discounted these cells from calculations. For statistical comparisons of 2D monoculture and 3D co-culture FUCCI ratios we applied the t-test in GraphPad Prism.

4.3.11 Cytokine Array

We seeded 5 x10^5 HS5 cells in a 35 mm dish in full growth medium. After cells adhered overnight, we washed once with PBS and replaced the media with DMEM containing 0.2% albumin (Probumin, EMD Millipore, Billerica, MA, USA) and penicillin/streptomycin/glutamine. After 24 hours, we collected supernatants and for analysis with the Proteome Profiler Human Cytokine Array Kit, Panel A (R&D Systems, Minneapolis, MN, USA). We used ImageJ to quantify area under the curve for array spots for two independent spots for each cytokine.

4.4 Results

4.4.1 Co-culture spheroids induce growth of cancer cells or reversible quiescence

We combined breast cancer cells (1-5% of total cells) with human bone marrow stromal cells (HS5, HS27A), or human mammary fibroblasts (HMF) in non-adherent 384 well plates. This low percentage of breast cancer cells in spheroids models the small numbers of cancer cells typically found in bone marrow while still giving sufficient signal for imaging. All stromal types formed uniform, compact spheroids by 24 (Supplemental Fig. C.1) hours and remained stable for at least 16 days. MDA-MB-231 cells, a triple-negative cell line, grew differently in HS5, HS27A, or HMF spheroids as quantified by green click beetle luciferase (Fig. 4.1A, $p < 0.0001$). Long doubling times for MDA-MB-231 cells in spheroids (9.1, 2.4, and 3.3 days, corresponding to 1.8, 10.3, and 5.4-fold change over 8 days) contrast starkly with 24 hour doubling in 2D mono-culture as we (Fig. 4.1D) and others report (31). Doubling times for cell lines representing three other breast cancer subtypes (MDA-MB-468, triple-negative; SKBR3, Her2 amplified; and T47D, ER^+/PR^+) also were prolonged in spheroids, ranging from 5.4-10.2 days (corresponding to 2.8-1.7 fold change, respectively, over 8 days), regardless of stromal cell type (Fig. 4.1A). Additionally, growth is increased for MDA-MB-231 cells with all stromal cell types by increasing the percentage of fetal bovine serum in the cultures from 1 to 10% ($p <0.0001$; Supplemental Fig. C.5A-B). However, with increased fetal bovine serum the trends in cancer cell growth between stromal cell types remain with increasing growth in the order of HS5 < HS27A ($p < 0.0001$). To test whether the HS5 cells were essential for viability of MDA-MB-231 cells, we

measured growth of the same number of cancer cells alone in non-adherent suspension culture (Supplemental Fig. C.1B). Without stromal support the MDA-MB-231 cells quickly die, suggesting that HS5 cells limit growth of breast cancer cells while maintaining viability. This is in contrast to previous reports showing HS5 and HS27A conditioned medium initiates apoptosis of cancer cells (13). In our system the stromal cells were necessary to maintain the cancer population.

To further validate quiescence of cancer cells, we used an established fluorescent cell cycle indicator (FUCCI) to show that MDA-MB-231 and T47D cells arrested in G1 by day 2 in HS5 spheroids relative to 2D culture (Fig. 4.1B-C, Supplemental Fig. C.2) (23). Despite quiescence of breast cancer cells after 2 or 10 days in HS5 spheroids, both MDA-MB-231 and T47D cells remained viable, as evidenced by doubling times of ~0.9 and 1.5-2 days, respectively, after dissociating spheroids and returning cells to 2D culture (Fig. 4.1D-E). Limited 3D growth and substantial 2D growth of T47D cells suggests these cells are more quiescent in spheroid cultures and may better reflect the likelihood of ER^+ cells to contribute to relapse. After dissociating co-culture spheroids, cancer cells resume growth despite the presence of HS5 cells in 2D culture, suggesting quiescence is induced by 3D interactions between cancer and stromal cells.

4.4.2 Dual-color click beetle luciferase imaging of two cell populations

To quantify effects of compounds on cancer versus stromal cells in intact spheroids, we implemented dual-color bioluminescence imaging with click beetle green (CBGreen) and red (CBRed) luciferases (32) (Fig. 4.2). Similar to firefly luciferase, click beetle green and red luciferases are ATP-dependent enzymes that sensitively quantify relative numbers of viable cells. To characterize our ability to measure dual-color luciferase activity without

spectral deconvolution, we generated spheroids with increasing percentages of MDA-MB-231 or HS5 cells expressing CBGreen or CBRed, respectively. Based on the spectral overlap of CBGreen and CBRed (Fig. 4.2A), we acquired images with filters centered at 520 and 680 nm. An increasing fraction of CBGreen cells produces linearly increasing signal measured in the 520 (green) and 680 nm (red) channels (Fig. 4.2B, Supplemental Fig. C.3 A-E). The CBGreen signal is an order of magnitude less than CBRed when cancer cells are seeded at 1-10% of total cells in a spheroid (Fig. 3.2B, Supplemental Fig. C.3A). Conversely, increasing the fraction of CBRed HS5 cells in spheroids of unmarked HS5 cells produced negligible overlap in the 520 nm channel with linearly increasing detection in the 680 nm channel (Fig. 4.2B, Supplemental Fig. C.3B). These results established that CBRed does not leak into our CBGreen channel. Only when more than 10% cancer cells are present in a spheroid does signal from CBGreen luciferase contribute substantially to signal from CBRed luciferase in the 680 nm channel. To avoid this problem, we maintained low levels (1-5%) of cancer cells with CBGreen luciferase in all spheroid experiments.

4.4.3 Selective elimination of proliferating and quiescent cancer cells with cytotoxic and targeted therapies

We initially tested standard chemotherapy drugs against quiescent and proliferating breast cancer cells in bone marrow spheroids, using CBGreen and CBRed to quantify relative cytotoxicity to each population. To visualize the effects of drugs, we plotted the untreated- and background-normalized dose-response curves for both cancer CBGreen and the stromal CBRed components, for both HS-5 and HS-27 co-cultures (Fig. 4.2C-D). To quantify selectivity of a drug for cancer cells at defined concentrations, we calculated the log-2-scale ratio of CBRed (stromal) to CBGreen (cancer) bioluminescence. Log-2

normalization is typical for bioinformatics measures that compare to internal references (33) and for biological samples where doubling is physiological. Selectivity is always zero for untreated spheroids as both dose-response curves start at one. Bioluminescence < 1% of starting values produces high variability as the signal is close to background of the imaging system, so we removed these selectivity points from graphs.

To compare effects of a compound to selectively eliminate MDA-MB-231 cells in co-cultures with HS5 or HS27A cells, we plotted the CBGreen (cancer) dose-response and corresponding selectivity from both stromal cell types on the same plot (Fig. 4.3; green and black curves from Fig. 4.2C-D combined into Fig. 4.3C). Treatment with cisplatin, paclitaxel, and doxorubicin produced typical sigmoidal cytotoxicity curves for MDA-MB-231 cells within HS5 and HS27A spheroids (Fig. 4.3A-C). Cisplatin produced markedly higher IC_{50} values for quiescent MDA-MB-231 cells than their counterpart HS5 cells, reflecting negative selectivity and greater toxicity of this drug to HS5s (Fig. 4.3A,C; IC_{50}'s summarized in Supplemental Fig. C.10). By comparison, these drugs had lower IC_{50} values and positive selectivity for MDA-MB-231 cells relative to HS27A cells, likely due to greater proliferation of the cancer cells in this environment. Doxorubicin was the only cytotoxic therapy to have highly positive selectivity against MDA-MB-231 cells in HS27A spheroids and non-negative selectivity when cultured with HS5 cells. Unlike the mainly cell cycle-based mechanism for cytotoxicity of cisplatin and paclitaxel, doxorubicin has multiple mechanisms including both cell cycle-based (intercalating DNA) and mitochondrial-based effects (34). We also measured a similar IC_{50} shift for MDA-MB-231 cells proliferating in HMF spheroids as compared with quiescent of cancer cells in HS5 spheroids (Supplemental Fig. C.1D). Quiescent T47D cells responded similarly to MDA-MB-231 cells cultured in HS5 spheroids

(Supplemental Fig. C.4A-C). Overall, only doxorubicin showed modest selectivity in eliminating proliferating and quiescent MDA-MB-231 cells and quiescent T47Ds. These data show that looking at IC_{50} shifts along with selective elimination of cancer cells is more informative than IC_{50} shift only.

We also targeted constitutively active KRas in MDA-MB-231 cells with PD0325901, an inhibitor of the downstream mitogen activated protein kinase, MEK (35). While PD0325901 selectively eliminated MDA-MB-231 cells in both quiescent and proliferative settings, selectivity increased and the IC_{50} value decreased for eliminating quiescent MDA-MB-231 cells in HS5 spheroids as compared with proliferating cancer cells in HS27A spheroids (Fig. 4.3D). This result is opposite to effects of doxorubicin in these two different bone marrow environments. The trends in efficacy and selectivity between doxorubicin and PD0325901 become more pronounced when proliferation is stimulated by adding 10% serum to spheroid cultures (Supplemental Fig. C.5). The IC_{50} and selectivity of PD0325901 for MDA-MB-231 cells decreased with additional serum stimulating growth, suggesting reduced dependence on MEK signaling. The opposite was true for doxorubicin, again supporting that the drug preferentially affects dividing cells, but maintains activity against quiescent cells.

4.4.4 Limited or non-selective effect for many cancer compounds

A provocative result revealed by our dual-color spheroid system was that many compounds and drugs developed to eliminate proliferating cancer cells were ineffective against quiescent cancer cells in spheroids. These compounds include inhibitors of PI3-kinase, mTOR, TGF-β, Her2, and CXCR4 (Tables C.1-4). Notably, estrogen receptor (ER) inhibitors did not affect quiescent ER+ T47D cells in bone marrow spheroids, which

parallels persistence of breast cancer cells in patients treated with these drugs. Additionally, we found several compounds with non-selective toxicity to both cancer cells and stromal cells (Supplemental Fig. C.7-8) or preferential elimination of stromal cells (PI3-kinase inhibitor GDC-0491) (Supplemental Fig. C.7B, C.8B). These results highlight the utility of our dual color imaging strategy to differentially measure effects of various targeted compounds on quiescent cancer versus stromal cells.

4.4.5 Drug combinations increase selectivity in vitro

We tested combination treatments to expand the therapeutic window for doxorubicin against quiescent MDA-MB-231 cells. We incubated cells with increasing concentrations of PD0325901 and doxorubicin alone or in combination for 8 days and quantified selectivity. After removing drugs, we also cultured spheroids for an additional 6 days to identify delayed effects on cell viability, similar to patients treated with intermittent cycles of chemotherapy. 3D surface plots showed that treatment with PD0325901 alone produced a maximum selectivity of ~4.0 at 100nM after 8 days (Fig. 4.4A). Interestingly, selectivity for doxorubicin against cancer cells increased after 6 days of recovery (Fig. 4.4B). Conversely, selectivity for intermediate concentrations of PD0325901 decreased after recovery, perhaps due to cytostatic rather than cytotoxic effects at sub-lethal concentrations of this compound. Treatment with 100nM PD0325901 and 1μM doxorubicin produced additive effects with peak selectivity of 6.6 after recovery. MEK activation has been shown to be a compensatory response to doxorubicin treatment in multiple types of cancer, so combination treatment with PD0325901 can block this potential mechanism of drug resistance (36-38). These results also show cancer burden is reflected accurately by imaging after 8 days of treatment. Post treatment rebound is

minimized due to more effective elimination of cancer cells with the combination of doxorubicin and PD0325901.

We also targeted Jak2 signaling in MDA-MB-231 cells since HS5 cells constitutively secrete IL6, a known activator of Jak2-Stat3 signaling in breast cancer progression (Supplemental Fig. C.6A-C) (39, 40). While treatment with the Jak2 inhibitor AG490 produced minimal selectivity for cancer cells, we observed highest post-recovery selectivity for AG490 combined with doxorubicin (Supplemental Fig. C.6B-C). These results highlight how our system can identify combinations of compounds with greater toxicity to quiescent cancer versus stromal cells.

4.4.6 Modeling and imaging bone marrow metastasis

To model formation of metastases and drug response in mice, we delivered MDA-MB-231 cells carrying both FUCCI and CBGreen via intracardiac injection. By one week ~80% of mice carried bone marrow metastases detectable by bioluminescence. We observed quiescent cells in metastases in bone marrow based on *ex vivo* two photon imaging of cell cycle status (Fig. 4.5A-C). Most metastases were located near metaphases of bone, but the size, cell density, microenvironment, and cell cycle status of separate lesions varied greatly. As representative examples, we found small metastases comprised predominantly of cells in G1/G0 near the endosteum of bone (Fig. 4.5A). Large, cell-dense, established metastases showed a proliferative exterior and cell cycle arrested interior, similar to the stratifications in a primary tumor (Fig. 4.5B). We also observed proliferating breast cancer cells near blood vessels and bone marrow stroma (Fig 4.5C). These images demonstrate the presence of quiescent and proliferating environments in bone marrow, comparable to our spheroid models and prior studies on hematopoietic stem cells (41, 42).

To verify these imaging findings, we recovered bone marrow from tumor-bearing mice and analyzed cell cycle status by flow cytometry (Fig. 4.5D-E; Supplemental Fig. C.9). Approximately 10% of MDA-MB-231 cells from bone marrow were in S/G2/M (Fig. 4.5D), comparable to the percentage measured by two photon microscopy and flow cytometry in MDA-MB-231 cells co-cultured with HS5 cells in spheroids (Fig. 4.1B, Supplemental Fig. C.2). Daily treatment with trametinib, a clinically approved MEK inhibitor that closely replicates kinetics and functions of PD0325901, shifted essentially all breast cancer cells to G1/G0 phase of the cell cycle and decreased the total amount of cancer cells in bone marrow (Fig 4.5D-G). These data indicate that trametinib diminishes cancer burden in both quiescent and proliferative bone marrow environments, paralleling results in spheroids.

4.4.7 Bone marrow spheroid model predicts combination therapy effective against bone marrow metastases.

We tested combination therapy with MEK inhibition and doxorubicin on experimental bone metastases with MDA-MB-231 cells. To replicate limited numbers of cancer cells in bone marrow, we began treatment three days after intracardiac injection of cancer cells. We treated mice with either a single dose of doxorubicin, four doses of trametinib, both drugs, or vehicle only. We used bioluminescence to quantify bone metastases and regrowth. After treatment of mice (8 days post-intracadiac injection) and an additional week of no treatment, we recovered and dissociated bone marrow from lower extremities and allowed outgrowth of cancer cells in standard 2D cell culture. Combination treatment with doxorubicin and trametinib completely eliminated outgrowth of MDA-MB-231 cells *in vitro* with 0/8 legs measuring positive for cancer cells (Fig. 4.6D-E). Doxorubicin and trametinib individually reduced the numbers of mice with viable cancer

cells in lower extremity bone marrow to 3/8 and 5/11, respectively, as compared to 7/10 for the vehicle (Fig. 4.6A-C,E). For bone marrow plates, trametinib, doxorubicin, and their combination significantly decreased growth of bioluminescent cancer cells *in vitro* by 86%, 99%, and 100% as compared to vehicle ($p < 0.05$).

In a separate experiment, we tested these same drug treatments in mice with larger metastases established 7 days after intracardiac injection. While single agent therapy showed a trend toward reduced tumor burden in bone, only combined treatment with trametinib and doxorubicin statistically lowered growth compared with vehicle control (Fig. C.11C; $p < 0.01$). Combination therapy was most effective in a subset of metastases, as highlighted by responsive lesions below the dotted line in Figure C.11C, which correspond to the top pair of bioluminescence images in Figure C.11B. The partial response may be due to heterogeneity of microenvironments in bone marrow (see Fig 4.5A-C). Variations in response also may reflect that large and/or growing metastases dominate the bioluminescent signal.

4.5 Discussion

Eliminating quiescent cancer cells is a major challenge to successfully and completely eradicate cancer from patients for at least three reasons. Firstly, drugs are typically designed to target functions of rapidly dividing cells (e.g. mitosis, DNA replication/repair, growth signals) but not quiescent cancer cells. Secondly, malignant cells are housed in protective microenvironments (e.g. bone marrow), which may contribute to quiescence or other resistance phenotypes. Thirdly, dosing is often attenuated or terminated due to toxicity to other tissues, such as the hematopoietic system. Therefore, experimental models are needed to identify and test therapies to eliminate quiescent

cancer cells while sparing stromal cells within a representative microenvironment. Our bone marrow model addresses these shortcomings for drug screening by providing a facile approach to test compounds selectively targeting quiescent or dividing cancer cells but not the surrounding bone stromal cells. The novelty of our system is three-fold: 1) we establish a simple but flexible model of cancer cell quiescence in a 3D environment; 2) we use multiple modes of imaging to monitor cell cycle status and viability of both cancer and stromal cells; and 3) we investigate single and combinatorial treatments to identify compounds that selectively eliminate quiescent cancer cells. Data from our animal model indicate the spheroid system can identify treatments effective against cancer cells in actual bone marrow environments.

As compared with other existing co-culture systems, our 3D bone marrow spheroid model is simple, reproducible and amenable to high throughput applications. Several systems exist on a continuum of complexity for recreating the microenvironment of the bone marrow environment. These assays include standard 2D assays (16), 3D spheroids, and more complicated Gelfoam™ 3D biomatrix-based assays (20). Co-culture 2D assays are less than physiological in terms of cell-cell interactions, substrate stiffness, induction of quiescence, and replication of a 3D environment *in vivo*. Here we confirm and build upon our previous results that cancer cells grow more slowly in 3D co-cultures as compared to 2D (21). 3D spheroids better reproduce parameters including hypoxia, cell-cell contacts, stiffness, and concentration of secreted factors, which may contribute to differences in growth based on dimensionality. However, optimizing spheroid uniformity, ease of use, and throughput has been an area of substantial work in the past several decades. We have developed several systems for establishing defined, uniform, and stable spheroids in both

microfluidic channels (21) and a high throughput 384 hanging drop plate (43, 44). These systems have challenges of throughput and stability, respectively. Other methods for spheroid assays also are limited by ease of use and throughput, including rotary flasks, non-adherent dishes, or other more advanced surface or device configurations (17, 18). We describe additional practical considerations and advantages of our system in the Methods.

We leveraged our spheroid system and fluorescence and bioluminescence imaging modalities to monitor cancer cell quiescence and viability of both cancer and stromal cells. Firstly, we used two-photon imaging of spheroids to monitor cell cycle arrest of cancer cells with an established fluorescent ubiquitin-based cell cycle indicator (FUCCI) (23). Using this strategy we confirmed that cancer cells reversibly arrested in G0/1 in spheroids with HS5 bone stromal cells. Secondly, we optimized dual-color click beetle luciferase imaging to measure two cell populations without spectral deconvolution. The high sensitivity of bioluminescence imaging allowed us to readily measure very low numbers of cancer cells (30-150 cells per spheroid, or 1-5% of total cells). By forming spheroids with few cancer cells, we not only modeled rare numbers of quiescent cancer cells in bone marrow but also cleanly separated click beetle green and red bioluminescence from cancer and stromal cells, respectively.

Although few tested compounds effectively or selectively eliminated cancer cells, we found combinations of therapies that improved elimination of MDA-MB-231 cells after sequential dosing and recovery for six and eight days, respectively. By measuring selectivity of responses, we also found that an inhibitor of Jak2-Stat3 only selectively eliminated cancer cells in combination with doxorubicin. The MEK inhibitor PD0325901 produced strongly selective reduction of MDA-MB-231 burden, particularly in combination

with doxorubicin. Multiple reports show compensatory MEK-dependent response upon challenge with doxorubicin (36-38). Combination of sub-maximal doses of both doxorubicin and PD0325901 may limit toxicities and improve elimination of cancer cells from bone marrow. Several lines of evidence support that MDA-MB-231 cells become additionally dependent on MEK signaling both while quiescent in HS5 co-cultures and stressed via doxorubicin. Firstly, efficacy of PD0325901 is diminished in growth supportive environments with increased serum and HS27A co-culture. Secondly, selective elimination of cancer cells persisted after six days of compound-free recovery only when PD0325901 was combined with doxorubicin. These data suggest that challenge with doxorubicin or quiescence culture conditions suppress growth and make cancer cells more susceptible to MEK inhibition.

We highlight three aspects of our bone marrow model system as it relates to replicating bone marrow metastases. Firstly, our *in vitro* models of cancer growth and quiescence begin to capture the heterogeneity of bone marrow microenvironments and their resulting phenotypes. Screening for drugs that selectively eliminate cancer cells in multiple stromal support conditions will better predict successful treatment of bulk, growing disease, and quiescent cells that contribute to late relapse. Secondly, our in vitro spheroid model with HS5 cells showed ≈ 90% of MDA-MB-231 cells in G1/G0, comparable to that quantified for cancer cells recovered from mouse bone marrow. Finally, the combination treatment with a MEK inhibitor and doxorubicin effectively eliminated breast cancer cells in bone marrow as predicted by our *in vitro* model. Our *in vitro* model predicted *in vivo* decrease of tumor cell burden upon single agent treatment with trametinib or doxorubicin. More provocatively, our *in vitro* model predicted substantial

outgrowth of cancer cells post-treatment for single agent therapy but near total elimination with dual therapy. Together these data suggest that our *in vitro* system begins to capture the quiescent phenotype and heterogeneity of responses in the bone marrow.

Results from our model system highlight the value of combined fluorescence and bioluminescence imaging to reveal effects of treatment. Bioluminescence imaging provides a real time measure of relative cancer burden in spheroids and mice. Additionally, we use bioluminescence to locate *in vivo* metastases for fluorescence imaging of cell cycle status within different bone marrow locations. Pairing bioluminescence-based *in vivo* location and burden with fluorescence-based analyses of cell-level status provides a detailed view of treatment efficacy. This optical imaging strategy is amenable to many other bioluminescent and fluorescent reporters, such as tracking receptor-ligand binding via bioluminescence (45) and/or apoptosis via fluorescence (46). We expect further testing with this spheroid model and multi-modal imaging will reveal additional compounds and/or combinations to effectively eliminate quiescent cancer cells while sparing stromal cells.

Our high throughput, simple, long-term, 3D model of cancer cell quiescence is a significant advance over previous 2D systems and existing, more complex 3D models. The system facilitates maintenance of 384 well format cultures for at least 16 days, which enables extended dosing and recovery to identify optimal drugs and drug combinations effective against quiescent cells. These 3D culture and imaging strategies are amenable to high throughput screening and many other co-culture models. The system also could be modified to include cells expressing reporters of cellular and molecular events other than cell cycle status, thereby allowing real time imaging of drug targeting. Since many

screening strategies for new cancer drugs include secondary testing for effects against normal cells, our approach saves time and resources by combining efficacy against cancer and normal cells in one assay. Incorporating screening against quiescent cancer cells in a bone marrow environment early in drug development will increase probability of finding therapies independent of cell division and with lower toxicity to normal tissues. We expect our drug testing platform will help advance more effective, less toxic therapies to clinical trials and ultimately clinical oncology.

4.6 Figures

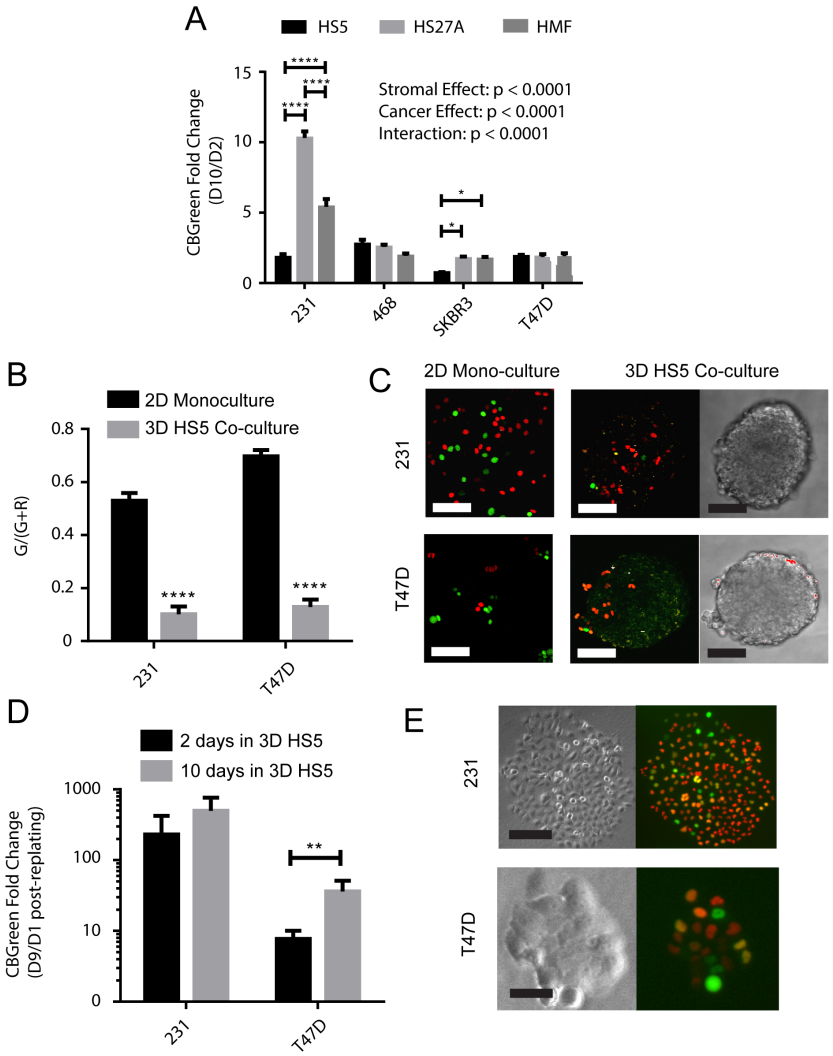

Figure 4.1. Long term spheroid culture with different stroma results in growth or reversible quiescence of cancer cells. (A) Stromal cells from human bone marrow (HS5, HS27A) and mammary tissue (HMF) support different levels of growth and/or quiescence as measured by bioluminescence fold change for four breast cancer cell lines (MDA-MB-231, MDA-MB-468, SKBR3, and T47D). Inset text lists the main variable effects (stroma, cancer, or their interactions) from 2-way ANOVA results and bars demarcate the *post hoc* Tukey test results (* p<0.05, **** p<0.0001). Presented data are mean + SEM for N = 28 pooled from two independent setups. (B) Cell cycle status of MDA-MB-231 or T47D breast cancer cells in 2D culture or HS5 spheroids (3D z-stack) based on genetically-encoded fluorescence ubiquination-based cell cycle indicators (FUCCI), which define cells in G1 and S/G2/M phases based on red or green fluorescence, respectively. Graph shows mean values + SEM for fraction of cells in S/G2/M, which decreases for cancer cells in HS5 spheroids (n = 9-13 spheroids pooled from two independent setups; t-test, * p<0.0001 between 2D and 3D for both cell types). (C) Representative images of MDA-MB-231 and T47D FUCCI cells in 2D and 3D culture, respectively. Scale bars demarcate 100 μm. (D) MDA-MB-231 or T47D cancer cells were cultured in HS5 spheroids for 2 or 10 days, dissociated as a co-culture, then returned to adherent 2D growth conditions for 8 days. The data are plotted as fold change in bioluminescence over 8 days in adherent 2D co-culture. Presented data are mean values + SEM (n = 6 measurements pooled from two independent setups, 4 spheroids dissociated per measurement). (E) Representative FUCCI images of outgrowth colonies from cancer cells described in panel D. Scale bars demarcate 200 μm and 50 μm for the MDA-MB-231 and T47D colonies, respectively.

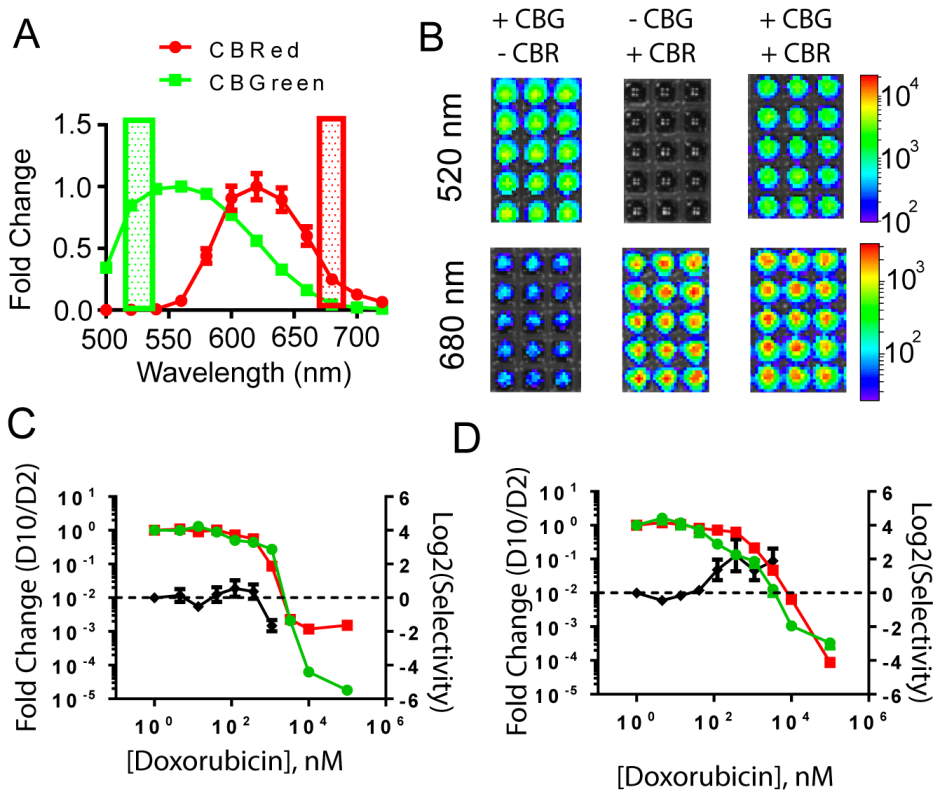

Figure 4.2. Validation of dual-color luciferase for monitoring selective response of cancer cells in bone marrow co-culture spheroids. (A) Representative bioluminescence spectra of MDA-MB-231 or HS5 cells expressing click beetle red or green luciferases, respectively. The spectra are normalized to their maxima for viewing purposes. Each data point represents mean ± SEM (n = 4 per point). (B) Representative log-scale pseudo-color images of 520nm and 680nm band pass filters for conditions of only CBGreen cells, only CBRed cells, or a mixture of the two. For the CBGreen only and mixture, the CBGreen cells are 10% of the total. See Figure S3 for more detailed characterization. (C-D) Graphs depict dose-response cytotoxicity of MDA-MB-231 cells (CBGreen, green curves) and their counterpart (C) HS5 and (D) HS27A cells (CBRed, red curves) after 8 days of treatment. After background subtraction, we normalized photon flux values for both CBGreen and CBRed luciferases in cancer and stromal cells, respectively, to their respective untreated controls. We calculated selective toxicity for cancer cells based on the log-2-scale ratio of CBRed to CBGreen signal adjusted to center around the untreated control (black curve). Positive values for selectivity (black curve) that lie above the horizontal dotted line denote selective loss of bioluminescence from cancer cells. As CBRed and CBGreen dose-response curves both decrease below 1% of untreated (fall below the horizontal line), we omit selectivity points because measurements are dominated by noise of the instrument.

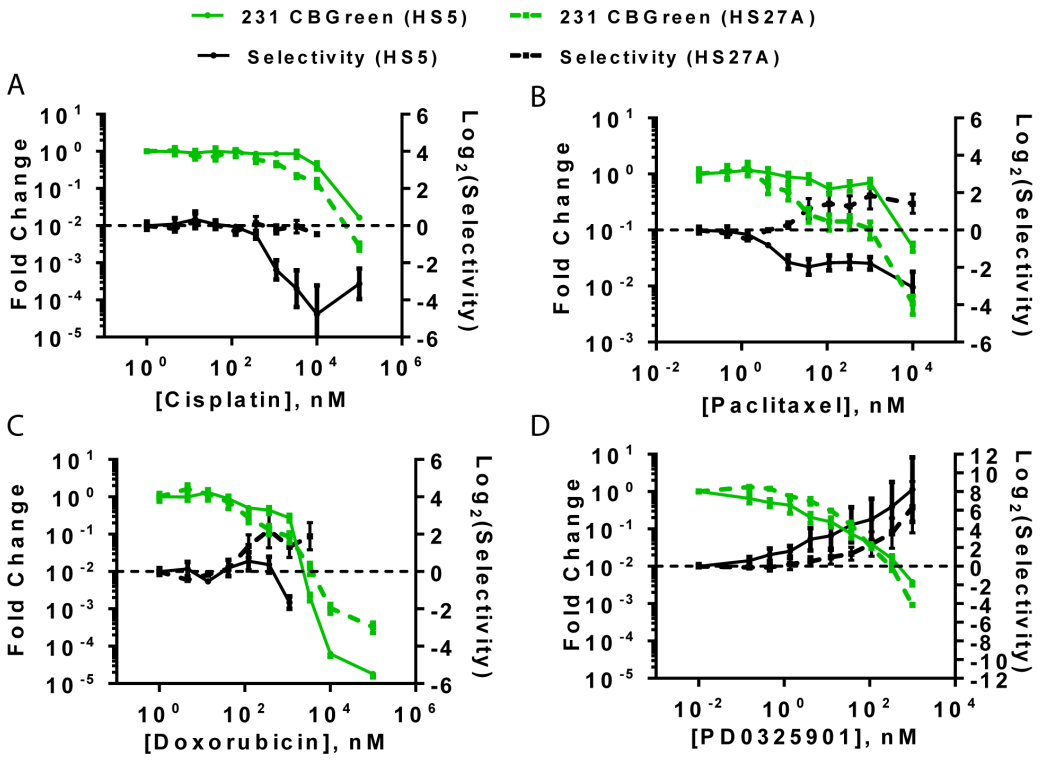

Figure 4.3. Treatment responses of cancer and stromal cells in spheroids. To directly demonstrate selective elimination of cancer cells in HS5 and HS27A co-cultures, we plotted the CBGreen dose-response and selectivity curves from HS5 and HS27A co-cultures (green and black curves from Fig. 2C-D) together on the same plot (C). (A-D) Graphs show dose-response cytoxicity for cisplatin (A), doxorubicin (B), paclitaxel (C), and PD0325901 (D) against MDA-MB-231 cells after 8 days of treatment in HS5 and HS27A spheroids (solid and dotted curves, respectively). Note that negative selectivity indicates that the counterpart CBRed stromal dose-response would be left-shifted relative to the depicted CBGreen curve. We present dose-response and selectivity curves as mean values ± SEM (n = 7 spheroids per condition).

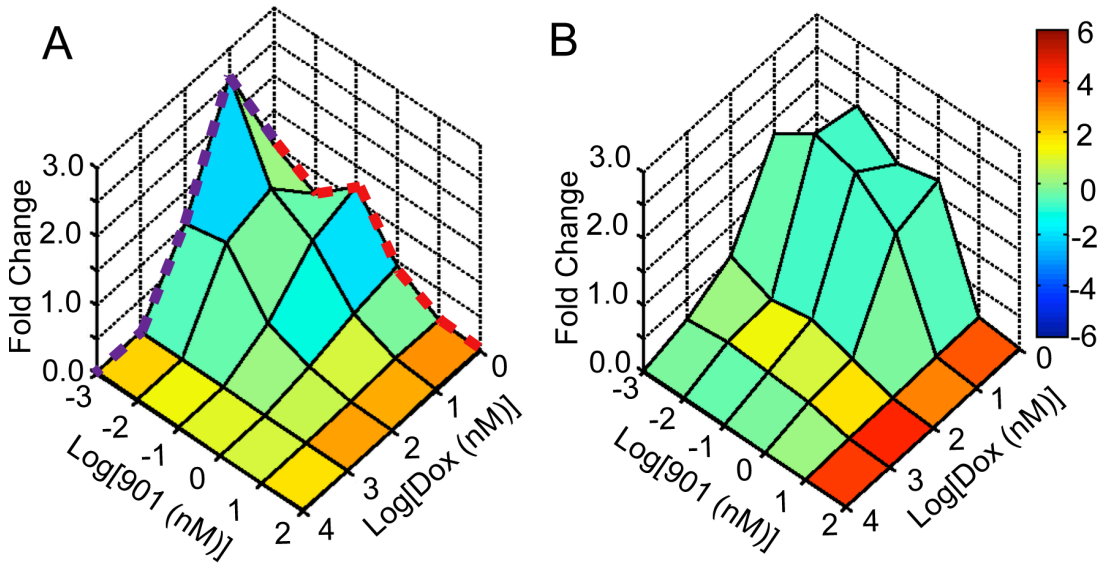

Figure 4.4. Dual-color click beetle bioluminescence reveals selectivity of combinatorial treatments on cancer versus stromal cells in bone marrow spheroids. Combinations produce enhanced selectivity after dose (A) and recovery (B). Surface plots show cancer cell bioluminescence (CBGreen) normalized to control after 8 days of treatment (A) and again after 6 days of recovery without compounds (B) for MDA-MB-231 cells treated with PD0325901 and doxorubicin. The dotted purple and red lines represent the doxorubicin only and PD0325901 only curves, respectively.

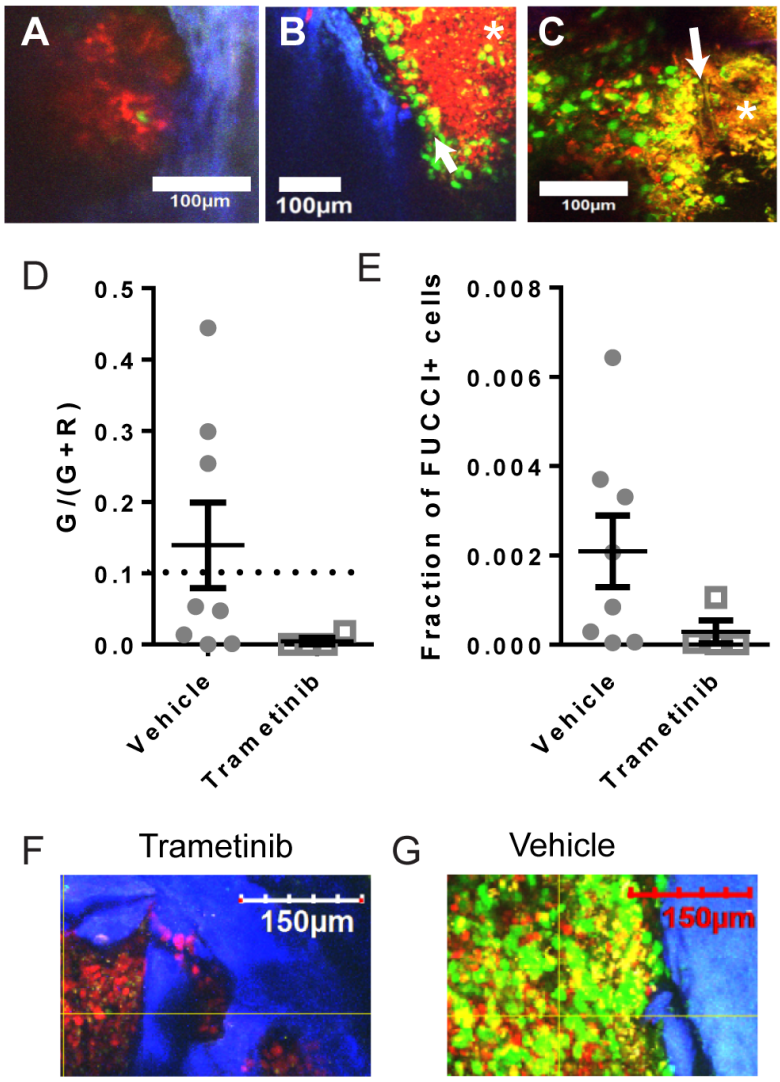

Figure 4.5. Heterogeneity of bone marrow microenvironment leads to different MDA-MB-231 cell cycle status and responsiveness to MEK inhibition. (A-C) Established bone metastases reveal heterogeneity of location and cell cycle status. Two photon microscopy showed (A) a quiescent bone lesion adjacent to bone; (B) large metastasis with growth arrested core (white *) and a cycling periphery (white arrow); and (C) diffusely populated, cycling cells adjacent to autofluorescent bone marrow stroma (white *) and a blood vessel (white arrow). Blue signal originates from collagen in the structural bone. (D, E) Daily dosing with trametinib decreased the (D) G/(G+R) fraction of cycling cells (C) and total burden of cancer cells in bone marrow as measured by flow cytometry. Example flow cytometry scatter plots and gating are found in Supplemental Fig. C.9. The horizontal dotted line in D depicts less than 10% cycling cells in S/G2/M. Presented data are mean + SEM for N = 8 and 4 for vehicle and trametinib, respectively. (F, G) Microscopy of femur bone marrow depicts cell cycle arrest of cancer cells in G1/G0 after trametinib treatment (F) as compared to vehicle (G). Scale bar denotes 100 μm (A, B) and 150 μm (F, G).

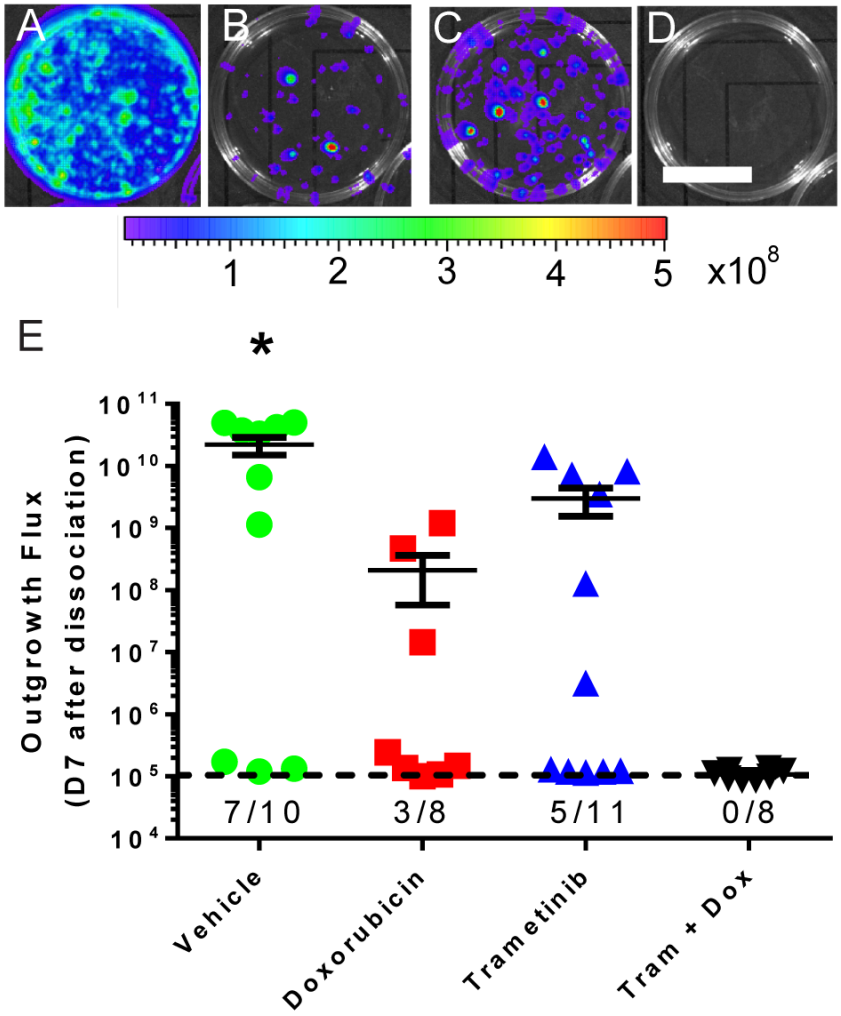

Figure 4.6. Bioluminescence reveals elimination of bone metastases with combination treatment with doxorubicin and trametinib. (A-D) Example pseudo-colored bioluminescence images dissociated bone marrow in 60 mm dishes after 7 days of culture for animals treated with vehicle (A), doxorubicin (B), trametinib (C), and dual doxorubicin and trametinib (D). Scale bar depicts 2 mm and color scale denotes photon flux values. (E) Flux measurements of outgrowth plates after single agent and combination treatments. The fraction below each dataset represents the fraction of lower extremities from which we detected cancer cells above background (dotted line at 10^5). The statistical demarcation shows difference between vehicle and all other samples, using multiple t-tests (* $p<0.05$) for the number of extremities listed in the denominator of the fractions. Other comparisons showed no statistical difference.

4.7 References

1. Alix-Panabières C, Riethdorf S, & Pantel K (2008) Circulating tumor cells and bone marrow micrometastasis. *Clinical Cancer Research* 14(16):5013-5021.
2. Leong SP & Tseng WW (2014) Micrometastatic cancer cells in lymph nodes, bone marrow, and blood: Clinical significance and biologic implications. *CA Cancer J Clin.* 64(3):195-206. doi: 110.3322/caac.21217. Epub 22014 Feb 21215.
3. Patel SA, Dave MA, Murthy RG, Helmy KY, & Rameshwar P (2011) Metastatic breast cancer cells in the bone marrow microenvironment: novel insights into oncoprotection. *Oncol Rev.* 5(2):93-102.
4. Zhang XH, Giuliano M, Trivedi MV, Schiff R, & Osborne CK (2013) Metastasis dormancy in estrogen receptor-positive breast cancer. *Clin Cancer Res.* 19(23):6389-6397. doi: 6310.1158/1078-0432.CCR-6313-0838.
5. Janni W*, et al.* (2011) Persistence of disseminated tumor cells in the bone marrow of breast cancer patients predicts increased risk for relapse—a European pooled analysis. *Clinical Cancer Research* 17(9):2967-2976.
6. Meads MB, Hazlehurst LA, & Dalton WS (2008) The bone marrow microenvironment as a tumor sanctuary and contributor to drug resistance. *Clin Cancer Res.* 14(9):2519-2526. doi: 2510.1158/1078-0432.CCR-2507-2223.
7. Ono M*, et al.* (2014) Exosomes from bone marrow mesenchymal stem cells contain a microRNA that promotes dormancy in metastatic breast cancer cells. *Science Signaling* 7(332):ra63.
8. Lim PK*, et al.* (2011) Gap junction-mediated import of microRNA from bone marrow stromal cells can elicit cell cycle quiescence in breast cancer cells. *Cancer Res.* 71(5):1550-1560. doi: 1510.1158/0008-5472.CAN-1510-2372. Epub 2011 Feb 1522.
9. Tjensvoll K*, et al.* (2012) Persistent tumor cells in bone marrow of non-metastatic breast cancer patients after primary surgery are associated with inferior outcome. *BMC Cancer.* 12:190.(doi):10.1186/1471-2407-1112-1190.
10. Morrison SJ & Scadden DT (2014) The bone marrow niche for haematopoietic stem cells. *Nature* 505(7483):327-334.
11. Graf L, Iwata M, & Torok-Storb B (2002) Gene expression profiling of the functionally distinct human bone marrow stromal cell lines HS-5 and HS-27a. *Blood* 100(4):1509-1511.
12. Roecklein BA & Torok-Storb B (1995) Functionally distinct human marrow stromal cell lines immortalized by transduction with the human papilloma virus E6/E7 genes. *Blood.* 85(4):997-1005.
13. Zhang C*, et al.* (2011) Paracrine factors produced by bone marrow stromal cells induce apoptosis and neuroendocrine differentiation in prostate cancer cells. *The Prostate* 71(2):157-167.
14. Li X, Marcondes A, Ragoczy T, Telling A, & Deeg H (2013) Effect of intravenous coadministration of human stroma cell lines on engraftment of long-term repopulating clonal myelodysplastic syndrome cells in immunodeficient mice. *Blood cancer journal* 3(4):e113.

15. Weisberg E, *et al.* (2012) Using combination therapy to override stromal-mediated chemoresistance in mutant FLT3-positive AML: synergism between FLT3 inhibitors, dasatinib/multi-targeted inhibitors and JAK inhibitors. *Leukemia* 26(10):2233-2244.
16. McMillin DW, *et al.* (2010) Tumor cell-specific bioluminescence platform to identify stroma-induced changes to anticancer drug activity. *Nature medicine* 16(4):483-489.
17. Mehta G, Hsiao A, Ingram M, Luker G, & Takayama S (2012) Opportunities and challenges for use of tumor spheroids as models to test drug delivery and efficacy. *J Control Release* May 18 [Epub ahead of print].
18. Torisawa Y-s, *et al.* (2014) Bone marrow–on–a–chip replicates hematopoietic niche physiology in vitro. *Nature Methods*.
19. Villasante A, Marturano-Kruik A, & Vunjak-Novakovic G (2014) Bioengineered human tumor within a bone niche. *Biomaterials*.
20. Marlow R, *et al.* (2013) A novel model of dormancy for bone metastatic breast cancer cells. *Cancer Research* 73(23):6886-6899.
21. Hsiao A, *et al.* (2009) Microfluidic system for formation of PC-3 prostate cancer co-culture spheroids. *Biomaterials* 30(16):3020-3027.
22. Kuperwasser C, *et al.* (2004) Reconstruction of functionally normal and malignant human breast tissues in mice. *Proceedings of the National Academy of Sciences of the United States of America* 101(14):4966-4971.
23. Sakaue-Sawano A, *et al.* (2008) Visualizing Spatiotemporal Dynamics of Multicellular Cell-Cycle Progression *Cell* 132(3):487-498.
24. Smith M, *et al.* (2004) CXCR4 regulates growth of both primary and metastatic breast cancer. *Cancer Res* 64(23):8604-8612.
25. Kwong LN, *et al.* (2012) Oncogenic NRAS signaling differentially regulates survival and proliferation in melanoma. *Nature medicine* 18(10):1503-1510.
26. Castellano E, *et al.* (2013) Requirement for Interaction of PI3-Kinase p110α with RAS in Lung Tumor Maintenance. *Cancer Cell* 24(5):617-630.
27. Ray P, *et al.* (2014) CXCL12-gamma in primary tumors drives breast cancer metastasis. *Oncogene.* 0.(doi):10.1038/onc.2014.1157.
28. Coggins NL, *et al.* (2014) CXCR7 Controls Competition for Recruitment of β-Arrestin 2 in Cells Expressing Both CXCR4 and CXCR7. *PLoS ONE* 9(6):e98328.
29. Cavnar SP, Salomonsson E, Luker KE, Luker GD, & Takayama S (2013) Transfer, Imaging, and Analysis Plate for Facile Handling of 384 Hanging Drop 3D Tissue Spheroids. *Journal of laboratory automation*:2211068213504296.
30. Cavnar S, *et al.* (2014) Microfluidic source-sink model reveals effects of biophysically distinct CXCL12 isoforms in breast cancer chemotaxis. *Integrative Biology*.
31. Korah RM, Sysounthone V, Golowa Y, & Wieder R (2000) Basic fibroblast growth factor confers a less malignant phenotype in MDA-MB-231 human breast cancer cells. *Cancer Research* 60(3):733-740.
32. Mezzanotte L, *et al.* (2011) Sensitive Dual Color In Vivo Bioluminescence Imaging Using a New Red Codon Optimized Firefly Luciferase and a Green Click Beetle Luciferase. *PLoS ONE* 6(4):e19277.
33. Quackenbush J (2002) Microarray data normalization and transformation. *Nature genetics* 32:496-501.

34. Chacon E & Acosta D (1991) Mitochondrial regulation of superoxide by Ca< sup> 2+</sup>: An alternate mechanism for the cardiotoxicity of doxorubicin. *Toxicology and applied pharmacology* 107(1):117-128.
35. Scholl C*, et al.* (2009) Synthetic Lethal Interaction between Oncogenic KRAS Dependency and STK33 Suppression in Human Cancer Cells. *Cell* 137(5):821-834.
36. Choi J*, et al.* (2008) The effect of doxorubicin on MEK-ERK signaling predicts its efficacy in HCC. *J Surg Res.* 150(2):219-226. doi: 210.1016/j.jss.2008.1001.1029. Epub 2008 Mar 1013.
37. McCubrey JA*, et al.* (2007) Roles of the Raf/MEK/ERK pathway in cell growth, malignant transformation and drug resistance. *Biochimica et Biophysica Acta (BBA) - Molecular Cell Research* 1773(8):1263-1284.
38. Jin W*, et al.* (0000) Roles of the PI-3K and MEK pathways in Ras-mediated chemoresistance in breast cancer cells. *Br J Cancer* 89(1):185-191.
39. Roecklein BA & Torok-Storb B (1995) Functionally distinct human marrow stromal cell lines immortalized by transduction with the human papilloma virus E6/E7 genes. *Blood* 85(4):997-1005.
40. Chang Q*, et al.* (2013) The IL-6/JAK/Stat3 feed-forward loop drives tumorigenesis and metastasis. *Neoplasia (New York, NY)* 15(7):848.
41. Eliasson P & Jönsson JI (2010) The hematopoietic stem cell niche: low in oxygen but a nice place to be. *Journal of cellular physiology* 222(1):17-22.
42. Mendelson A & Frenette PS (2014) Hematopoietic stem cell niche maintenance during homeostasis and regeneration. *Nature medicine* 20(8):833-846.
43. Tung Y*, et al.* (2011) High-throughput 3D spheroid culture and drug testing using a 384 hanging drop array. *Analyst* 136(3):473-478.
44. Hsiao AY*, et al.* (2012) 384 hanging drop arrays give excellent Z-factors and allow versatile formation of co-culture spheroids. *Biotechnol Bioeng.* 109(5):1293-1304. doi: 1210.1002/bit.24399. Epub 22011 Dec 24320.
45. Luker K*, et al.* (2012) *In vivo* imaging of ligand receptor binding with *Gaussia* luciferase complementation. *Nat Med* 18(1):172-177.
46. Bardet P-L*, et al.* (2008) A fluorescent reporter of caspase activity for live imaging. *Proceedings of the National Academy of Sciences* 105(37):13901-13905.

Chapter Five: Sensitivity of Quiescent Cancer Cells to Metabolic Perturbations in Bone Marrow Spheroids

5.1 Summary

Metastatic cancer cells harbored in the bone marrow are often quiescent, and as a result, resistant to standard cytotoxic therapies and capable of regrowth even decades after initial disease. The bone marrow regulates quiescence of cancer and stem cells in part via the metabolic microenvironment created by the surrounding stromal cells. Development of strategies to target cancer cells in this microenvironment has been hindered by the lack of experimental models that robustly recreate bone marrow interactions that induce quiescence. Here we further develop a 3D bone marrow spheroid model of cancer quiescence in order to analyze the resulting metabolic microenvironment, its impact on cancer viability, and their sensitivity to therapies. Using optical metabolic imaging, metabolic flux analysis, molecular perturbations of metabolism, and dual-colored bioluminescence of cancer and stromal cell viability, we assessed role of metabolic microenvironments in cancer quiescence. Using this model, we found the bone marrow stromal cell line HS-5, to be basally glycolytic, have minimal metabolic responsiveness, and minimally protect the quiescent cells from metabolic perturbations. Conversely, we found the HS-27A stromal cell line to be metabolically responsive in spheroids, to harbor both oxidative and glycolytic niches of cancer cells, and to robustly protect multiple breast cancer subtypes from metabolic perturbations. This combined approach of spheroid

culture, optical metabolic imaging, and bioluminescence screen provides a platform for identifying strategies to robustly and selectively eliminate quiescent cancer cells in the bone marrow.

5.2 Introduction

Quiescent cancer cells are relatively insensitive to cytotoxic therapies and may contribute to late relapse even decades after initial diagnosis of disease (1-3). Disseminated cancer cells reside in microenvironments that support cancer cell quiescence and confer resistance to chemotherapy, allowing these cells to persist in a viable state after adjuvant treatment (4, 5). In particular, bone marrow is regarded as a major site of quiescent cancer cells. Bone marrow is thought to maintain cellular quiescence of cancer cells in a similar fashion as hematopoietic stem cells, using metabolism, cell contacts, and secreted factors to control distribution (endosteal versus vascular niches) and proliferation of these cells (6-9). One strategy towards eliminating quiescent cancer cells is to selectively target unique metabolic demands of these cells, which is a hallmark feature of cancer that may be exacerbated by hypoxia in bone marrow niches (10). Understanding differences in metabolism between disseminated cancer cells and stroma cells in bone marrow and developing therapies selectively targeting cancer metabolism offer the potential to eliminate quiescent cancer cells and prevent late replaces of disease.

Growing cancer cells often have modified energetic profiles as compared to normal cells (10-13), yet relatively little is known about metabolism of quiescent cancer cells in bone marrow. Cancer cells, hematopoietic stem cells, and other mesenchymal stem cells have commonalities and differences in energetic and biosynthetic demands during growth, quiescence, and in response to hypoxia that may inform potential therapies (14). Similar to

hematopoietic stem cells in hypoxic bone marrow, cancer cells become increasingly dependent on glycolysis via activation of HIFα, which inhibits glucose-derived pyruvate from entering mitochondria (12). Mesenchymal stem cells exhibit metabolic flexibility between oxidative versus glycolytic states; differentiate towards chondrogenic not osteogenic lineages under hypoxia; and are locked in glycolytic or oxidative metabolisms upon differentiation into chondrogenic or osteogenic/adipogenic lineages, respectively (15-18). Within the hypoxic bone marrow environment, hematopoietic stem cells, cancer cells, and mesenchymal stromal cells produce higher levels of molecules that scavenge reactive oxygen species; increase pentose phosphate pathway metabolism; and replace mitochondrial flux with reductive glutamine pathways (4, 14, 17, 19). Despite commonalities in hypoxia-responsiveness among resident bone marrow cells, hypoxia induces cell-type specific differences that may be leveraged to selectively eliminate cancer cells. For example, hematopoietic stem cells decrease mitochondrial mass under hypoxia, decreasing production of reactive oxygen species (20, 21). Conversely, hypoxic cancer cells enlarge their mitochondria, inhibiting apoptosis with a concomitant elevation in reactive oxygen species (22). In response to reactive oxygen species, cancer cells may regain proliferative capacity and/or acquire additional mutagenic stress, but hematopoietic stem cells terminally differentiate and/or undergo apoptosis (21, 23). Leveraging fine balances between responsiveness to reactive oxygen species, energetic demands, and biosynthetic needs may reveal ways to selectively eliminate quiescent cancer cells in heterogeneous bone marrow microenvironments (24).

Recent studies show heterogeneous metabolic microenvironments in bone marrow, which may differently regulate cancer cell quiescence. For example, high metabolic

demands of bone marrow create intravascular hypoxia with additional oxygen depletion proceeding away from the vascular compartment towards endosteal niches (10). Sharply graded hypoxic microenvironments lead to different locations, levels of differentiation, and abundance of hematopoietic, mesenchymal, immune, vascular, and cancer cells (25-27). Although the metabolic status *in vivo* is the summation of all of these interacting components, as a model system we begin by considering the metabolically diverse status of mesenchymal stem cell lineages, particularly the mesenchymal stem cell derived cell lines, HS-5 and HS-27A. HS-5 and HS-27A cells support either expansion or maintenance of hematopoietic stem cells, respectively (28). Multiple studies of these cells describe dichotomous regulation of gene expression, secretion of growth factors, matrix deposition, and support of bone marrow transplant efficiency among other effects on cancer and hematopoietic stem cells (28-32). Additionally, one recent gene expression study revealed that unlike HS-5 cells, HS-27A cells are more pluripotent and express markers of the hematopoietic niche (33, 34). These results suggest HS27A cells also have greater metabolic flexibility between glycolytic and oxidative metabolic states (15). How the metabolic microenvironment supported by these stromal cells and their metabolic coupling with cancer cells supports cancer growth or quiescence is largely unknown.

While prior studies have emphasized interconnected signaling networks in tumor environments (35, 36), recent research reveals that metabolic links among malignant and stromal cells control growth, quiescence, and drug sensitivity of cancer cells (37, 38). Malignant cells promote metabolic reprogramming of stromal cells to supply metabolites, such as lactate and glutamine, necessary to fuel growth of neighboring epithelial cancer cells (39, 40). Cancer and stromal cells may exhibit different responses to molecules such

as glutamine, suggesting the potential to uncouple tumor-stromal metabolism without toxicity to normal cells. To capitalize on cancer metabolism as a target to eliminate disseminated tumor cells from bone marrow, there is an unmet need for cell-based assays that reproduce intracellular interactions in vivo while enabling facile analyses of metabolic states and drug efficacy.

Here we investigate how the metabolic status of 3D cancer-stromal spheroids determines growth and drug sensitivity of multiple breast cancer cell lines. We use optical imaging of endogenous NADH as a label-free method for determining metabolic gradients within 3D culture environments. We also use extracellular flux measurements, molecular inhibition of metabolic pathways, and bioluminescence-based quantification of viability of cancer and stromal cells to assess the collective metabolic environment of our model system. We found that metabolic differences in bone marrow stromal cells differently support quiescence of multiple cancer cells, interdependence on glucose and glutamine, and sensitivity to molecular inhibition of metabolic pathways. Specifically we found HS-5 stromal cells to be glycolytic, induce quiescence of multiple breast cancer subtypes (including aggressive, triple negative MDA-MB-231 cells), and provide limited support to cancer cells upon metabolic perturbations. We also found HS-27A stromal cells to be more metabolically flexible, supporting cancer cell resistance to nutrient withdrawal. Together these data can be used to screen for therapies that target the metabolic phenotypes of quiescent cancer cells in bone marrow and eliminate their contribution to late relapse.

5.3 Material and Methods

5.3.1 Reagents

Unless otherwise stated we purchased all cell culture reagents from Life Technologies (Carlsbad, CA, USA). We obtained drugs and compounds from the following sources: PD0325901 from SelleckChem (Houston, TX, USA); D-glucose, 2-deoxy-D-glucose, rotenone, and sodium dichloroacetate from Sigma Aldrich (St. Louis, MO, USA); and oligomycin from Seahorse Biosciences (Massachusetts, USA). We prepared a rotenone stock at 10 mM in ethanol. We prepared all other compounds in formulations supplied or specified by manufacturers.

5.3.2 Cell culture and spheroid assays

We grew HS-5, HS-27A, MDA-MB-231, MDA-MB-468, and T47D cells as we described previously (41). Briefly, we maintained all cells in 10% FBS (HyClone, ThermoScientific, Waltham, MA, USA) DMEM (#11995, Life Technologies) supplemented with penicillin, streptomycin, and glutamine (Life Technologies). Cells were maintained at subconfluence and passaged every 2 to 4 days. Stromal and cancer cells express Click Beetle Red and Green, respectively. Cancer cells also expressed fluorescent ubiquitin-based cell cycle indicator (42).

We detailed our spheroid assays previously (41). Briefly, $3x10^3$ cells were distributed as a suspension in 25 µl per well to black 384 shallow, round bottom well plates (Corning Incorporated #3676, Corning, NY, USA). For cancer cell growth and dose-response assays we composed the spheroids of 1% MDA-MB-231 with the balance of stromal cells. For experiments looking at the distribution of cancer cells throughout

spheroids we seeded $3.3x10^3$ total cells with the additional 10% MDA-MB-231 cells. For optical metabolic imaging in different sized spheroids we seeded 300, 1000, and 3000 mesenchymal stem cells. For comparison of metabolic gradients in different stromal cell types we seeded spheroids with $3x10^3$ HS-5, HS-27A, and MSCs. For optical metabolic imaging in 2D, we seeded 10^6 HS-5, HS-27A, or primary mesenchymal stem cells in a 35 mm dishes in spheroid media, but containing 10% FBS. Once cells were firmly adhered we replaced medium with that used for spheroids.

The culture conditions of all spheroids were consistent unless otherwise stated. We seeded and maintained all spheroids in phenol red free DMEM (#31053, Life Technologies), supplemented with 1% FBS (HyClone, ThermoScientific, Waltham, MA, USA), penicillin/streptomycin/glutamine (Life Technologies), and pyruvate (Life Technologies). For experiments modulating the glucose and glutamine levels, the base medium was replaced with glucose- and glutamine-free DMEM, supplemented with glutamine-free penicillin/streptomycin (Life Technologies), and pyruvate. We then supplemented D-glucose (Sigma Aldrich, St. Louis, MO, USA) and glutamine (Life Technologies) at listed concentrations. We exchanged about 80% of the volume of media every second day for the entirety of each assay.

The timing of each assay was consistent unless otherwise stated. For growth assays, we measured bioluminescence flux at two and ten days, change media with fresh spheroid media every two days. For dose-response curves, after cells spheroids formed for two days, we initialized treatment by exchanging media on the second day and every two thereafter for a total assay time of ten days. For optical metabolic imaging in 2D and

spheroids and for microscopy of cancer cell distribution, we imaged spheroids 24 hours after seeding.

5.3.3 Bioluminescence imaging

We previously described Click Beetle Green and Red imaging in detail (41).

5.3.4 Microscopy

For microscopy of 2D and 3D cultures we used an Olympus MPE using a 25X NIR corrected objective (XLPLN25XWMP, NA=1.05, Olympus, Tokyo, Japan). We facilitated stable imaging of spheroids by transferring spheroids to a custom spheroid imaging plate that we described previously (43). To image the fluorescence ubiquitin-based cell cycle indicator, we excited both AcGFP and mKO fluorophores with 920nm excitation and collected green (495-540nm) and red (575-630nm) channels with their respective band-pass filters.

5.3.5 Intensity-based metabolic imaging

For intensity-based optical metabolic imaging we used two paired excitation and emission wavelengths for NADH and FAD imaging similar to previous descriptions (44). For NADH intensities, we excited with 740 nm and collected light with a band-pass filter (420-460nm). For FAD intensities, we excited with 890 nm and collected light with a band-pass filter (495-540nm). We maintained constant imaging parameters within each experimental run, including laser power, detector voltage, and offset. To quantify image intensities and ratios, we exported pixel-by-pixel intensities from Fluoview (Olympus, Tokyo, Japan) into Microsoft Excel (Seattle, WA, USA), where we removed below background pixels (determined from cell-free regions) and performed additional

calculations. We also used Excel to determine frequency distributions and NADH to FAD ratios.

5.3.6 Frequency domain fluorescence imaging and data analysis

For lifetime-based measure of metabolic status, we used the ISS FastFLIM system, containing a Spartan 6 processor, and coupled with our Olympus MPE microscope. We calibrated the FLIM system to a fluorescein dye slide, using open filters and 740 nm excitation and an expected single component lifetime of about 4.1 ns. Using an excitation of 740 nm with mode-locked 80MHz Ti:Sapphire laser system (Spectra-Physics Mai Tai) and a 690 dichroic to block internal reflectance from the IR laser, we collected NADH emission using a X dichroic and Y band-pass filters. We also measured FAD lifetime simultaneously using the long-pass dichroic cut and Y nm band-pass filter. The caveat with the FAD measurement with 740nm excitation is that there is a small spectral overlap with NADH (45). Using excitation of 890 eliminates NADH excitation but would require recalibration of the FLIM system with each laser wavelength change. We used a 256x256 view field and 100μs dwell time for all frequency-domain images. We captured between 15 and 25 frames and adjusted laser intensity in order to maximize pixels above our count threshold. To image size-based gradients in spheroids, we used smaller view fields for smaller spheroids in order to maximize the view area occupied by the spheroid.

To analyze the lifetime data, we exported the phase lifetime and counts from the VistaVision software into Excel. In Excel we removed lifetime and count values that fell outside 0.5-5 ns for phase lifetime and below 5 for counts. We then applied a count-weighted average for imaging segments as described in Figure S3. For images of stromal cells cultured in 2D, we used the count-weighted average for the entire frame. For

spheroids, we used radial cuts in four directions for each spheroid consisting of 1x50 pixel vectors that progressed from exterior to interior of each spheroid. Aligning the spheroid edge for each of four radial cross-sections for four spheroids from two independent setups, we used average the lifetime across the radius profile.

5.3.7 Glucose measurements

To measure bulk glucose from cell culture supernatants we used commercial blood glucose meter Accu-chek Aviva Plus (Roche Diagnostics). Samples were diluted 50% in PBS containing 20 wt% Probumin (EMD Millipore, Billerica, MA, USA) in order to bypass blood quality errors. All values were benchmarked against high glucose measurements in spheroid culture medium (25mM, 450 mg/dl). We measured supernatants pooled from 4 spheroid wells, from 20 separate spheroids, totaling N = 5 measurements for each stromal combination.

5.3.8 Extracellular Flux Assays

We performed extracellular flux assays using a Seahorse Bioscience (Massachusetts, USA) XF^e96 Extracellular Flux Analyzer. We performed the XF Glycolysis Stress test per manufacturer specifications. We seeded cells overnight at a density of $15x10^3$ cells per well. Injections were performed sequentially with 25mM D-glucose, 1μM oligomycin, and 100 mM 2-deoxy-D-glucose. For pretreatment with PD0325901, we treated cells with 10 nM overnight and during the 1-hour incubation in unbuffered assay medium. Data are plotted for average of N = 6 wells over three measurement cycles.

5.3.9 Statistical analysis and plotting

We processed bioluminescence and optical metabolic data in Microsoft Excel (Seattle, WA, USA) before plotting data using GraphPad Prism (San Diego, CA, USA). All graphs display mean values ± standard error of the mean (S.E.M.) unless stated otherwise. We propagated error for all data normalized to experimental measurements.

We described our strategy for measuring selective elimination of cancer cells but not stromal cells using dual-colored Click Beetle luciferase previously (41). For growth curves we divided average bioluminescence flux for red and green signals at day 10 by their corresponding value at day 2. For dose-response curves, we divide background subtracted flux values by their corresponding untreated condition for both green and red signals. To visualize the selectivity of cancer cell elimination, we plotted the log-2 ratio of the red signal divided by the red signal and subtract the value of the untreated control. Selectivity for the untreated control is zero and positive selectivity corresponds to relatively lower cancer (green) as compared to stromal (red) signals.

5.4 Results

5.4.1 Bone marrow stromal spheroids support growth or quiescence of breast cancer cells

We used long-term co-cultures of bone marrow stromal cell lines (HS-5 and HS-27A) to recreate metastatic growth or quiescence in bone marrow (41). To investigate relative effects of HS5 and HS27A stromal cells on quiescence or growth of triple negative ($ER^-/PR^-/Her2^-$) MDA-MB-231 cells, we varied the composition of the stromal environment and independently monitored growth of cancer and stromal cells with stably expressed Click Beetle Green and Red luciferases, respectively. Increasing the fraction of HS27A

compared to HS5 cells while maintaining total cell number, we determined that relatively few HS5 cells (EC_{50} ~27%) diminished growth of MDA-MB-231 cells (Fig. 5.1A). HS-27A cells supported rapid growth of cancer cells as compared with the quiescence-supporting HS-5 cells, similar to our previous report (41). MDA-MB-231 co-cultures with untransformed primary human mesenchymal stem cells (MSC) grew rapidly as compared to HS-5 cells, which suggests HS-27A cells represent the subtype of mesenchymal stromal cells that typically is enriched through *in vitro* isolation (data not shown).

Despite quiescence of cancer and stromal cells in the HS-5 spheroid environment, we observed substantial acidification of their supernatant as compared to HS-27A cells based on phenol red in culture medium. To measure whether lactate-based acidification corresponded to decreased glucose levels in HS-5 spheroids, we measured glucose levels in medium after 2 days of culture. Corresponding with the decreased pH in the HS-5 cultures, these cells reduced glucose in the bulk media by ~20% relative to ~10% for HS-27A (Fig. 5.1B). Although this is a relatively small decrement considering the typical non-physiologically high glucose culture medium (25mM) as compared to *in vivo* (5mM), we expect that local, cell-scale depletion of glucose for cancer cells within HS-5 spheroids may surpass 20% depletion. To confirm differences between glucose consumption between these cell types, we used the Seahorse extracellular flux analyzer (XF^e96) to compare levels of oxygen consumption and extracellular acidification. Under conditions of glutamine only, or sequential glucose and oligomycin (inhibition of oxidative metabolism) injections, we found HS5 cells to have both higher oxygen consumption and lactate production (Fig. 5.1B, i to ii glucose injection, ii to iii oligomycin injection). HS5 and HS27A cells were both

relatively unaffected by inhibition of oxidative metabolism by oligomycin, as shown by the relatively small shift between Fig. 1Bii-iii.

On a per cell basis these results suggest that glucose consumption is different between stromal cells and between 2D and 3D cultures. To test this, we estimated the glucose consumption from two different analysis modalities, both Seahorse extracellular flux analyzer and direct glucose measurements. From Seahorse data (Fig. 5.1Bii), assuming that two lactate protons are derived from a single glucose molecule (an imperfect but reasonable estimate), we calculated glucose consumption rates of about 3.1 and 2.5 fmol/minute/cell for HS-5 and HS-27A in 2D culture, respectively, after normalizing to $15x10^3$ cells per well. Assuming constant per cell glucose consumption, the glucose consumption rates are 14.5 and 7.2 fmol/minute/cell for HS-5 and HS-27A in 3D spheroids, respectively, after normalizing to $3x10^3$ cells per spheroid. These estimates suggest that on a per cell basis, cells are more glycolytic in 3D cultures, which is consistent with other reports comparing 2D and 3D cultures (46).

5.4.2 Optical metabolic imaging to study metabolic microenvironment

To confirm the glucose consumption of the bone marrow stromal cells, we used optical metabolic imaging to capture intensities and redox ratio of endogenous NADH and FAD. There was a rank-order increase in NADH intensities (MSC < HS-27A < HS-5) and reverse-order increase in FAD, intensities (Fig. 5.1C-D). Likewise, the background adjusted pixel-by-pixel ratio of NADH to FAD showed a similar rank-order increase in redox ratio for MSC, HS-27A, and HS-5 cells grown in 2D (Fig. 5.2E). Based on a previous report linking redox ratio to glycolytic index (glucose consumption per lactate production), these data suggest that HS5 are more glycolytic than HS27A cells and MSCs (44). Despite improved

optics of two-photon microscopy, intensity-based measures of fluorescence are complicated at depth within 3D tissues because of preferential absoption of blue (NADH) versus green (FAD) light. Therefore, we also used frequency domain fluorescence lifetime imaging to measure changes in free and bound NADH for theses stromal cell types (Fig. 5.2F). Increased glycolysis has been associated with increased fraction of free, protein unbound NADH and corresponds to a decreased fluorescence lifetime (44, 47). The phase lifetime differences of NADH did not follow the same intensity-based order for HS5, HS27A, and MSCs. Instead, MSCs presented the lowest NADH phase lifetime, followed by HS5 and HS27A.

To assess the impact of stromal cell type on the metabolic microenvironment of 3D spheroids, we measured the intensity-independent lifetime profile of NADH across the diameter of different cell type and size spheroids. Two factors determine the metabolic status of these spheroids: the exterior NADH lifetime and the slope of the NADH lifetime over the first 60 μm of the spheroid. The former reflects the non-nutrient limited condition and the latter measures the responsiveness of stromal cell types to radial nutrient density and distance to the center of the spheroid. To measure radial lifetime profiles, we used four radial sections of multiple spheroids and a count-weighted average of above-threshold pixels to calculate average lifetime for radial positions (Supplemental Fig. D.1). As proof of concept for this approach, we show the size of MSC spheroids dictated the slope of the NADH lifetime gradient but not the exterior starting value (Fig. 5.2). Small spheroids showed limited slope of change in NADH lifetime from exterior to interior, and we observed a rank-order increase in slope with increasing size of spheroid (Fig. 5.2B-C). Lifetime did not change through depth of small non-nutrient limited spheroids

(Supplemental Fig. D.2). Previous reports describe hypoxia and/or anoxia at around 100 μm from blood vessels *in vivo* rat mesentery (48), 100-150 μm in tumor sections (49), and beyond several cell-diameters *in silico* bone marrow models (50). Although it is difficult to decouple oxygen and other metabolic gradients from NADH lifetime profiles, our data suggest sensing of metabolic changes at distances smaller than described for hypoxia.

Comparing among large spheroids of different stromal cell types, we found the non-nutrient limited exterior condition reflects the NADH phase lifetimes measured in 2D cultures, with MSCs having the lowest exterior lifetime, followed by HS-5, and HS-27A cells (Fig. 5.3A-B). This result suggests that the exterior of these spheroids have similar metabolic status as 2D cultures with no metabolic limitations. HS-5 spheroids produced the lowest slope of NADH lifetime at 0.00283 ns/μm (95% CI: 0.0025-0.0032), followed by MSC at 0.0039 ns/μm (95% CI: 0.0034-0.0044), and HS-27A at 0.0041 ns/μm (95% CI: 0.0038-0.0046). High slopes reflect flexibility between oxidative and glycolytic metabolism.These data reflect that HS-5 spheroids are the least responsive to radial nutrient gradients, followed by MSCs and HS-27A cells both having similar high levels of responsiveness.

To establish how MDA-MB-231 cells distribute in spheroids with different metabolic profiles, we imaged locations of these breast cancer cells 24 hours after forming spheroids. MDA-MB-231 cells distributed solely on the exterior of the more glycolytic, less metabolically responsive HS-5 spheroids. By comparison, we identified MDA-MB-231 cells both in the interior and exterior of spheroids with the more metabolically responsive HS-27A cells (Fig. 5.3C-D). Since spheroids are seeded with a homogenous mix of stromal and cancer cells, the interior-exterior distribution must be an active migratory process by the

cancer and/or stromal cells. These localization differences persist at longer time points. Over time the exterior cancer cells in HS-27A spheroids grow substantially, whereas the interior MDA-MB-231 cells do not (Fig. 5.3C-D).

5.4.3 Metabolic balance between glycolysis and glutaminolysis for cancer-stromal co-culture

Increased glycolysis by HS-5 depletes bulk glucose levels by about 20%, which we expect limits the local concentration available to the cancer cells. With depleted glucose, we expect cancer cells to be increasingly dependent on other sources of carbon, i.e. lactate, glutamine, amino acids, or fatty acids. Here we tested the interdependence of three breast cancer subtypes (MDA-MB-231, MDA-MD-468, and T47D) on combinations of glucose and glutamine when cultured with more metabolically responsive HS-27A or unresponsive HS-5 stromal cells (Fig. 5.4). After 2 days formation in full spheroid media and 8 days of culture in various glucose and glutamine concentrations, we plotted the fold change for cancer cell bioluminescence as compared to the high glucose and high glutamine condition, color-coded for the log-2 based ratio of cancer to stromal signals (Fig. 5.4). Corresponding surface plots for stromal components with the same color-coding are found in the Supplemental Information (Fig. D.3).

Comparing between breast cancer subtypes and their culture in the two stromal environments, each had a unique response to combinations of glucose and glutamine. MDA-MB-231 cells are very responsive to both glucose and glutamine in both HS-5 and HS-27A co-cultures (Fig. 5.4A-B). Conversely, their counterpart stromal cells were insensitive to glutamine but highly sensitive to glucose for HS-5, and largely insensitive to both glucose and glutamine for HS-27A. These data correspond with our NADH lifetime profiles suggesting that HS-5 stromal cells are highly glycolytic, but HS-27A cells are more flexibly

glycolytic. Warmer color-coding for low glutamine and high glucose conditions highlights the selective response of MDA-MB-231 cells towards glutamine depletion in HS-5 co-cultures. The stromal cells' glucose-glutamine response surface profile was independent of counterpart cancer cells (Fig. D.3), suggesting the larger fraction of stromal cells in each spheroid dominates their response. MDA-MB-468 followed closely after response of MDA-MB-231 cells in HS-5 co-cultures (Fig. 5.4C), showing higher sensitivity to both glucose and glutamine, which is reflected by warmer color-coding. In HS-27A co-cultures MDA-MB-468 cells were refractory to changes in glucose and glutamine, suggesting a metabolically protective environment (Fig. 5.4D). T47D cells showed no sensitivity to glutamine but extremely high sensitivity to glucose withdrawal in HS-5 co-cultures (Fig. 5.4E), which may reflect dependence on glycolysis that is associated with ER^+ dependent signaling (44). In HS-27A co-cultures, T47D were moderately responsive to glucose and glutamine withdrawal. These data are summarized in Table 5.1, which captures the qualitative responsiveness of these breast cancer subtypes at the four glucose-glutamine extremes of each surface plot. Recreating pharmacologic sensing of glutamine and/or glucose deprivation may provide an avenue for selectively eliminating some subsets of breast cancer metastases. Additionally, these results suggest that independence of T47D to glutamine withdrawal and MDA-MB-468 cells independence of glucose and glutamine, may suggest resistant phenotypes that contribute to late bone metastasis relapse.

5.4.4 Metabolic inhibition selectively eliminates cancer cells

Using known inhibitors of glycolysis we tested whether we could selectively eliminate growing and quiescent cancer cells by inhibiting differential metabolic profiles. Using 2-deoxy-glucose, which inhibits the first enzyme in glycolysis we confirmed that HS-5

cells are more dependent on glycolysis than HS-27A and MDA-MB-231 cells (Fig. 5.5A-B). Dose-response curves for 2-deoxy-glucose closely match the differential effects on cancer and stromal cells produced by glucose deprivation (Supplemental Fig. D.4). As compared to HS-5 cells, HS-27A and MDA-MB-231 cells grown with either stromal spheroids are similarly less sensitive to both 2-deoxy-glucose and glucose deprivation. Using dichloroacetate, which inhibits pyruvate dehydrogenase kinase and forces pyruvate away from lactate production into mitochondria, we selectively eliminated cancer cells in both their quiescent and growing states in both HS-5 and HS-27A spheroids (Fig. 5.5C-D).

We also tested known inhibitors of oxidative metabolism via electron transport decoupling and inhibition of oxidative metabolism. As predicted by minimal responsiveness of HS-5 and HS-27A to oligomycin in Seahorse assays, inhibition of Complexed I and V with rotenone and oligomycin, respectively, had minimal effect on stromal cells (Fig. 5.5C-D). MDA-MB-231 cells were selectively eliminated in both HS-5 and HS-27A spheroids, suggesting the role of oxidative metabolism role in both quiescent and growing situations. Inhibition of oxidative metabolism was most effective in the growth supporting HS-27A microenvironment and less positively selective in HS-5 spheroids. Although positively selective for both, eliminating cancer cells via inhibition of oxidative metabolism was incomplete, with 10-20% and 30-50% CBGreen signal remaining at maximal levels of rotenone and oligomycin, for HS-27A and HS-5 co-cultures, respectively. The incomplete response to inhibition of oxidative metabolism and the cancer cell location within HS-27A spheroids (Fig. 5.3D) suggests there is a reservoir of glycolytic cancer cells housed in the center of the HS-27A spheroid. Therefore, molecular intervention that suppressed both oxidative and glycolytic metabolism may better eliminate cancer cells in

both metabolic states. Co-inhibition of glycolysis and oxidative metabolism was a successful strategy in reversing lupus by deactivating $CD4^+$ T cells (51).

Contact-inhibition induced quiescence of stromal fibroblasts has previously been coupled with maintenance of glycolytic throughput, shuttling glucose into the pentose phosphate shunt, and backward flux of glutamine into the TCA cycle (52). To test whether flexible metabolism of HS-27A and their support of MDA-MB-231 cell growth is dependent on the pentose phosphate pathway, we measured their dose response to the steroid hormone, dehydroepiandrosterone (DHEA) (Fig. 5.5E). Interestingly, the cancer cells were eliminated with positive selectively in both HS-5 and HS-27A spheroids, suggesting the involvement of the pentose phosphate pathway for these cancer cells in both stromal environments. The IC_{50} was reduced for both stromal and cancer cells in HS-27A as compared to HS-5 co-cultures. These data suggest that unlike HS-5, HS-27A produce compensatory shift towards the pentose phosphate pathway within spheroids.

We previously suggested that selective elimination of quiescent and growing MDA-MB-231 cells by inhibition of constitutively active KRas (MEK inhibitor, PD0325901) could be attributed to non-proliferation-based mechanisms (41) (Fig. 5.5F). To test the metabolic effects of MEK inhibition, we pretreated MDA-MB-231 cells overnight prior to measuring extracellular flux in the Seahorse system (Fig. 5.6). Metabolic activity was suppressed for glutaminolysis, glycolysis, and maximal glycolytic capacity. These data further suggest that MEK inhibition functions in part through a non-cell cycle-based mechanism and suppresses both glycolytic and oxidative metabolism.

5.5 Discussion and Future Goals

Elimination of cancer cells with non-cytotoxic therapies has two-fold benefit. Firstly, targeting non-cytotoxic can limit toxicity to other high turnover cells such as hematopoietic cells, bone marrow, mucosal membranes, etc. Secondly and our major focus here, targeting non-cytotoxic phenotypes offers means to eliminate quiescent cancer cells that are refractory to standard chemotherapies therapies and contribute to relapse. Here we build upon our previous co-culture model of bone marrow metastases in order to analyze metabolic phenotypes in quiescent and growing cancer cells. Using this system we identify the glycolytic HS-5 spheroids promote cancer cell quiescence and the basally less metabolically active, but more responsive HS-27A spheroids promote cancer growth. Using our complementary strategies to measure and perturb metabolic status of growing and quiescent cells may provide a platform to screen therapies that limit quiescent cancer relapse.

Despite derivation from the same mesenchymal stem cell population and corresponding with previous results (34), our results reveal that HS-5 and HS-27A cells represent two metabolically distinct stromal populations. Our measured redox ratios, extracellular flux analysis, glucose consumption, basal NADH phase lifetimes, and radial NADH phase lifetime gradients describe HS-5 cells as more glycolytic and less metabolically responsive than HS-27A cells. These results, previous results of HS-27A cells expressing a marker of multi-potency and of the hematopoietic niche (34), and description of metabolically flexible mesenchymal stem cells (15), suggests that HS-27A are less differentiated and more common to the hematopoietic niche *in vivo* than HS-5 cells. Furthermore, our results suggest that HS-5 spheroids contain a larger reservoir of

glycolytic cancer cells resistant to inhibition of oxidative metabolism as compared to HS-27A co-cultures. These data, the cancer cell location data, and the minimal NADH lifetime responsiveness suggests that HS-5 co-cultures may model rigid hypoxic-like, glycolytic phenotypes as compared to the metabolically responsive HS-27A spheroids. Conversely in HS-27A spheroids, cancer sensitivity to inhibition of oxidative metabolism, glycolysis, and the pentose phosphate pathway, taken with cancer cell distribution on NADH lifetime profile, all suggest these stromal cells to be more metabolically responsive.

While it is difficult to assign cause-effect with these outcomes, it is clear that the more metabolically responsive HS-27A spheroids provide protection from glucose-glutamine withdrawal for three breast cancer sub-populations (MDA-MB-231, MDA-MB-468, and T47D). Using this strategy, we reveal unique metabolic profiles for three breast cancer sub-populations. Triple negative ($ER^-/PR^-/Her2^-$) MDA-MB-231 cells were dependent on both glucose and glutamine in both stromal cell types, which may reflect a previous report of decoupled dependence of K-Ras transformed cells on both glucose and glutamine (53). In this work they describe that K-Ras transformed cells such as MDA-MB-231 cells, rely on glycolysis for ATP and glutamine for anaplerosis. Additionally, we found inhibition of MEK within MDA-MB-231 cells suppressed both oxidative metabolism and glycolysis resulting in selective cancer cell elimination in both spheroid environments. For these cancer cells, mimicking combined oxidative and glycolytic inhibition may provide a strategy for eliminating metastases similar to normalization of metabolism to reverse symptoms of lupus (51). Similarly, triple negative ($ER^-/PR^-/Her2^-$) MDA-MB-468 cells showed high sensitivity to glucose and glutamine in HS-5, but nearly undetectable response in HS-27A co-cultures, suggesting a supportive environment created by HS-27A cells. Such

resistance to metabolic perturbations may indicate signaling via over expressed EGFR on MDA-MB-468. The ER^+ T47D cell line showed extreme sensitivity towards glucose deprivation, which may confirm previous reports of glycolysis with increased receptor status (44).

These findings, although decoupled from cell-specific mechanisms, provide a platform to measure and perturb the metabolic status and outcomes of cancer cells housed within metabolically difference bone marrow stromal cells. To better define mechanisms for each of these cancer cell lines we propose measuring cell cycle status, NADH lifetime, and drug-dependent outcomes for the cancer cells in each stromal environment. Using these strategies to screen and develop compounds that target cancer cells' metabolism may provide alternatives to cytotoxic therapies that would better eliminate quiescent cancer cells in bone marrow.

5.6 Figures

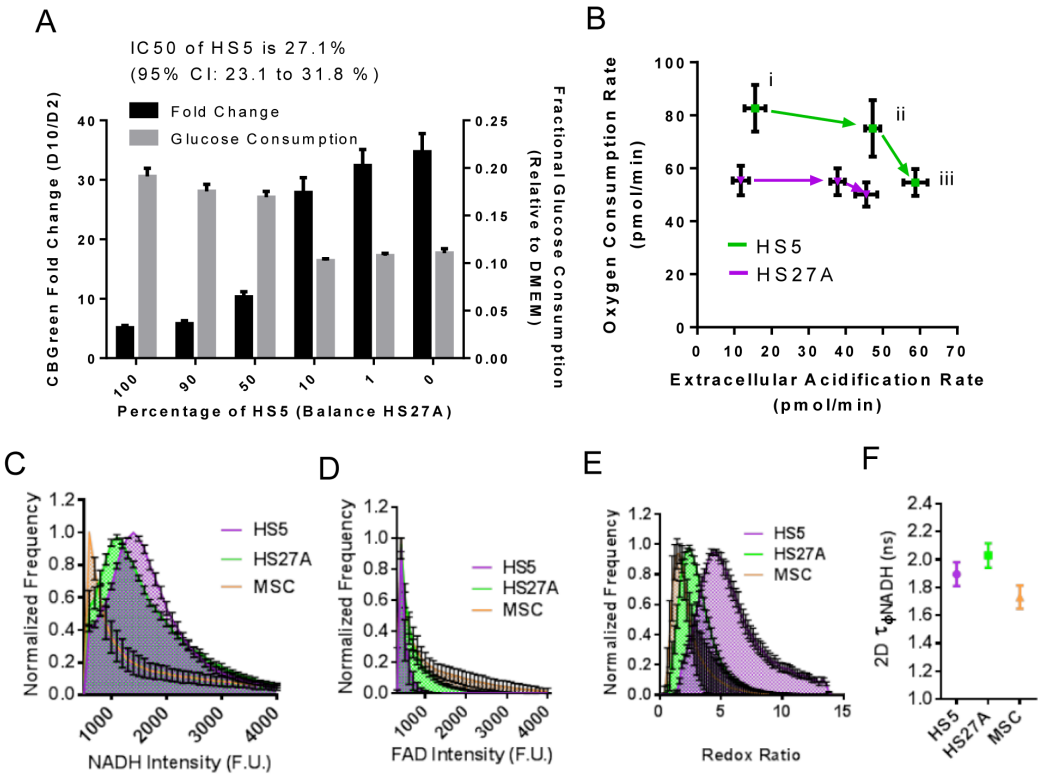

Figure 5.1. HS-5 and HS-27A bone marrow spheroids support different levels of glucose consumption and growth of MDA-MB-231 cells. (A) Increasing proportion of HS-5 relative to HS-27A stromal cells decrease the relative growth of MDA-MB-231 cells. We measured growth by bioluminescent flux fold change from day 2 to day 10 and plotted it on the left axis (black bars). Fold change values are reported as mean + S.E.M. for N = 28 spheroids for each condition from one of three representative experiments. In a separate experiment without cancer cells but similar proportions of HS-5 and HS-27A, we found glucose consumption to increase with larger proportion of HS-5 cells. We plotted the glucose consumption on the right axis (Gray bars) as percentage of 25mM glucose in base media. Glucose values are reported as mean + S.E.M. for 5 measurements with a commercial glucose meter for supernatants pooled from 4 spheroids (20 spheroids total) from two independent setups. (B) For both HS-5 (green) and HS-27A (purple) stromal cells we plotted the oxygen consumption rate and extracellular acidification rate for sequential baseline (i) glutamine conditions, (ii) after injection of 25mM glucose, or (ii) after injection of 1μM oligomycin in the XF^{e}96 Seahorse Biosciences assay. Averages are pooled for N=6 wells over three consecutive mixing-measurement cycles. Assays were seeded overnight with 15x10^{3} stromal cells per well. We incubated for 1 hour prior to measurement in un-buffered media containing essential amino acids and glutamine, per manufacture recommendation for the XF Glycolysis Stress Test. Frequency distributions of (C) NADH, (D) FAD, and (E) NADH:FAD ratio for HS-5, HS-27A, and primary mesenchymal stem cells (MSCs). For each intensity- or ratio-level (x-axes) of the frequency distribution, the maximum-normalized values are plotted as the mean ± S.E.M. for four images, from one of three representative setups. Redox ratios are calculated in a pixel-by-pixel manner from four pictures from one of three representative setups. Intensity-based NADH images were captured with a 740 nm excitation and 420-460nm emission filter and FAD is captured with 890 nm excitation and 495-540 nm emission filter. (F) NADH phase lifetime plotted as mean ± S.E.M. for each of the same three stromal cell types from N = 10 measurements, from three independent setups. We pooled lifetime-based data due to our ability to calibrate lifetime measurements between trials. Lifetime-based measurements were captured with a 740 nm excitation and filtered with 435 (40) nm and 530 (11) nm band-pass filters for NADH.

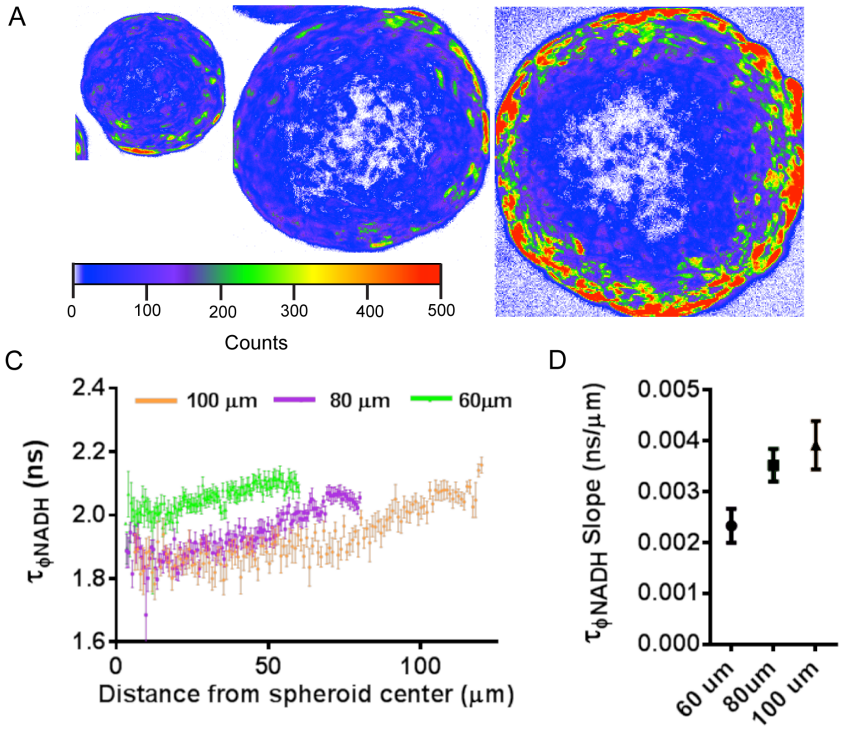

Figure 5.2. Lifetime-based optical metabolic imaging reveals NADH lifetime gradients in different size mesenchymal stem cell spheroids. (A) For MSC spheroids, increasing diameter from 120µm, to 160µm and 200 µm diameter changed the NADH phase lifetime profile (B). (A) Images of spheroids are depiction of the number of photon counts acquired across spheroids. Note that larger spheroids required longer acquisition time to provide above-background counts on the interior of the spheroid, hence the high counts on the exterior. Increasing spheroid size corresponded with increasing NADH lifetime slope (C), which we attribute to decreasing nutrient concentrations for larger spheroids. See Supplemental Figure D.1 for details of quantification. NADH phase lifetime profiles are averaged for four radial cross-sections on four spheroids for each size spheroid.

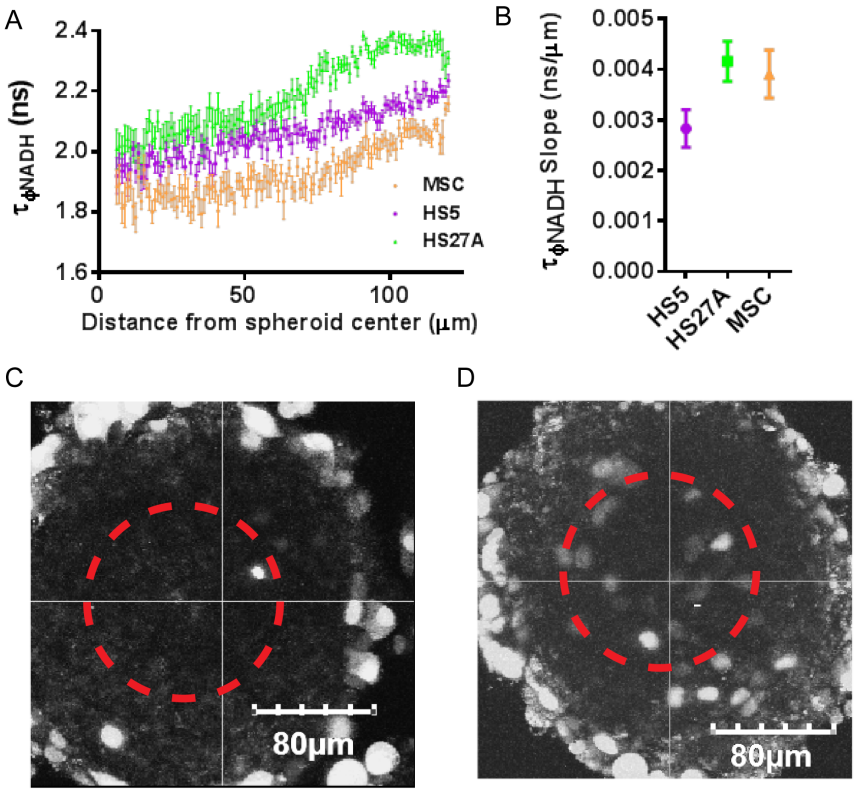

Figure 5.3. Bone marrow stromal cell type produce different 3D metabolic gradients in spheroids. (A) Similar to Figure 5.2, NADH fluorescence lifetime profiles reveal rank-order decrease of lifetime for the exterior of spheroids similar to in 2D cultures (Fig. 5.1F), with HS-27A the highest, followed by HS-5 and MSCs. (B) The slope of the NADH phase lifetime measured by linear regression over the first 60 µm was highest for MSCs, closely followed by HS-27A, and the lowest with HS-5. NADH phase lifetime profiles are averaged for four radial cross-sections on four spheroids for each size. Fluorescence imaging of cancer cells showed localization to the exterior of (C) HS-5 spheroids but to interior and exterior of (D) HS-27A spheroids. These locations were also maintained at longer time points.

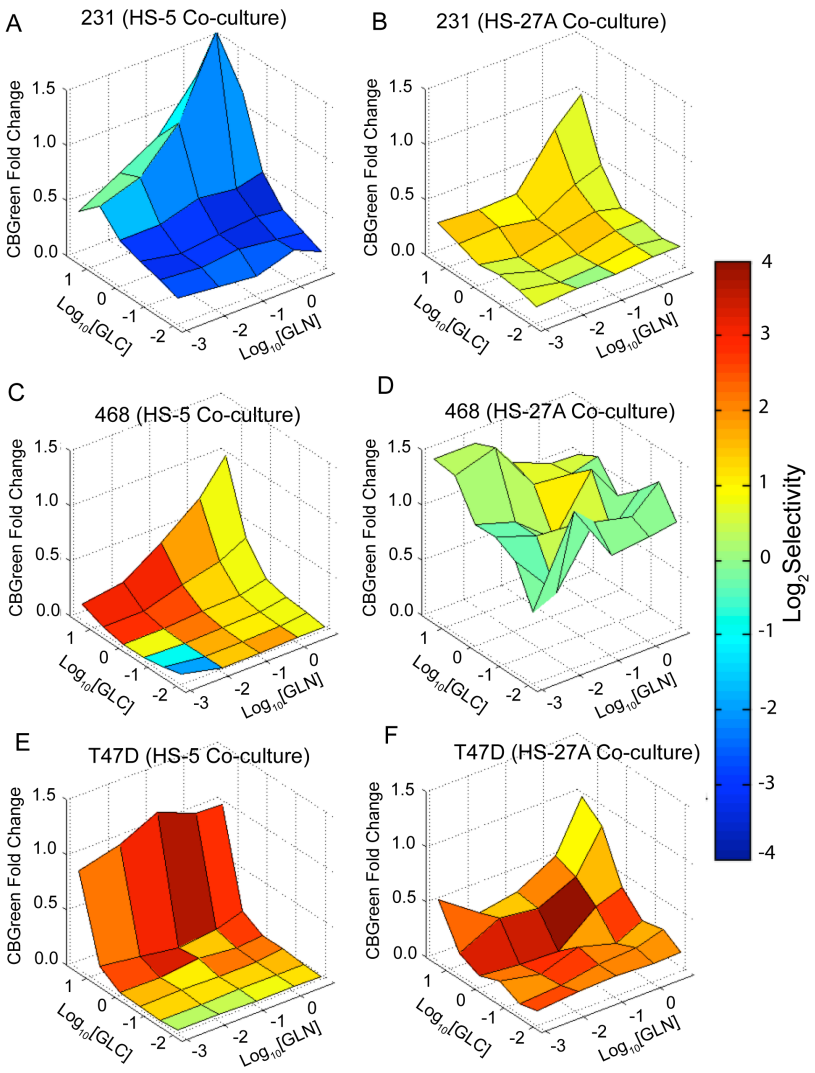

Figure 5.4. Interdependence on glucose and glutamine for cancer and stromal cells in bone marrow spheroids. We plotted combination dose-response surface plots of glucose and glutamine concentrations for CBGreen signal from (A-B) MDA-MB-231, (C-D) MDA-MB-468, and (E-F) T47D cells grown in (A, C, E) HS-5 or (B, D, F) HS-27A spheroids. We also plotted the corresponding CBRed stromal signal for HS-5 and HS-27A cells in Supplemental Figure D.3. We plotted the CBGreen fold change as compared to the high glucose and high glutamine concentration for both cancer and stromal cells. The plots are color-coded for log-2-scaled ratio of CBRed to CBGreen signal, both normalized to high glucose and high glutamine. Hot colors designate relatively lower cancer signal. In the dose-response surfaces, values are plotted as mean for 4 spheroids from one of two representative independent trials.

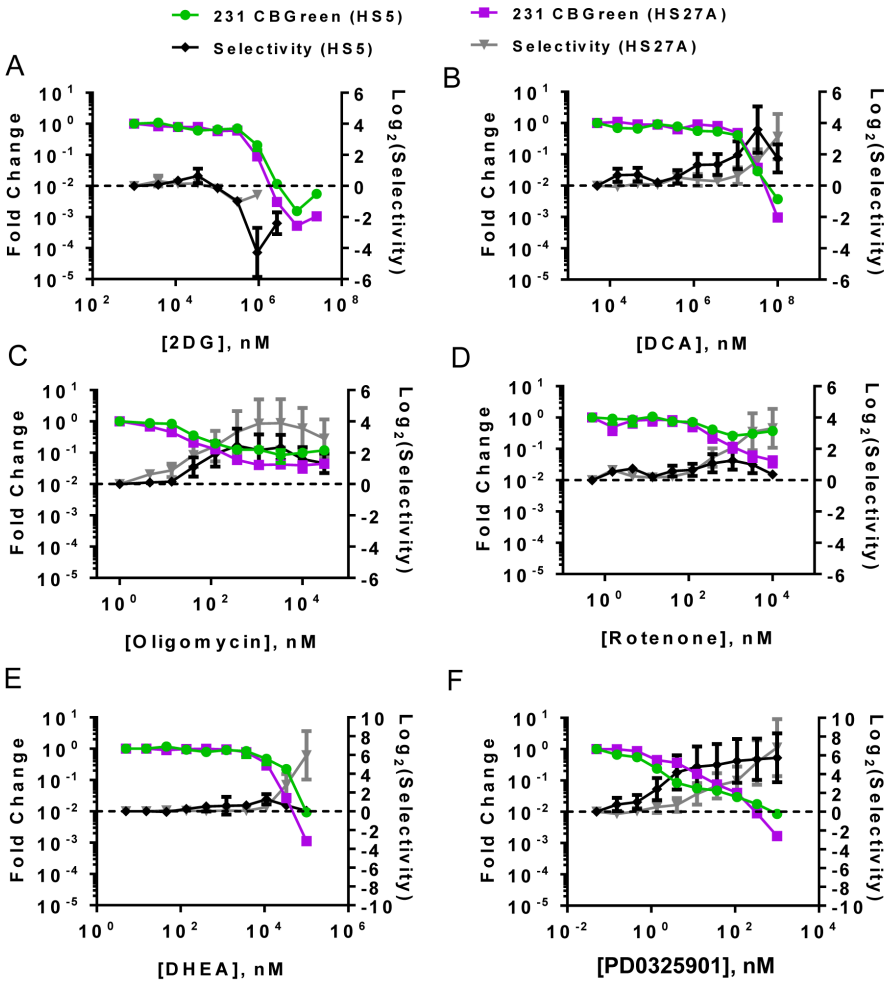

Figure 5.5. Molecular perturbation of glycolytic or oxidative metabolism reveals selective elimination of cancer or stromal cells. We plot dose-response curves for (A-B) MDA-MB-231 grown in (green curve) HS-5 or (purple curve) HS-27A spheroids. We plot their fold change Treatment with (A) 2-deoxy-D-glucose, (B) dichloroacetate, (C) oligomycin, (D) rotenone, (E) DHEA, and (F) PD0325901 result in typical sigmoidal dose-response curves. The selectivity curves corresponding to (black curves) HS-5 and (gray) HS-27A co-cultures represent the log-2-scaled ratio of CBRed to CBGreen signal, both normalized to untreated conditions and plotted on the right y-axis. Negative and positive values of selectivity denote relative loss of stromal or cancer signals. We omit selectivity values for dose levels with both CBGreen and CBRed signals less than 1% of untreated.

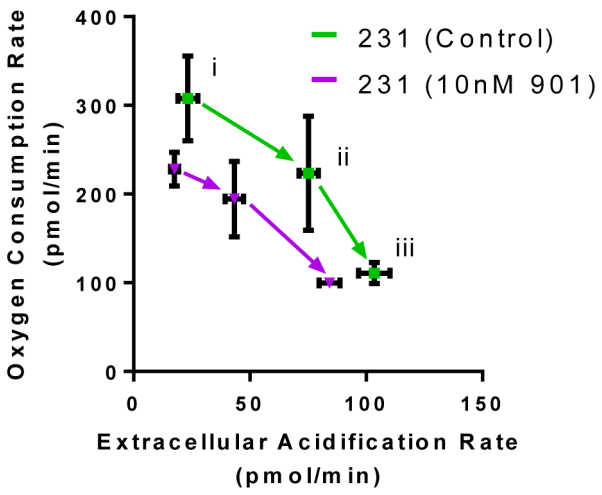

Figure 5.6. Suppression of metabolism by PD0325901 for MDA-MB-231 cells. Similar to Figure 5.1B, we plotted the oxygen consumption rate and extracellular acidification rate for MDA-MB-231 cells after sequential baseline (i) glutamine conditions, (ii) after injection of 25mM glucose, or (iii) after injection of 1μM oligomycin in the XF^{e}96 Seahorse Biosciences assay. Averages are pooled for N=6 wells over three consecutive mixing-measurement cycles. Assays were seeded overnight with 15x10^{3} cancer cells per well. After allowing cells to firmly adhere, we treated cancer cells with PD0325901 for 12 hours prior to the assay. We incubated for 1 hour prior to measurement in un-buffered media containing essential amino acids and glutamine, per manufacture recommendation for the XF Glycolysis Stress Test.

Table 5.1. Summary of metabolic interdependence on glucose and glutamine withdrawal. The qualitative characteristics designate positive or negative association with fraction of signal remaining as compared to the high glucose and high glutamine condition, for glucose and glutamine extremes (- indicated > 1.0, +/- no change, + 0.5-1.0, ++ 0.2-0.5 fraction remaining, +++ 0.0-0.2 fraction remaining).

Cell Type (Stromal Pair)	Cell Characteristic	Glucose Dependence	Glutamine Dependence
231 (HS5)	Triple Negative, Active MEK	++	++
231 (HS27A)		++	++
468 (HS5)	Triple Negative	+++	+++
468 (HS27A)		+/-	+/-
T47D (HS5)	ER^{+}	+++	+/-
T47D (HS27A)		++	++
HS5*	MSC-derived Cell Line	+++	-
HS27A*	MSC-derived Cell Line	+	+

5.7 References

1. Demicheli R, Terenziani M, & Bonadonna G (1998) Estimate of tumor growth time for breast cancer local recurrences: rapid growth after wake-up? *Breast Cancer Res Treat* 51(2):133-137.
2. Demicheli R (2001) Tumour dormancy: findings and hypotheses from clinical research on breast cancer. *Seminars in Cancer Biology*, (Elsevier), pp 297-306.
3. Brackstone M, Townson JL, & Chambers AF (2007) Tumour dormancy in breast cancer: an update. *Breast Cancer Res* 9(3):208.
4. Suda T, Takubo K, & Semenza Gregg L (2011) Metabolic Regulation of Hematopoietic Stem Cells in the Hypoxic Niche. *Cell Stem Cell* 9(4):298-310.
5. Alonso S, Su M, Jones R, & Ghiaur G (2014) The stem cell niche detoxifies chemotherapy and protects malignant hematopoietic cells via expression of cytochrome P450 enzymes. *Cancer Research* 74(19 Supplement):4842-4842.
6. Eliasson P & Jönsson J-I (2010) The hematopoietic stem cell niche: Low in oxygen but a nice place to be. *Journal of cellular physiology* 222(1):17-22.
7. Arai F & Suda T (2007) Maintenance of quiescent hematopoietic stem cells in the osteoblastic niche. *Annals of the New York Academy of Sciences* 1106(1):41-53.
8. Lim PK*, et al.* (2011) Gap junction-mediated import of microRNA from bone marrow stromal cells can elicit cell cycle quiescence in breast cancer cells. *Cancer Res.* 71(5):1550-1560. doi: 1510.1158/0008-5472.CAN-1510-2372. Epub 2011 Feb 1522.
9. Parmar K, Mauch P, Vergilio J-A, Sackstein R, & Down JD (2007) Distribution of hematopoietic stem cells in the bone marrow according to regional hypoxia. *Proceedings of the National Academy of Sciences* 104(13):5431-5436.
10. Spencer JA*, et al.* (2014) Direct measurement of local oxygen concentration in the bone marrow of live animals. *Nature* 508(7495):269-273.
11. Warburg OH & Dickens F (1930) *The metabolism of tumours: investigations from the Kaiser Wilhelm Institute for Biology, Berlin-Dahlem* (Constable & Company Limited).
12. Ward Patrick S & Thompson Craig B (2012) Metabolic Reprogramming: A Cancer Hallmark Even Warburg Did Not Anticipate. *Cancer Cell* 21(3):297-308.
13. Hanahan D & Weinberg RA (2011) Hallmarks of cancer: the next generation. *Cell* 144(5):646-674.
14. Zhang J, Nuebel E, Daley George Q, Koehler Carla M, & Teitell Michael A (2012) Metabolic Regulation in Pluripotent Stem Cells during Reprogramming and Self-Renewal. *Cell Stem Cell* 11(5):589-595.
15. Pattappa G, Heywood HK, de Bruijn JD, & Lee DA (2011) The metabolism of human mesenchymal stem cells during proliferation and differentiation. *Journal of cellular physiology* 226(10):2562-2570.
16. Guo H-W*, et al.* (2008) Reduced nicotinamide adenine dinucleotide fluorescence lifetime separates human mesenchymal stem cells from differentiated progenies. *BIOMEDO* 13(5):050505-050505-050503.
17. Chen CT, Shih YRV, Kuo TK, Lee OK, & Wei YH (2008) Coordinated changes of mitochondrial biogenesis and antioxidant enzymes during osteogenic differentiation of human mesenchymal stem cells. *Stem Cells* 26(4):960-968.

18. Quinn KP, *et al.* (2013) Quantitative metabolic imaging using endogenous fluorescence to detect stem cell differentiation. *Scientific reports* 3.
19. Metallo CM, *et al.* (2012) Reductive glutamine metabolism by IDH1 mediates lipogenesis under hypoxia. *Nature* 481(7381):380-384.
20. Prigione A, Fauler B, Lurz R, Lehrach H, & Adjaye J (2010) The Senescence‐Related Mitochondrial/Oxidative Stress Pathway is Repressed in Human Induced Pluripotent Stem Cells. *Stem Cells* 28(4):721-733.
21. Chen C, *et al.* (2008) TSC–mTOR maintains quiescence and function of hematopoietic stem cells by repressing mitochondrial biogenesis and reactive oxygen species. *The Journal of Experimental Medicine* 205(10):2397-2408.
22. Chiche J, *et al.* (2010) Hypoxic enlarged mitochondria protect cancer cells from apoptotic stimuli. *J Cell Physiol.* 222(3):648-657. doi: 610.1002/jcp.21984.
23. Folmes Clifford DL, Dzeja Petras P, Nelson Timothy J, & Terzic A (2012) Metabolic Plasticity in Stem Cell Homeostasis and Differentiation. *Cell Stem Cell* 11(5):596-606.
24. Schumacker PT (2006) Reactive oxygen species in cancer cells: Live by the sword, die by the sword. *Cancer Cell* 10(3):175-176.
25. Morrison SJ & Scadden DT (2014) The bone marrow niche for haematopoietic stem cells. *Nature* 505(7483):327-334.
26. Nombela-Arrieta C, *et al.* (2013) Quantitative imaging of haematopoietic stem and progenitor cell localization and hypoxic status in the bone marrow microenvironment. *Nat Cell Biol* 15(5):533-543.
27. Patel SA, Dave MA, Murthy RG, Helmy KY, & Rameshwar P (2011) Metastatic breast cancer cells in the bone marrow microenvironment: novel insights into oncoprotection. *Oncol Rev.* 5(2):93-102.
28. Roecklein BA & Torok-Storb B (1995) Functionally distinct human marrow stromal cell lines immortalized by transduction with the human papilloma virus E6/E7 genes. *Blood.* 85(4):997-1005.
29. Graf L, Iwata M, & Torok-Storb B (2002) Gene expression profiling of the functionally distinct human bone marrow stromal cell lines HS-5 and HS-27a. *Blood* 100(4):1509-1511.
30. Zhang C, *et al.* (2011) Paracrine factors produced by bone marrow stromal cells induce apoptosis and neuroendocrine differentiation in prostate cancer cells. *The Prostate* 71(2):157-167.
31. Li X, Marcondes A, Ragoczy T, Telling A, & Deeg H (2013) Effect of intravenous coadministration of human stroma cell lines on engraftment of long-term repopulating clonal myelodysplastic syndrome cells in immunodeficient mice. *Blood cancer journal* 3(4):e113.
32. Weisberg E, *et al.* (2012) Using combination therapy to override stromal-mediated chemoresistance in mutant FLT3-positive AML: synergism between FLT3 inhibitors, dasatinib/multi-targeted inhibitors and JAK inhibitors. *Leukemia* 26(10):2233-2244.
33. Covas DT, *et al.* (2008) Multipotent mesenchymal stromal cells obtained from diverse human tissues share functional properties and gene-expression profile with CD146+ perivascular cells and fibroblasts. *Experimental hematology* 36(5):642-654.

34. Iwata M, Sandstrom RS, Delrow JJ, Stamatoyannopoulos JA, & Torok-Storb B (2014) Functionally and phenotypically distinct subpopulations of marrow stromal cells are fibroblast in origin and induce different fates in peripheral blood monocytes. *Stem Cells Dev.* 23(7):729-740. doi: 710.1089/scd.2013.0300. Epub 2013 Nov 1023.
35. Whiteside T (2008) The tumor microenvironment and its role in promoting tumor growth. *Oncogene* 27(45):5904-5912.
36. Gajewski TF, Schreiber H, & Fu Y-X (2013) Innate and adaptive immune cells in the tumor microenvironment. *Nature immunology* 14(10):1014-1022.
37. Mayers JR & Vander Heiden MG (2015) Famine versus feast: understanding the metabolism of tumors in vivo. *Trends in Biochemical Sciences*.
38. Martinez-Outschoorn U, Sotgia F, & Lisanti MP (2014) Tumor microenvironment and metabolic synergy in breast cancers: critical importance of mitochondrial fuels and function. *Seminars in oncology*, (Elsevier), pp 195-216.
39. Hirschhaeuser F, Sattler UG, & Mueller-Klieser W (2011) Lactate: a metabolic key player in cancer. *Cancer Research* 71(22):6921-6925.
40. Ko Y-H*, et al.* (2011) Glutamine fuels a vicious cycle of autophagy in the tumor stroma and oxidative mitochondrial metabolism in epithelial cancer cells: Implications for preventing chemotherapy resistance. *Cancer biology & therapy* 12(12):1085-1097.
41. Kojima T, Moraes C, Cavnar SP, Luker GD, & Takayama S (2015) Surface-templated hydrogel patterns prompt matrix-dependent migration of breast cancer cells towards chemokine-secreting cells. *Acta biomaterialia* 13:68-77.
42. Miyawaki A (2003) Visualization of the spatial and temporal dynamics of intracellular signaling. *Dev Cell* 4(3):295-303.
43. Cavnar SP, Salomonsson E, Luker KE, Luker GD, & Takayama S (2013) Transfer, Imaging, and Analysis Plate for Facile Handling of 384 Hanging Drop 3D Tissue Spheroids. *Journal of laboratory automation*:2211068213504296.
44. Walsh AJ*, et al.* (2013) Optical metabolic imaging identifies glycolytic levels, subtypes, and early-treatment response in breast cancer. *Cancer Research* 73(20):6164-6174.
45. Huang S, Heikal AA, & Webb WW (2002) Two-photon fluorescence spectroscopy and microscopy of NAD (P) H and flavoprotein. *Biophysical journal* 82(5):2811-2825.
46. Longati P*, et al.* (2013) 3D pancreatic carcinoma spheroids induce a matrix-rich, chemoresistant phenotype offering a better model for drug testing. *BMC Cancer* 13(1):95.
47. Skala MC*, et al.* (2007) In vivo multiphoton microscopy of NADH and FAD redox states, fluorescence lifetimes, and cellular morphology in precancerous epithelia. *Proceedings of the National Academy of Sciences* 104(49):19494-19499.
48. Tsai AG*, et al.* (1998) Microvascular and tissue oxygen gradients in the rat mesentery. *Proceedings of the National Academy of Sciences* 95(12):6590-6595.
49. Thomlinson R & Gray L (1955) The histological structure of some human lung cancers and the possible implications for radiotherapy. *British Journal of Cancer* 9(4):539.

50. Chow DC, Wenning LA, Miller WM, & Papoutsakis ET (2001) Modeling pO 2 distributions in the bone marrow hematopoietic compartment. II. Modified Kroghian models. *Biophysical journal* 81(2):685-696.
51. Yin Y*, et al.* (2015) Normalization of CD4+ T cell metabolism reverses lupus. *Science Translational Medicine* 7(274):274ra218.
52. Lemons JM*, et al.* (2010) Quiescent fibroblasts exhibit high metabolic activity. *PLoS biology* 8(10):e1000514.
53. Gaglio D*, et al.* (2011) Oncogenic K-Ras decouples glucose and glutamine metabolism to support cancer cell growth. *Molecular Systems Biology* 7(1):n/a-n/a.

Chapter Six: Future Goals and Directions

6.1 Summary

The primary goal of this dissertation was to develop systems that model compartments of the metastatic cascade that are difficult to analyze experimentally. By experimentally beginning to bridge the physical and biological dimensionality gap between standard *in vitro* conditions and *in vivo* physiology, this dissertation highlights that systems of interacting cellular components behave very differently than individual components alone. In the metastatic process, multiple cells interact to drive bulk phenomena and rare, single cell events that contribute to cell functions and treatment efficacy. By increasing the number of these interacting components and improving the scales of observation in our experimental systems (single and bulk events), we were able to observed how relatively few cells interact in primary and metastatic sites and may contribute to metastasis.

We highlight the success of using our *in vitro* models to increase dimensionality (physical and biological), to integrate the entire microenvironment (biochemical, biomechanical, metabolic), and create insights that predict *in vivo* responses. Firstly, in our source sink model we found a high-matrix-binding chemokine isoform to drive high sensitivity migration, be more refractory towards molecular inhibition even at low secretion rates, to work independently of receptor-based scavenging, and to have increased expression in advanced breast cancer as compared to other isoforms of this chemokines. The second *in vivo* insight we found was using our bone marrow spheroid model to identify

therapy combinations that predicted complete elimination of breast cancer cells from mouse bone marrow. These two examples highlight the benefits of developing robust and practical experimental systems that better capture *in vivo* physiology of metastasis.

By studying processes underlying metastasis, we hope to screen for prognostic markers and therapies that prevent and/or eliminate metastatic disease. In order to meet these challenges, we developed multiple tissue engineering and imaging systems to bridge the dimensionality gap between standard *in vitro* assays and *in vivo* physiology. Further development of the systems utilized in this dissertation will advance our understanding of metastatic disease. In particular, leveraging these systems in combination with three specific avenues will provide substantial advances towards improving clinical medicine, including further increasing dimensionality, computational modeling, and patient-specific models.

6.2 Increasing Dimensionality

In vivo physiology is inherently multi-dimensional, involving multiple cell types, time scales, and 3D physical interactions. Further development of practical and robust *in vitro* models that capture *in vivo* characteristics will improve our ability to model, screen for markers, and design therapies against metastatic disease. Shifting from simple, relatively amorphous 3D models (spheroids, hydrogels), towards highly controlled, organoid systems is one such improvement in dimensionality (1). Interfacing organoid cultures with microfluidic control, reagent delivery and mechanical stimulation will further our ability to model physiology with "organ-on-chip" technology" (2). For instance, encapsulating skin, hair, (3), brain (4), bone marrow (5), intestines, and/or liver (6) on microfluidic chips allows perfusion, extended observation, fine-tuned delivery of reagents,

and/or pharmacokinetic-pharmacodynamic studies. In addition to increasing the biological and physical dimensionality of tissue engineering tools, improving the time- and spatial- resolution of analysis will further advance our understanding of metastasis. Such advances also require integration of novel optical and molecular imaging tools to improve spatial and temporal scales of observation.

From a practical standpoint, simple tools that increase physiological dimensionality are most critical to near term advances. For instance we used surface-templated 3D hydrogels to recreate source-sink migration (7). In this study, proteoglycans in the patterned extracellular matrix were critical for shaping, presentation, and/or sensing of chemotactic gradients. Similarly, we used a similar 3D cell-laden hydrogel system to adapt standard 384 well 2D assays to recreate decreased sensitivity to therapies within 3D culture (8). Building upon these systems, adding physical and biological dimensionality, and improving our observation scales will improve our knowledge of how to impede/eliminate the few cells that interact with their microenvironment to metastasize.

6.3 Computational Modeling

Computational modeling will aid the development and analysis of increased dimensionality within *in vitro* and *in vivo* models (9) (10) (11). With increasing dimensionality of *in vitro* assays, experiments become more costly, more multivariate and complicated to analyze, and collectively more difficult to interpret. Computational models provide three avenues for improvement to experimental models: 1) preemptive sensitivity analysis to define/reduce the number of minimally necessary experiments, 2) integration of multiple scales of data (DNA/RNA sequencing, proteomic, signaling, phenotypic outcomes, and response to therapy), and 3) improving data interpretation at scales by

typical sampling. One example is our use of agent-based models to visualize the magnitude and shape of chemokine gradients, which were impossible to observe in our *in vitro* model of source-sink migration (Chang, 2015, work in progress). By fitting experimental cell migration data to ODE models that recreate intracellular receptor-ligand dynamics, extracellular ligand kinetics (mass transfer, surface binding, etc), and agent-based cell movement, we extended our 2D microfluidic source-sink model to predictions of gradient formation and migration *in vivo*. More so, we modeled the limited efficacy of receptor-ligand inhibitors based on high local concentration of high binding ligand isoforms. We expect that combining similar modeling approaches with large cohorts of gene expression data and metastatic outcomes will further link clinical and experimental data to provide prognostic markers and therapeutic opportunities.

6.4 Patient-specific Models

Improved culture techniques, tools to induce cell differentiation, and improved tissue sampling/expansion techniques make working with primary patient tissues increasingly feasible (1). Combining tissue engineering and molecular imaging techniques described in this dissertation with primary patient samples will allow direct drug screening against patient-specific phenotypes. For example, routine bone marrow biopsies for breast cancer patients enable growth and expansion of primary bone marrow stromal cells that form 3D spheroids (12). Culturing of patient-matched circulating and resected primary tumor cells and within these patient bone marrow spheroids would allow screening against refractory cancer cells in this microenvironent. Multi-modal imaging tools have been described to work with primary samples, which would enable the many strategies contained in this dissertation. Using primary patient samples within these experimental

models may provide avenues to experimentally predict therapies that will limit metastatic disease and relapse for patients. These combined strategies may begin to allow drug development that accounts for intra- and inter-patient disease heterogeneity, which is a major challenge to successful treatment of all diseased cells.

6.5 References

1. Shamir ER & Ewald AJ (2014) Three-dimensional organotypic culture: experimental models of mammalian biology and disease. *Nature Reviews Molecular Cell Biology* 15(10):647-664.
2. Huh D, Hamilton GA, & Ingber DE (2011) From 3D cell culture to organs-on-chips. *Trends in cell biology* 21(12):745-754.
3. Ataç B*, et al.* (2013) Skin and hair on-a-chip: in vitro skin models versus ex vivo tissue maintenance with dynamic perfusion. *Lab on a Chip* 13(18):3555-3561.
4. Huang Y, Williams JC, & Johnson SM (2012) Brain slice on a chip: opportunities and challenges of applying microfluidic technology to intact tissues. *Lab on a Chip* 12(12):2103-2117.
5. Torisawa Y-s*, et al.* (2014) Bone marrow–on–a–chip replicates hematopoietic niche physiology in vitro. *Nature Methods*.
6. van Midwoud PM, Merema MT, Verpoorte E, & Groothuis GMM (2010) A microfluidic approach for in vitro assessment of interorgan interactions in drug metabolism using intestinal and liver slices. *Lab on a Chip* 10(20):2778-2786.
7. Kojima T, Moraes C, Cavnar SP, Luker GD, & Takayama S (2015) Surface-templated hydrogel patterns prompt matrix-dependent migration of breast cancer cells towards chemokine-secreting cells. *Acta biomaterialia* 13:68-77.
8. Leung BM*, et al.* (2014) Microscale 3D Collagen Cell Culture Assays in Conventional Flat-Bottom 384-Well Plates. *Journal of laboratory automation*:2211068214563793.
9. Wiley HS, Shvartsman SY, & Lauffenburger DA (2003) Computational modeling of the EGF-receptor system: a paradigm for systems biology. *Trends in cell biology* 13(1):43-50.
10. Loew LM & Schaff JC (2001) The Virtual Cell: a software environment for computational cell biology. *Trends in biotechnology* 19(10):401-406.
11. Kitano H (2002) Computational systems biology. *Nature* 420(6912):206-210.
12. Bernardo ME*, et al.* (2007) Human bone marrow–derived mesenchymal stem cells do not undergo transformation after long-term in vitro culture and do not exhibit telomere maintenance mechanisms. *Cancer Research* 67(19):9142-9149.

Appendix A. Chapter 2 Supporting Information

7.1 Supplemental Figures

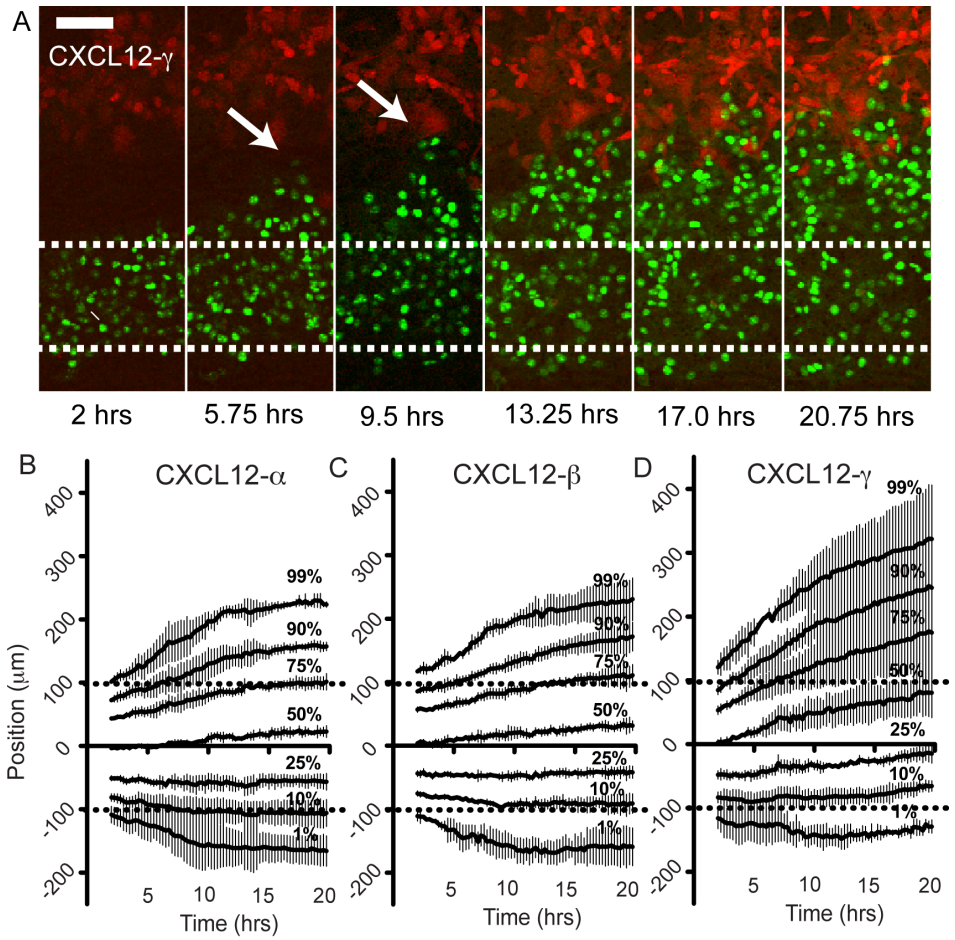

Figure A.1. CXCL12-γ enhances initial chemotaxis of CXCR4+ cells. *(A)* Time lapse images of CXCR4+ cells (green) migrating towards CXCL12-γ secreting cells (red). Imaging began two hours after final seeding (t=2 hrs), followed by images every 15 minutes for ~20 hours. Representative images are shown. The dotted white lines designate the channel location and starting position. The arrows denote leading sprout formation and the scale bar indicates 100 μm length. Representative time lapse videos are found in Supplemental Video V1. *(B-D)* Chemotaxis of CXCR4+ cells toward cells secreting various CXCL12 isoforms was quantified by live cell microscopy. Data show percentile distributions of CXCR4+ cell positions over time ± S.D. beginning two hours after patterning cells (n = 3 individual set ups, ~1200 cells total). The 50% line is the median position of the cells. The dashed lines denote the channel boundries where cells were initially patterned.

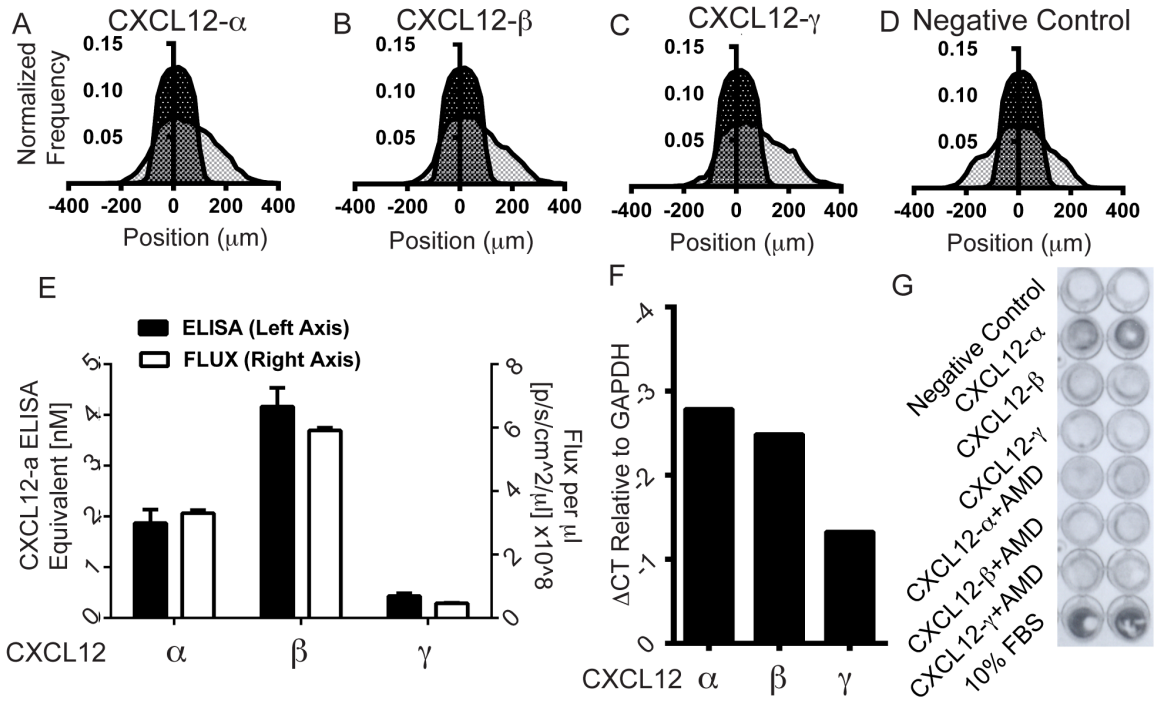

Figure A.2. Increased chemotaxis of CXCR4+ cells toward CXCL12-γ. *(A-D)* Position frequency distribution of CXCR4+ cells relative to the starting point (channel boundaries). Frequencies are normalized to the number of cells per view. These data are composite distributions for each CXCL12-isoform representing 10-11 devices with 6 view fields each (~$15x10^3$ cells total per histogram). The black distribution represents the pooled initial distribution. Graphs depict chemotaxis toward CXCL12 as a shift to positive positions with higher values denoting greater distances traveled by cells. *(E)* Production of CXCL12 isoforms after 24 hours based on corresponding *Gaussia* luciferase activity and CXCL12-α ELISA equivalent measurements. We measured CXCL12-isoform content in supernatants from 10^6 231 cells secreting individual CXCL12-isoforms. We measured *Gaussia* luciferase activity with 1:5 final dilution of supernatants in a 1:100 dilution in PBS of 1 mg per ml coelenterazine (50 μl total). Data are reported as mean ± S.E.M. for 6 measurements each in two independent setups with paired ELISA and bioluminescence measurements (n = 12 total). Each ELISA well was measured in quadruplicate. *(F)* Relative qRT-PCR amplification cycle number (ΔCT) as compared to GAPDH. We measured comparable mRNA levels of CXCL12-isoforms in our transduced cells. CXCL12 was not detectable in the parental cells. *(G)* Transwell migration towards 100 ng/ml CXCL12-isoforms in the absence or presence of CXCR4 inhibitor AMD3100 (1 μM). Cells migrating through the membrane in response to equal amounts of cell-secreted CXCL12 isoforms based on *Gaussia* luciferase activity were detected by staining with crystal violet. Darker staining shows relatively greater cell migration. 10% fetal bovine serum (FBS) was used as a positive control.

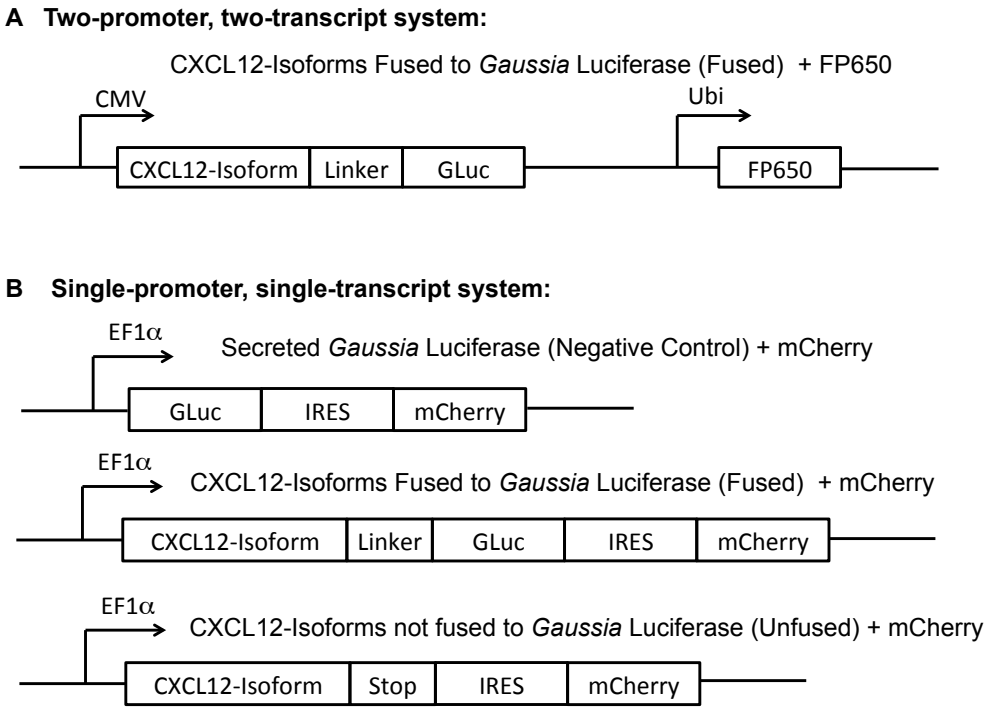

Figure A.3. CXCL12-isoform vector construction. We used two viral constructs to express CXCL12-isoforms in mammalian cells. *(A)* Schematic representation of the two-part construct with CXCL12-isoforms fused to *Gaussia* luciferase under one the CMV promoter and the far-red fluorescent protein under the Ubi promoter. This strategy forgoes the ability to express and sort for *Gaussia* luciferase-unfused CXCL12. We used this construction for most data represented in this paper. *(B)* Schematic representations of the one-transcript expression system using and internal ribosomal entry site (IRES) separating two genes of interest under a single EF1α promoter. This strategy enabled more quantitative control of CXCL12 abundance based on proportional expression with mCherry. The IRES construct also enabled flow cytometry sorting for CXCL12 with a stop codon rather than linked to *Gaussia* luciferase. We used the IRES construct for comparison of the biological effect of recombinant *Gaussia* luciferase fusions in Figure A.2.

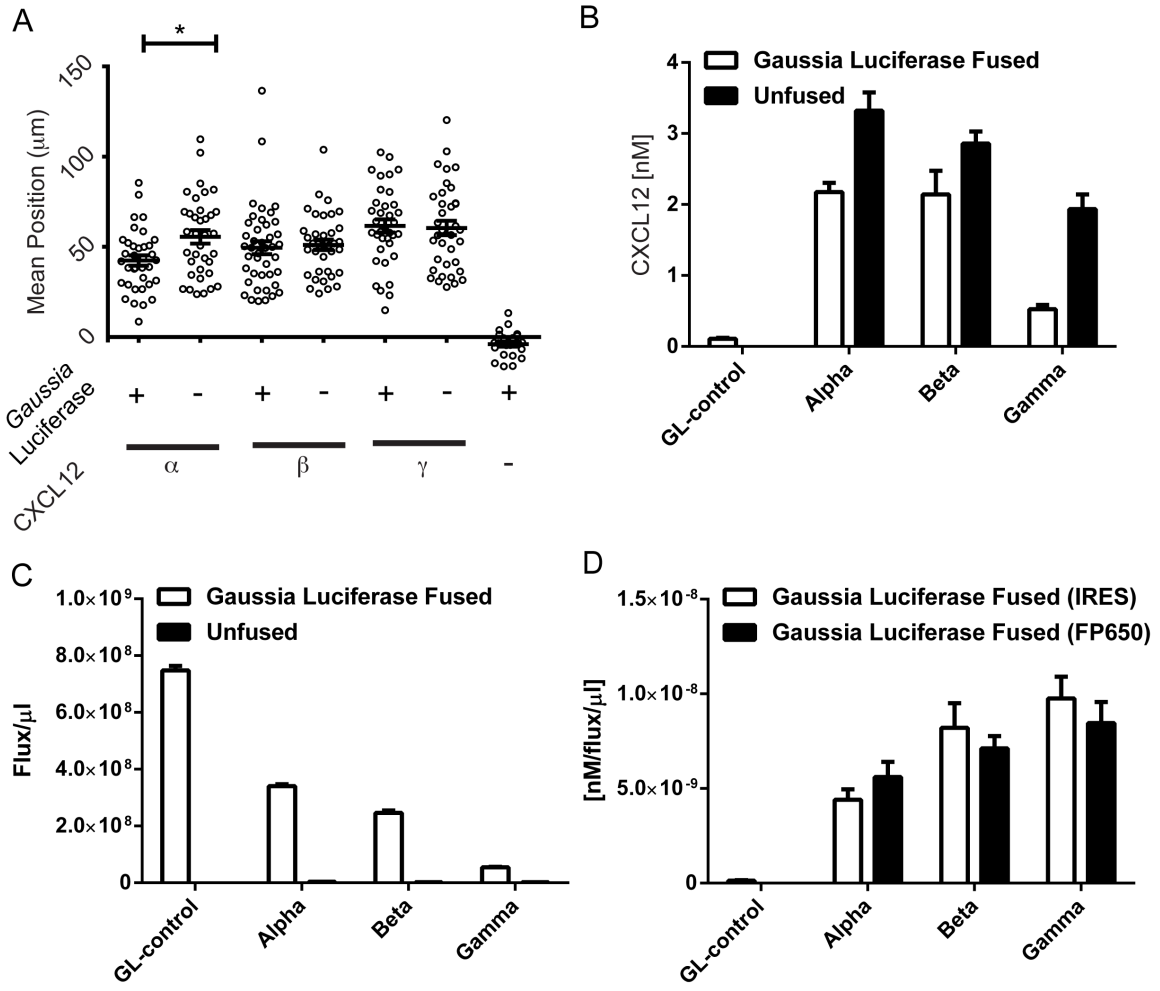

Figure A.4. Characterization to recombinant CXCL12-isoforms with and without *Gaussia* luciferase fusions. *(A)* Average position of CXCR4+ cells after 24 hours of migration toward cells expressing IRES constructs for CXCL12-α, β, or γ with (+) and without (-) recombinant *Gaussia* luciferase fusion, as described in Figure A.2 part B. The negative control cells secrete *Gaussia* luciferase without CXCL12. Data are shown as mean values ± S.E.M. (n=6 view fields for 4-6 devices per condition, similar to described in Fig. 2.1). The bars represent the statistical comparison of all fractions to the non-secreting control (0%). Statistical demarcations directly above data are comparisons to the 100% secreting fraction (* $p<0.005$). Matched conditions were performed in parallel. We measured secretion of IRES CXCL12 constructs based on corresponding equivalent ELISA reactivity, which was developed and calibrated towards CXCL12-α *(B)* and *Gaussia* luciferase activity *(C)* in the supernatants from 10^6 231 cells in 30 mm dishes after 24 hours. *(B)* By ELISA measurements, CXCL12 expressed without *Gaussa* luciferase fusion was more abundant and/or more efficiently measured by ELISA. *(C)* Corresponding bioluminescent imaging of *Gaussia* luciferase activity revealed only background signal from the unfused CXCL12 constructs but substantial signal from the negative control secreted *Gaussia* luciferase (GL-control) and from the CXCL12-fusions. Bioluminescence data is normalized per μl of supernatant added. *(D)* Comparison of the measured ELISA readings per bioluminescent flux revealed a rank-order increase in the nM per flux per μl quantitation of CXCL12-fusions from both the IRES constructs and the FP650 constructs. These measures were on the same order of magnitude for all three isoforms, allowing us to use *Gaussia* luciferase activity to estimate the quantity of CXCL12-isoforms in supernatants. Data are reported as mean ± S.E.M. for 6 measurements each in two independent setups with paired ELISA and bioluminescence measurements (n = 12 total). Each ELISA well was measured in quadruplicate.

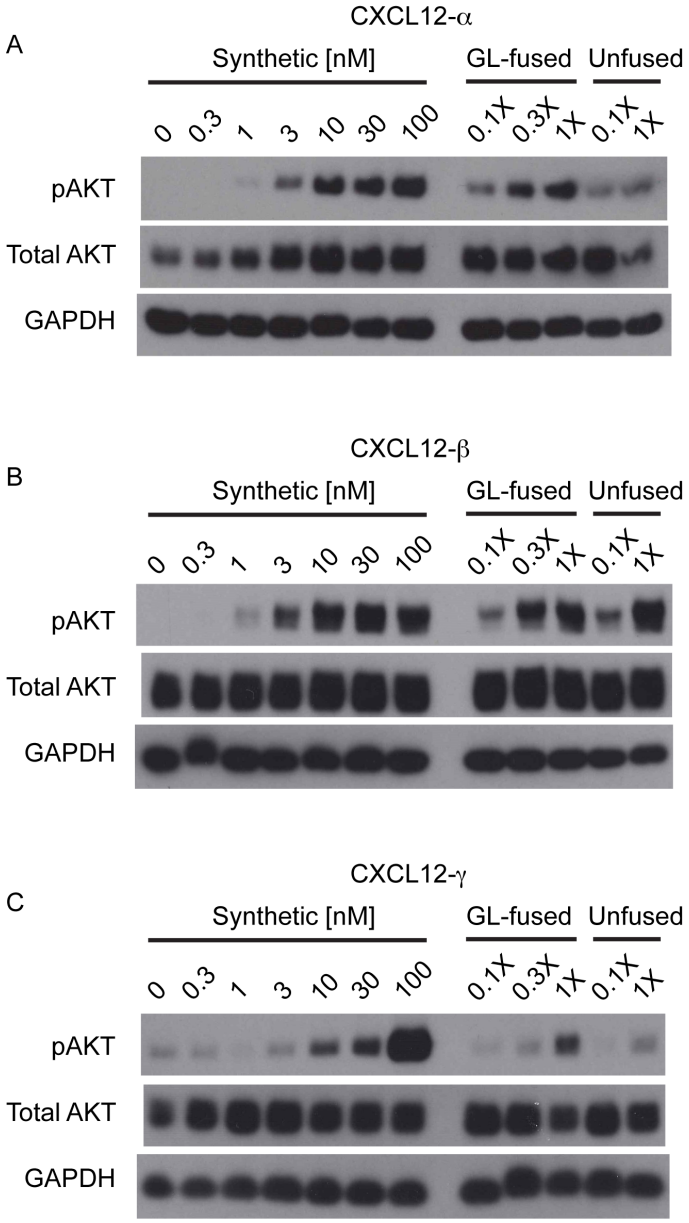

Figure A.5. CXCL12-isoform induction of AKT phosphorylation. *(A-C)* Western blot analysis of AKT phosphorylation downstream of CXCR4 in MDA-MB-231 cells for CXCL12-α, -β, and -γ, respectively. We measured total AKT and GAPDH as loading controls.

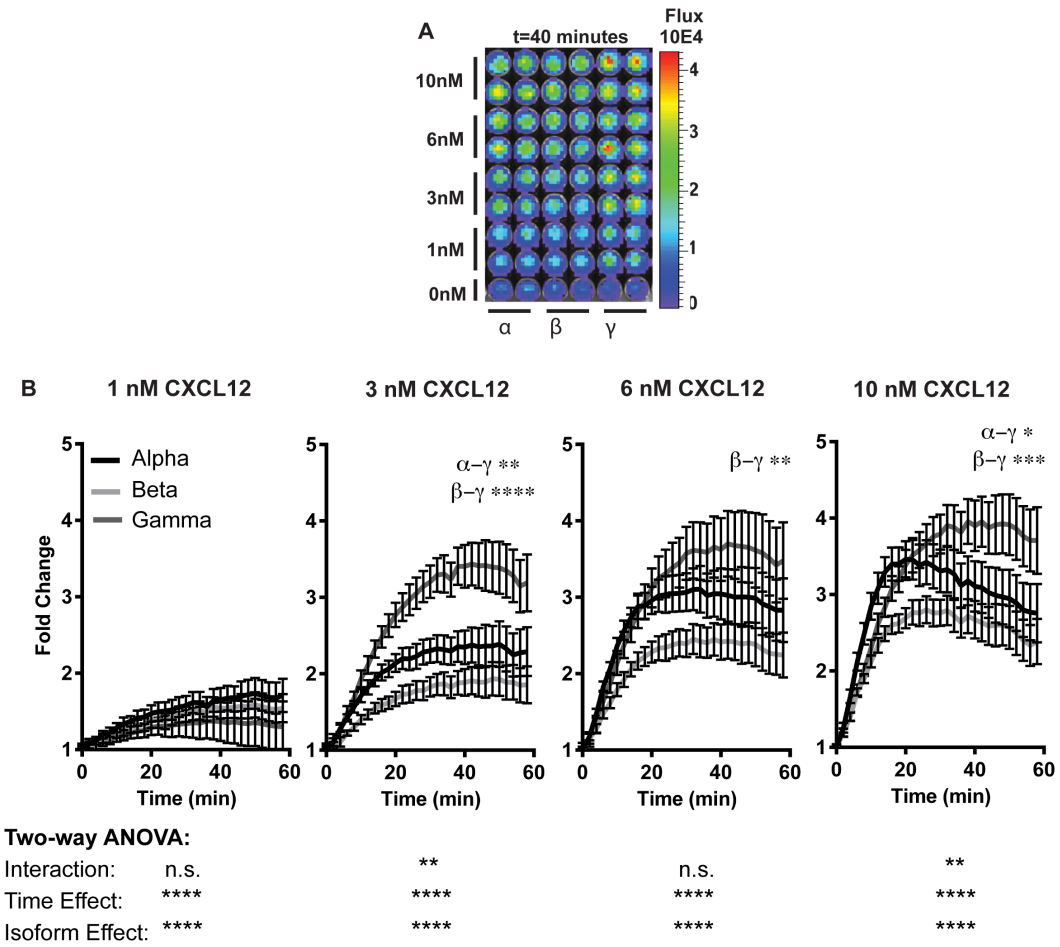

Figure A.6. Representative bioluminescence images of β-arrestin 2 recruitment to CXCR4 in response to CXCL12 isoforms. Dilutions of equimolar concentrations of recombinant CXCL12 isoforms were applied simultaneously to cells. This image was taken at t=40 minutes of a 1 hour time course. Scale bar depicts range of photon flux (p/s/cm^2) values with the pseudocolor dislay scale showing red and blue as highest and lowest values, respectively. The image depicted is representative two experimental runs.

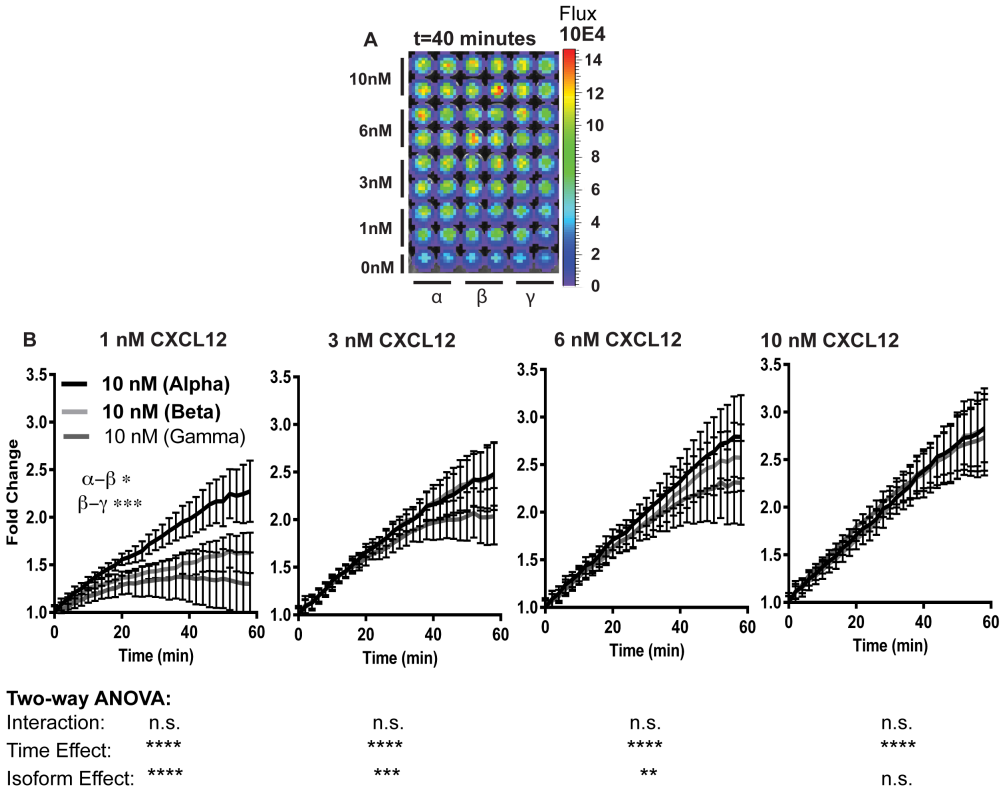

Figure A.7. Representative bioluminescence images of β-arrestin 2 recruitment to CXCR7 in response to CXCL12 isoforms. Cells expressing a luciferase complementation reporter for association of CXCR7 and β-arrestin 2 were incubated with increasing equimolar concentrations of synthetic CXCL12-α, β, or γ. Representative bioluminescence image from t=40 minutes from a one hour time course. Scale bar depicts range of photon flux (p/s/cm^2) values with pseudocolor display. The image depicted is representative two experimental runs.

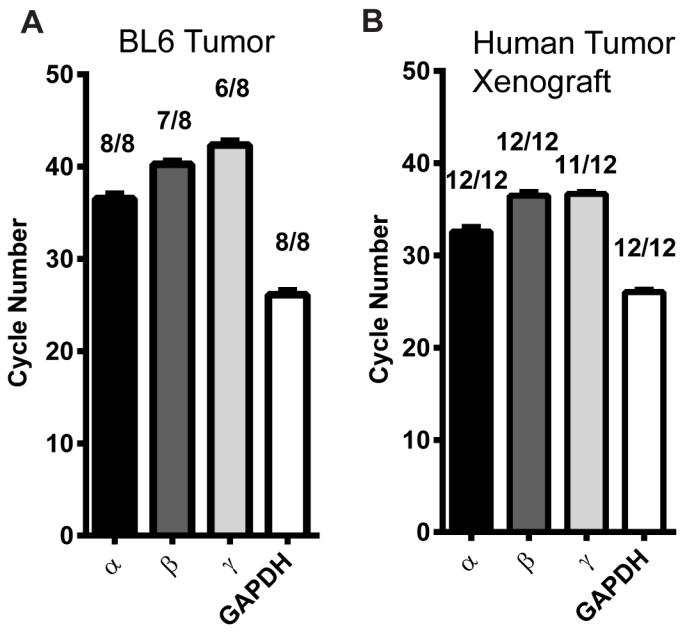

Figure A.8. Mouse expression of CXCL12-isoforms in primary breast tumors. Quantitative RT-PCR cycle numbers are reported for orthotopic implants of *(A)* syngenic implants of E0771 breast cancer cells in C57BL/6mice and *(D)* human xenograft of MDA-MB-231 cells in NSG mice. Tissues homogenates were analyzed from primary tumors. Numerals above data represent the fraction of samples positive for each transcript. Transcripts amplified below 40 qRT-PCR cycles we denoted as positive. Amplified gene product purity was also confirmed via gel electrophoresis.

7.2 Supplemental Results

Characterization of secreted Gaussia luciferase CXCL12-isoform-fusions

The single promoter, IRES-linked CXCL12 and mCherry construct facilitates characterization of CXCL12-isoforms fused or not fused with *Gaussia* luciferase. The internal ribosomal entry site (IRES)-linkage promotes proportional expression of both proteins, but limits translational efficiency and total protein levels as compared to single protein transcripts. For this reason, we also developed a vector to co-express CXCL12-isoforms fused to *Gaussia* luciferase and a far-red fluorescent protein (FP650) from two different promoters.

We used the IRES system to evaluate effects of the *Gaussia* luciferase fusion on biological activity of CXCL12-isoforms (Fig. S4). To characterize levels of secreted CXCL12 *Gaussia* luciferase fusions, we complemented ELISA reactivity with bioluminescence imaging. Although polyclonal ELISA antibodies were developed towards CXCL12-α, we measured the relative ELISA ng per bioluminescence flux to be on the same order of magnitude for all isoforms. All CXCL12-isoforms elicited chemotaxis of CXCR4+ cells independent of fusion to *Gaussia* luciferase. To measure the biological effect of recombinant *Gaussia* luciferase fusions, we measured phosphorylation of AKT, a known downstream target of CXCL12-CXCR4 signaling (Fig. S5). As compared with recombinant CXCL12-isoforms, CXCL12 secreted by 231 cells stimulated levels of AKT phosphorylation corresponding to the measured ELISA-based concentrations for each isoform, independent of fusion to *Gaussia* luciferase. For the *Gaussia* luciferase fusions, our bioluminescence-based measurement of chemokine concentration corresponded with the Western blot phosphorylation of AKT as compared with recombinant CXCL12-isoforms. In combination with our prior studies of CXCL12-α, these data show that CXCL12 isoforms retain expected biological activity when fused to *Gaussia* luciferase (Fig. S4-5)(1).

Since IRES-linkage may limit translational efficiency of both products, we used a two-promoter system to express higher levels of CXCL12-isoform fusions with *Gaussia* luciferase for subsequent studies (Fig. S2A). Similar to the IRES-linked expression system, ELISA and bioluminescence imaging provided complementary measures of chemokine production (Fig. 2F and S2B-D). We sorted cells for equal expression of co-expressed FP650 fluorescent protein, yielding comparable levels of mRNA for CXCL12 α and β with slightly lower levels of CXCL12-γ (Fig 2G). We note that CXCL12 transcripts were

undetectable in parental 231 cells, so source cells secreted only the desired isoform (data not shown).

7.3 Supplemental Discussion

For the simplest semi-quantitative conceptualization of increased CXCL12-γ potency, we posit that CXCL12 is a bivalent ligand between CXCR4 and heparan sulfate, a major component of cell surfaces and the extracellular compartment. Previous studies have shown that co-localization of heparan sulfate with CXCR4 cooperatively increases local concentrations of CXCL12, thus promoting signaling(2). To estimate the overall affinity of CXCL12-isoforms to CXCR4 and heparan sulfate, we extend a model developed to calculate the bivalent affinity of polymer-linked ligands(3, 4). The bivalent affinity is a multiplicative function of the two monovalent affinities of CXCL12 for CXCR4 and heparan sulfate (K_{R4} and K_{HS}) with the effective concentration of the multiple-binding ligand (C_{Eff}). The parameter C_{Eff} is based on molecular size, shape, and rigidity of the multiple-binding ligand, which we assume to be the same between CXCL12 isoforms and therefore we leave this as a constant. We also assume the distance between heparan sulfates and CXCR4 not to be limiting based on the high abundance and flexibility of heparan sulfates(5). Multiplication of the binding constant for CXCL12-isoforms to CXCR4 or heparan sulfate reveals ~6 fold greater apparent affinity for CXCL12-γ as compared to the α-isoform (Table S1). Although only semi-quantitative, this conceptual framework provides a potential mechanism for increased chemotactic potency of CXCL12-γ.

Table A.1. Affinities for CXCL12 isoforms towards CXCR4, heparan sulfate, and divalent CXCR4-HS complex.

	CXCL12-Isoforms		
Tumor Grade:	α	β	γ
CXCR4 (IC50 ~ K_{R4})(6)	15 nM	--	350 nM
Heparan Sulfate (K_{HS})(7)	200 nM	53 nM	1.5 nM
C_{Eff}*K_{R4}*K_{HS}	C_{Eff}*3000	--	C_{Eff}*525

Note: IC_{50} is proportional between α and γ for CXCR4 so we use it as a surrogate for K_d for CXCL12-γ. We assume C_{Eff} to be equal for both isoforms based on structural similarities.

7.4 Supplemental Methods

Text S1. ImageJ Script for Cell Position. The following imageJ script takes corresponding 8-bit phase contrast and fluorescent images and maps the coordinate of every cell. The script converts fluorescent images to binary images for a range of threshold values to identify both bright and dim cells. The threshold scan also identifies duplicate counts, which we exclude using an embedded loop comparison. The output coordinates were analyzed in Microsoft Excel.

```
macro "automated migration" {
waitForUser("Open Phase Contrast and Draw Rectangle");
run("Set Measurements...", "area center limit redirect=None decimal=3");
run("Clear Results");
myImageID = getImageID(); //get Image information

//Make Rectangle Manually, Delay, Check the Channel Position
setTool(0);
if(selectionType() != 0)
        exit("Sorry, no rectangle");
run("Measure");
area=getResult("Area",0);
xm=getResult("XM",0);
ym=getResult("YM",0);

run("Close All");
waitForUser("Open Fluorescence IMG");
myImageID2 = getImageID();
selectImage(myImageID2);
direct = getInfo("image.directory");
filename = getInfo("image.filename");

setThreshold(20, 255);
run("Convert to Mask");
run("Open");
run("Watershed");
run("Analyze Particles...", "size=30-300 circularity=0.00-1.00 show=Ellipses display clear");

for(i=nResults; i>0; i--) {
```

```
areai=getResult("Area",i-1);
xmi=getResult("XM",i-1);
ymi=getResult("YM",i-1);
setResult("Area",i,areai);
setResult("XM",i,xmi);

setResult("YM",i,ymi);}
setResult("Area",0,area);
setResult("XM",0,xm);
setResult("YM",0,ym);
updateResults();
run("Close All");

//Loop through thresholds, 5 threhold incraments

i=25;
while(i<75){open(direct+"/"+filename);
setThreshold(i, 255);
run("Convert to Mask");
run("Open");
run("Watershed");
        run("Analyze Particles...", "size=30-300 circularity=0.00-1.00 show=Ellipses display");
        run("Close All");
        i=i+5;}

//Loop through thresholds, 20 threshold increments

i=75;
while(i<250){open(direct+"/"+filename);
setThreshold(i, 255);
run("Convert to Mask");
run("Open");
run("Watershed");
        run("Analyze Particles...", "size=30-300 circularity=0.00-1.00 show=Ellipses display");
        run("Close All");
        i=i+20;}

//Remove Data with Duplicates,
run("Close All");

for(i=1; i<=nResults; i++) {
        for(j=i+1; j<nResults; j++)  {

//Speeds up program by not Processing NaNs as duplicates
                if(getResult("XM",j)==NaN)
                        j=nResults;
                if( abs(getResult("XM",i)-getResult("XM",j)) < 5 && abs(getResult("YM",i)-
getResult("YM",j)) < 5) {  for(k=j+1;k<nResults;k++){
                                areak=getResult("Area",k);
                                xmk=getResult("XM",k);
                                ymk=getResult("YM",k);
                                setResult("Area",k-1,areak);
                                setResult("XM",k-1,xmk);
                                setResult("YM",k-1,ymk);
                                setResult("Area",k,NaN);
```

```
                                        setResult("XM",k,NaN);
                                        setResult("YM",k,NaN);
                                }}}}

setResult("Area",0,area);
setResult("XM",0,xm);
setResult("YM",0,ym);
updateResults();

//Starts over for a new image
run("automated migration");
}
```

Table A.2 Cloning strategy for CXCL12 isoforms and *Gaussia* luciferase fusions.

	PCR template	template	5' primer	3' primer	sites
1	GL for fusions	pGLuc Basic, NEB	atgcgaattccggcggaggtggctccggaggcggtg ggagcgccaagcccaccgagaacaacgaagacttc	gcatgcggccgcttagtcaccaccggccccttg	EcoRI/NotI
2	secreted GL unfused	pGLuc Basic, NEB	atgcgctagccgcccaccatggagtcaaagttctg	gcatgcggccgcttagtcaccaccggccccttg	NheI/NotI
3	CXCL12-alpha for GL fusion	mCXCL12 (Luker et al., 2009b)	atgcctcgaggcccaccatggacgccaaggtcgtcg	gcatgaattccccttgtttaaagctttctccaggtac	XhoI/EcoRI
4	CXCL12-beta for GL fusion	mCXCL12 (Luker et al., 2009b)	atgcctcgaggcccaccatggacgccaaggtcgtcg	gcatgaattccccatcttgagcctctgtttaaagct ttctccaggtac	XhoI/EcoRI
5	CXCL12-gamma for GL fusion	synthetic gene (IDT)	ctcgaggccaccatggacgccaaggtcgtcgccgtgc tggccctggtgctggccgcgctcgcatcagtgacggt aaaccagtcagcctgagctaccgatgccccctgccggt tcttcgagagccacatcgccagagccaacgtcaagca ttgttgcacggctgaagaacacaacacaacagacaagtgtg catgaccgaaattaaagtggatccaagagtacctg gagaaagctttaacaagggcgcagaagaaaaa agtgggaaaaaagaaaagatagggaaaaaagaag cgacagaagagagaaaggctgcccagaaaaggaa aaacgggaattc	gcatgcggccgcttagtcaccaccggccccttg	XhoI/EcoRI
6	CXCL12-alpha unfused	mCXCL12 (Luker et al., 2009b)	atgctctagagccaccatggacgccaagg	gcatgcggccgcttacttgtttaaagctttctccagg	XbaI/NotI
7	CXCL12-beta unfused	mCXCL12 (Luker et al., 2009b)	atgctctagagccaccatggacgccaagg	gcatgcggccgctcacatcttgagcctctgtttaaa g	XbaI/NotI
8	CXCL12-gamma unfused	synthetic gene (IDT)	atgctctagagccaccatggacgccaagg	gcatgcggccgcttagttttccttttctgggcagcc	XbaI/NotI
9	CXCL12-GL fusions for FU650W	fusion constructs in pEGFP-N1	atgcttaattaatagtaatcaattacgggg (bases 6-27 of pEGFP-N1)	gcatttaattaatgtggtatggctgattatgatc (bases 1413-1435 of pEGFP-N1)	PacI
10	CXCL12-GL fusions for pLVX	fusion constructs in pEGFP-N1	atgctctagagccaccatggacgccaagg	gcatgcggccgcttagtcaccaccggccccttg	XbaI/NotI
11	AcGFP-nuc	pAcGFP1-Nuc (Clontech)	atgctctagagcagagctggtttagtgaaccg	atgtggtatggctgattaatgatc	XbaI

Luker, K., M. Gupta, and G. Luker. 2009a. Bioluminescent CXCL12 fusion protein for cellular studies of CXCR4 and CXCR7 Biotechniques. 47:625-632.

7.5 References

1. Luker K, Gupta M, & Luker G (2009) Bioluminescent CXCL12 fusion protein for cellular studies of CXCR4 and CXCR7 *Biotechniques* 47(1):625-632.
2. Valenzuela-Fernandez A*, et al.* (2001) Optimal inhibition of X4 HIV isolates by the CXC chemokine stromal cell-derived factor 1 alpha requires interaction with cell surface heparan sulfate proteoglycans. *J Biol Chem.* 276(28):26550-26558. Epub 22001 May 26514.
3. Kane RS (2010) Thermodynamics of Multivalent Interactions: Influence of the Linker. *Langmuir* 26(11):8636-8640.
4. Krishnamurthy VM, Semetey V, Bracher PJ, Shen N, & Whitesides GM (2007) Dependence of effective molarity on linker length for an intramolecular protein-ligand system. *J Am Chem Soc.* 129(5):1312-1320.
5. Kramer RH & Karpen JW (1998) Spanning binding sites on allosteric proteins with polymer-linked ligand dimers. *Nature.* 395(6703):710-713.
6. Laguri C*, et al.* (2007) The novel CXCL12gamma isoform encodes an unstructured cationic domain which regulates bioactivity and interaction with both glycosaminoglycans and CXCR4. *PLoS One* 2:e1110.
7. Rueda P*, et al.* (2008) The CXCL12gamma chemokine displays unprecedented structural and functional properties that make it a paradigm of chemoattractant proteins. *PLoS One* 3(7):e2543.

Appendix B: Chapter 3 Supporting Information

8.1 Supplemental Figures

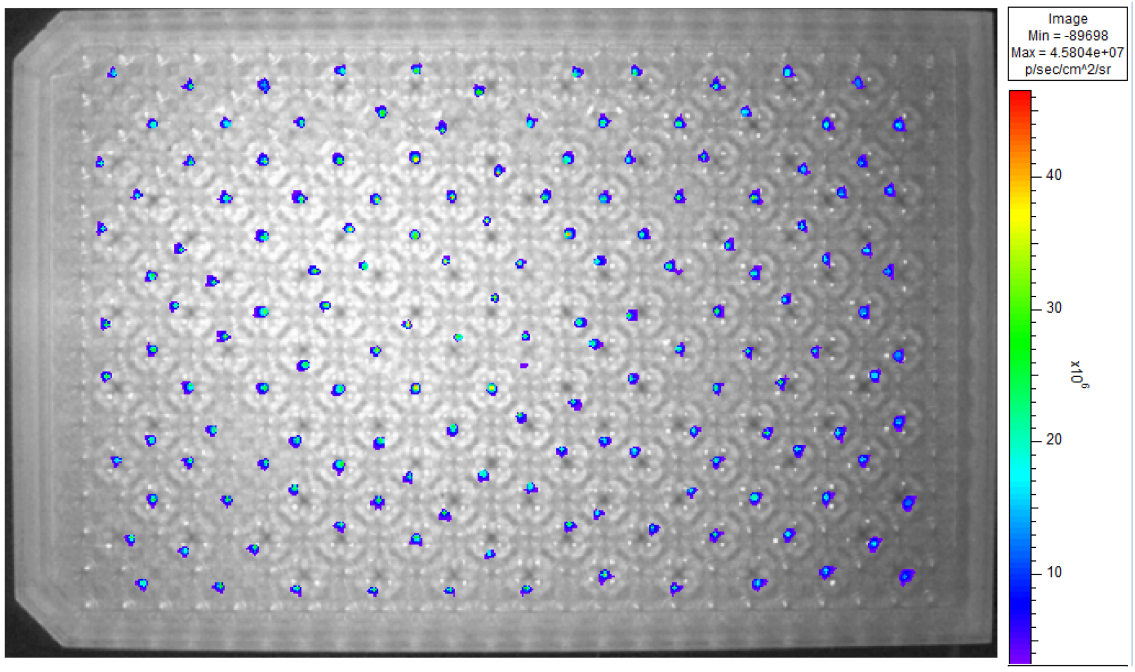

Figure B.1. Spheroid collection efficiency using bioluminescent imaging. For each spheroid we seeded at a ratio of 9:1 HMF cells and MDA-MB-231 cells expressing firefly luciferase for a total of 10,000 cells. Prior to transfer of spheroids we added 3 µl of luciferin diluted 4X in PBS to the TRIM plate. Only drops containing a spheroid and transferred to a well containing luciferin emit in detectable bioluminescence signal. We identified 154/154 spheroids seeded. Simultaneous mixing with luciferin at the time of transfer is advantageous for measurements of enzyme-substrate kinetics as compared to adding substrate to each well individually.

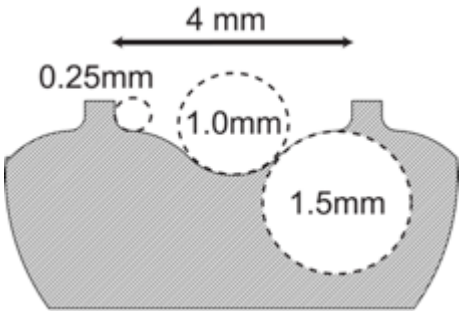

Figure B.2. Multi-radius well curvature and dimensions. Each well is 4 mm in diameter with a multi-radial (radii are noted) contour and a total depth of 1.75 mm. The radii are labeled adjacent to corresponding dashed circles.

Appendix C: Chapter 4 Supporting Information

9.1 Supplemental Figures

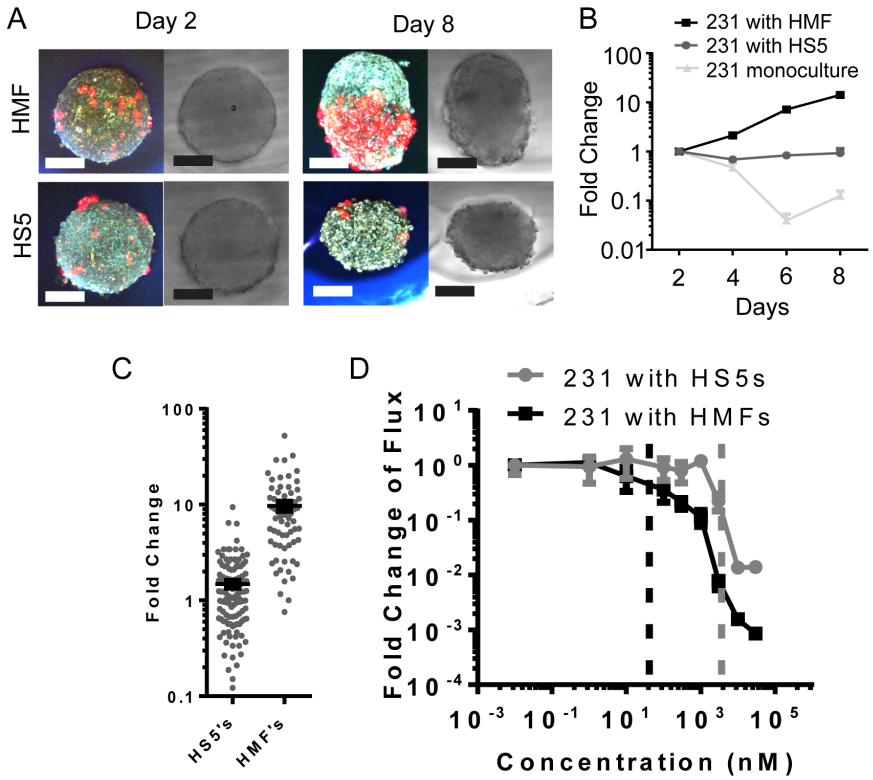

Figure C.1. Human mammary fibroblast induced growth differences change responsiveness to cytotoxic therapies. (A) Representative two photon fluorescence (left) and transmitted light (right) images of 1% MDA-MB-231 cells in either HMF (Top) or HS5 spheroids (Bottom) after 2 and 8 days of culture. The MDA-MB-231 cells express firefly luciferase and mCherry (red) and the HS5s and HMFs show up in green and blue channels due to NADH and FAD autofluorescence produced by 740nm excitation. (B) Bioluminescence time course expressed as fold change relative to day 2 reveals growth or quiescence of MDA-MB-231 cells. The graph shows mean values ± SEM for spheroids seeded initially with 30 cancer cells and 2,970 stromal cells (231 with HMF or HS5 cells) or cancer cells alone (231 monoculture) (n = 6 per time point and condition). (C) Aggregate fold change growth of MDA-MB-231 breast cancer cells based on bioluminescence from 16 and 9 independent experiments for co-culture spheroids with HS5 (N = 145) or HMF (n = 68 total), respectively, calculated on a per-spheroid basis. (D) Drug cytotoxicity curves for doxorubicin treatment of 1% MDA-MB-231 cells in HMF or HS5 spheroids. Graph shows mean values ± SEM for fold change in luciferase photon flux values from cancer cells. The grey and black dotted lines indicate IC_{50} values for MDA-MB-231 cells HS5 and HMF spheroids, respectively.

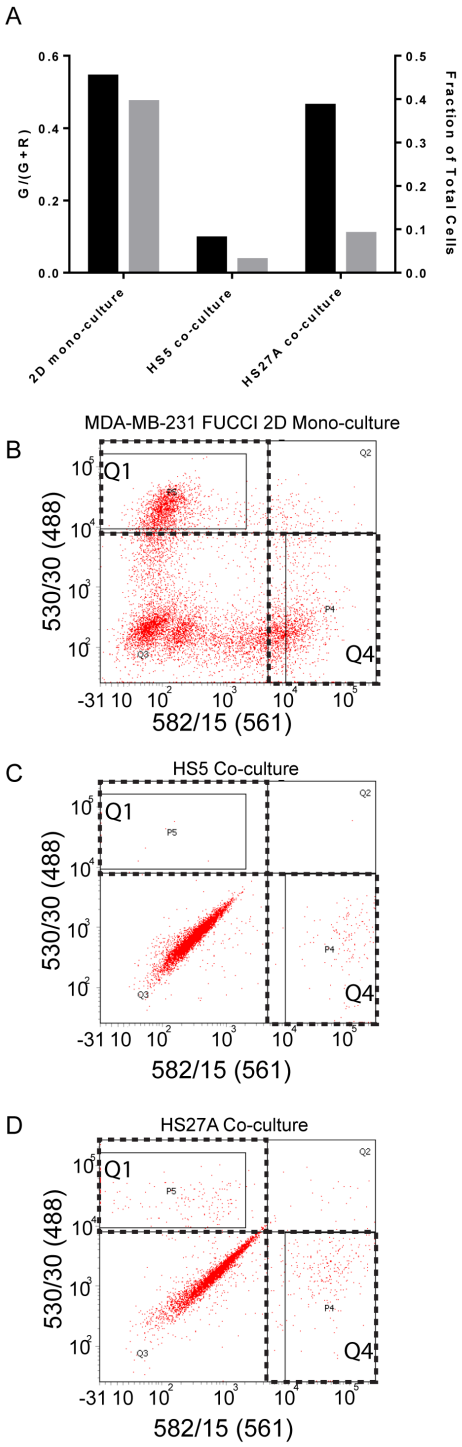

Figure C.2. Flow cytometry-based measure of FUCCI status of MDA-MB-231 cells in HS5 or HS27A spheroids. (A) The ratio of dividing cells (black, left axis), and the fraction of FUCCI+ cells out of total cells in spheroids (grey, right axis) were plotted after 4 days of culture in HS5 or HS27A spheroids. Monoculture MDA-MB-231 cells were plated 24 hours prior to analysis and collected at ~80% confluence to give a benchmark of actively dividing cells. The plot is depicted as the measurement from one experimental trial. We calculated the fraction of dividing cells as G/(G+R), where G is number of cells in Q1 (top left dotted box), and R is the number of cells in Q4 (bottom right dotted box) of the representative flow cytometry plots (B-D). We measured 1 x 10^4 events for each sample.

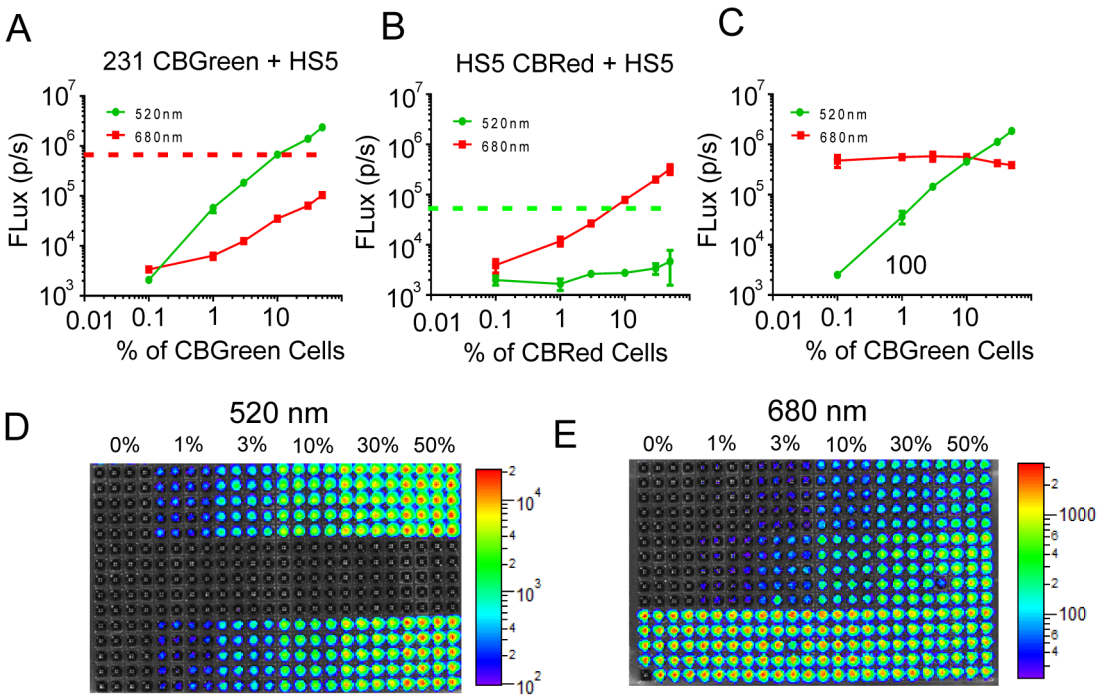

Figure C.3. Validation of dual-color luciferase imaging. (A) We plated an increasing percentage of MDA-MB-231 CBGreen cells with non-bioluminescent HS5 cells and quantified bioluminescence in green (520 nm) and red (680 nm) channels. Graphs in A-C show mean values with error bars smaller than the symbol when not evident (n = 20 per point). The red dashed line (A) shows the typical photon flux from CBRed HS5 cells when these cells are present at proportions (90-99% of cells) used in our spheroids. (C) Increasing the percentage of HS5 CBRed cells with unmarked HS5 cells increases signal in the red channel only. The green dotted line (B) shows approximately the average CBGreen photon flux when cancer cells are present at typical proportions (~1-10% of cells). At ratios of cancer to stromal cells used in bone marrow spheroids, bioluminescence from stromal cells is undetectable in the green channel, and cancer cells produce minimal signal in the red channel. (D) Bioluminescence from increasing percentages of CBGreen cells increases linearly with cell number, allowing sensitive detection of cancer cells without perturbing the constant CBRed signal from stromal cells. (F-G) representative 520nm and 680 nm images for the different proportions of cancer and stromal cells.

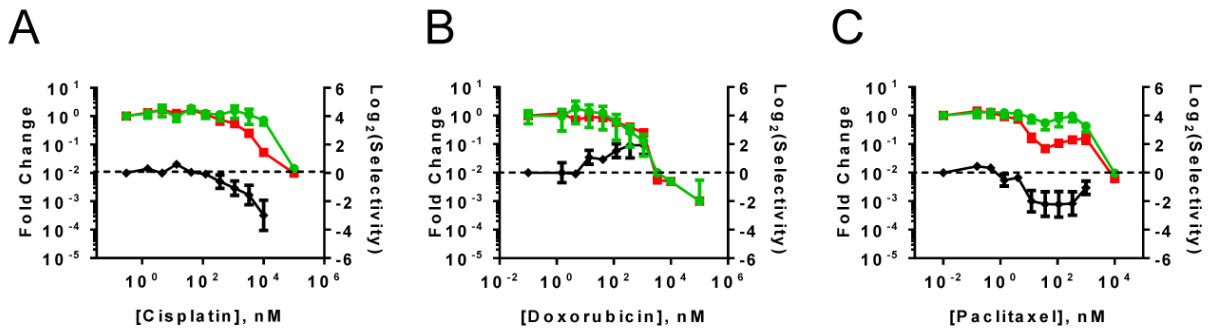

Figure C.4. Response of T47D and stromal cells to cytotoxic drugs. Dose-response cytotoxicity curves for T47D cells treated for eight days with cisplatin, doxorubicin, or paclitaxel in HS5 spheroids. Red curves designate CBRed HS5 signal, and green curves designate the CBGreen cancer cell signal, respectively. After background subtraction, we normalized photon flux values for both CBGreen and CBRed luciferases in cancer and stromal cells, respectively, to their respective untreated control. We calculate selective toxicity for cancer cells based on the log-2-scale ratio of CBRed to CBGreen signal adjusted to center around the untreated control (black curve). Positive values for selectivity (black curve) that lie above the horizontal dotted line denote selective loss of bioluminescence from cancer cells. We omit selectivity data points for conditions where CBRed and/or CBGreen signal is below 1% of untreated control since instrument noise generates most of the signal.

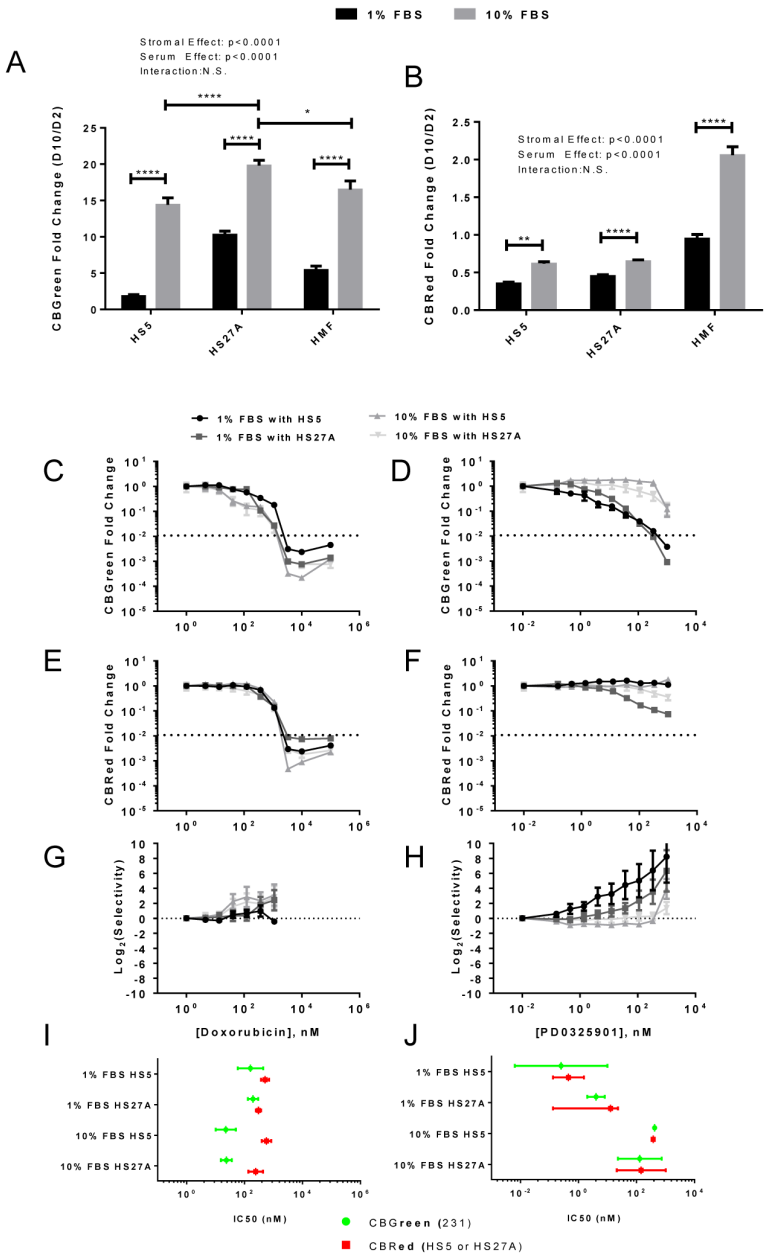

Figure C.5. Serum concentrations modulate, growth, drug efficacy, and selectivity of eliminating MDA-MB-231 cells in HS5 and HS27A spheroids. (A-B) Similar to Fig. 1A for MDA-MB-231 cells, we compared the CBGreen cancer (A) and CBRed stroma (B) fold change over 8 days. Inset text lists the main variable effects (stroma, serum, or their interactions) from 2-way ANOVA and bars demarcate the *post hoc* Tukey test results (* p <0.05, ** p<0.01, **** p<0.0001). Presented data are mean + SEM for n = 28 spheroids pooled from two independent setups. Doxorubicin (C,E,G) and PD0325901 (D,F,H) produce sigmoidal curves for MDA-MB-231 CBGreen cells (C-D) and stromal CBRed cells (E-F) after 8 days of drug treatment in HS5 or HS27A spheroids supplemented with 1 or 10% fetal bovine serum. With data from cancer and stroma dose response panels (C-E,D-F), we normalized data for graphs of selectivity of drugs (G,H) for cancer versus stromal cells as described in Figure S4. (I-J) We estimated the IC_{50} and 95% confidence intervals using four parameter non-linear regression for both cancer (green) and stromal (red) components for each serum condition. Note that lack of typical dose-response curve for 10% FBS in HS5 (J) led ambiguity of curve fit therefore we omitted the wide error bars.

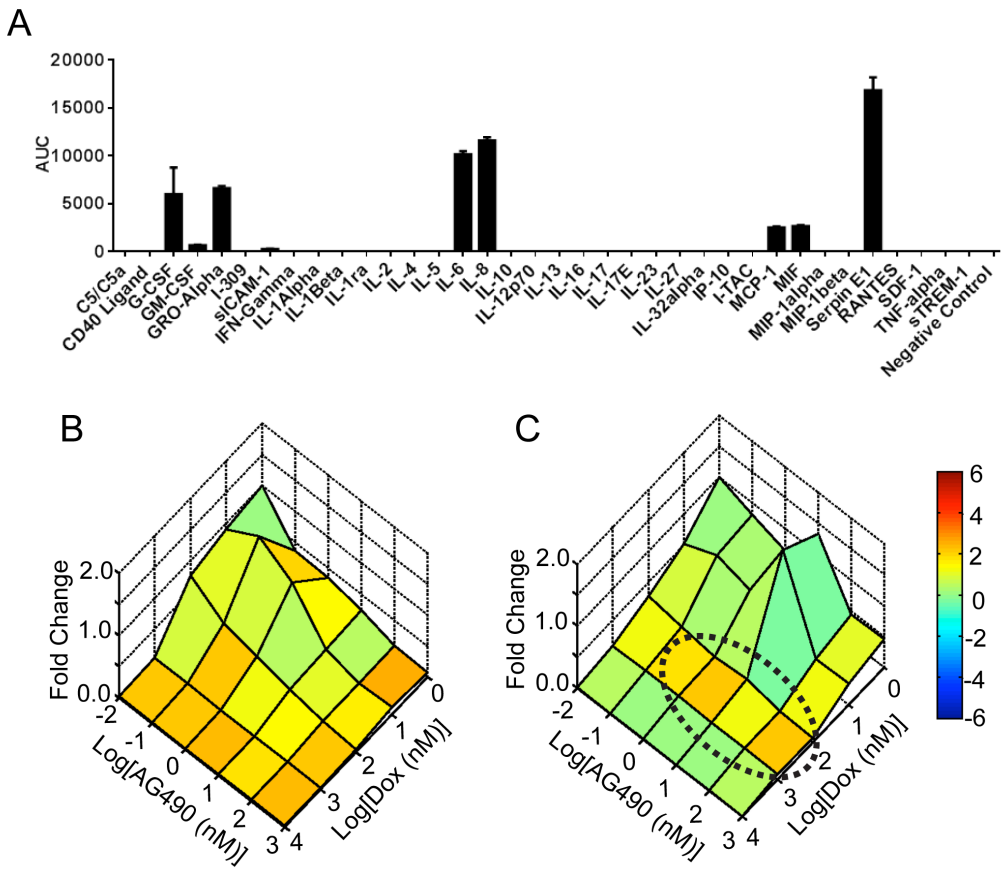

Figure C.6. Combinatorial treatment with doxorubicin and Jak2 kinase inhibitor to target cytokines produced by HS5 cells. (A) We quantified relative amounts of listed cytokines produced by HS5 cells after 24 hours in 2D culture with serum-free medium. We quantified values for signal intensity from each cytokine by area under the curve analysis (AUC) of the developed cytokine array. Values are from duplicate determinations for each molecule. (B-C) Surface plots display cancer cell bioluminescence (CBGreen) normalized to control after 8 days of treatment (B) and again after 6 days post-treatment recovery (C) for MDA-MB-231 cells treated with the Jak2 inhibitor AG490 and doxorubicin. Color-scale reflects log-2-scale selectivity in panels B-C with positive values (red colors) depicting preferential loss of bioluminescence from cancer cells relative to HS5 stromal cells. Combinations of AG490 and doxorubicin produce the highest post-recovery within the circled region in panel C.

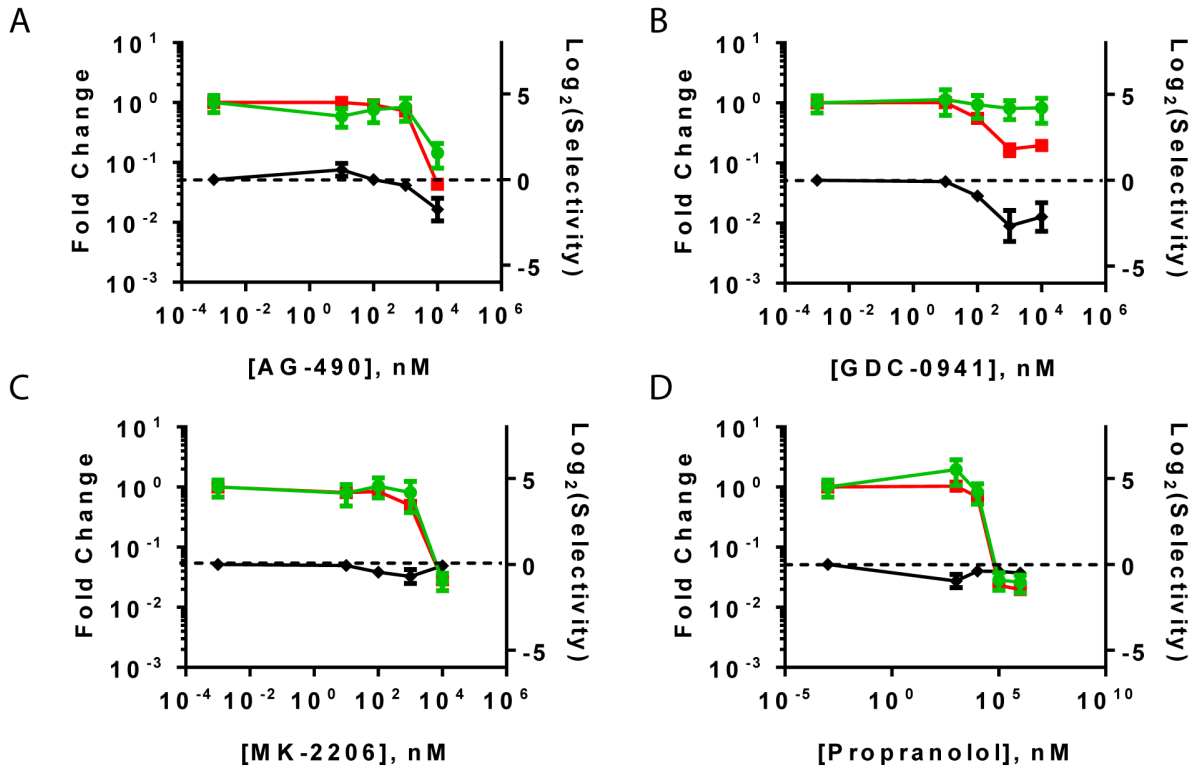

Figure C.7. Representative cytotoxicity curves for selective inhibitors of Jak2 (AG-490), PI3-kinase (GDC-0941), AKT (MK-2206), and β2-adrenergic receptor (propranolol) with MDA-MB-231 cells in HS5 spheroids. Graph shows mean values + SEM (n = 8 per condition) for fold change in bioluminescence from MDA-MB-231 cells (green curves) and HS5 cells (red curves). We calculated selectivity of compounds for cancer versus stromal cells as described in Fig C.4 (black curves) with positive values representing greater killing of cancer cells and negative selectivity values for greater killing of HS5 stromal cells.

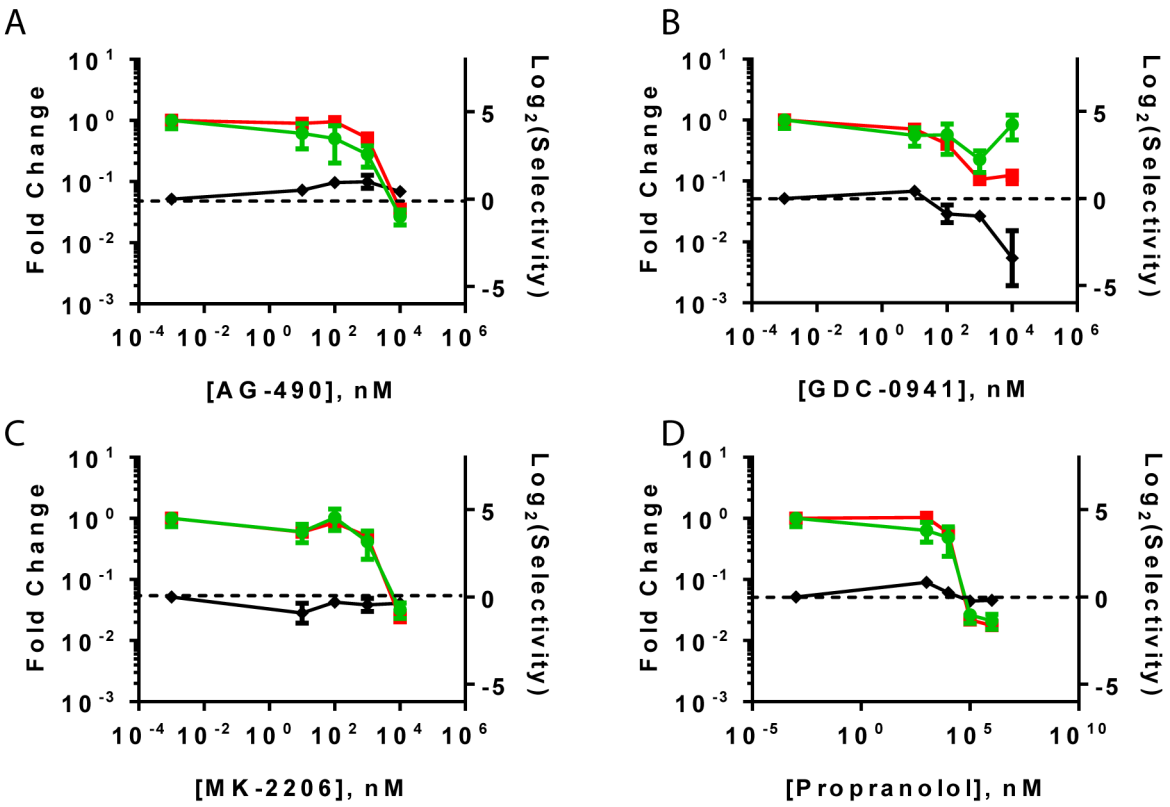

Figure C.8. Representative cytotoxicity curves for selective inhibitors of Jak2 (AG-490), PI3-kinase (GDC-0941), AKT (MK-2206), and β2-adrenergic receptor (propranolol) with T47D cells in HS5 spheroids. Graph shows mean values + SEM (n = 8 per condition) for fold change in bioluminescence from MDA-MB-231 cells (green curves) and HS5 cells (red curves). We calculated selectivity of drugs for cancer versus stromal cells as described in Fig C.4 (black curves) with positive values representing greater killing of cancer cells and negative selectivity values for greater killing of stromal cells.

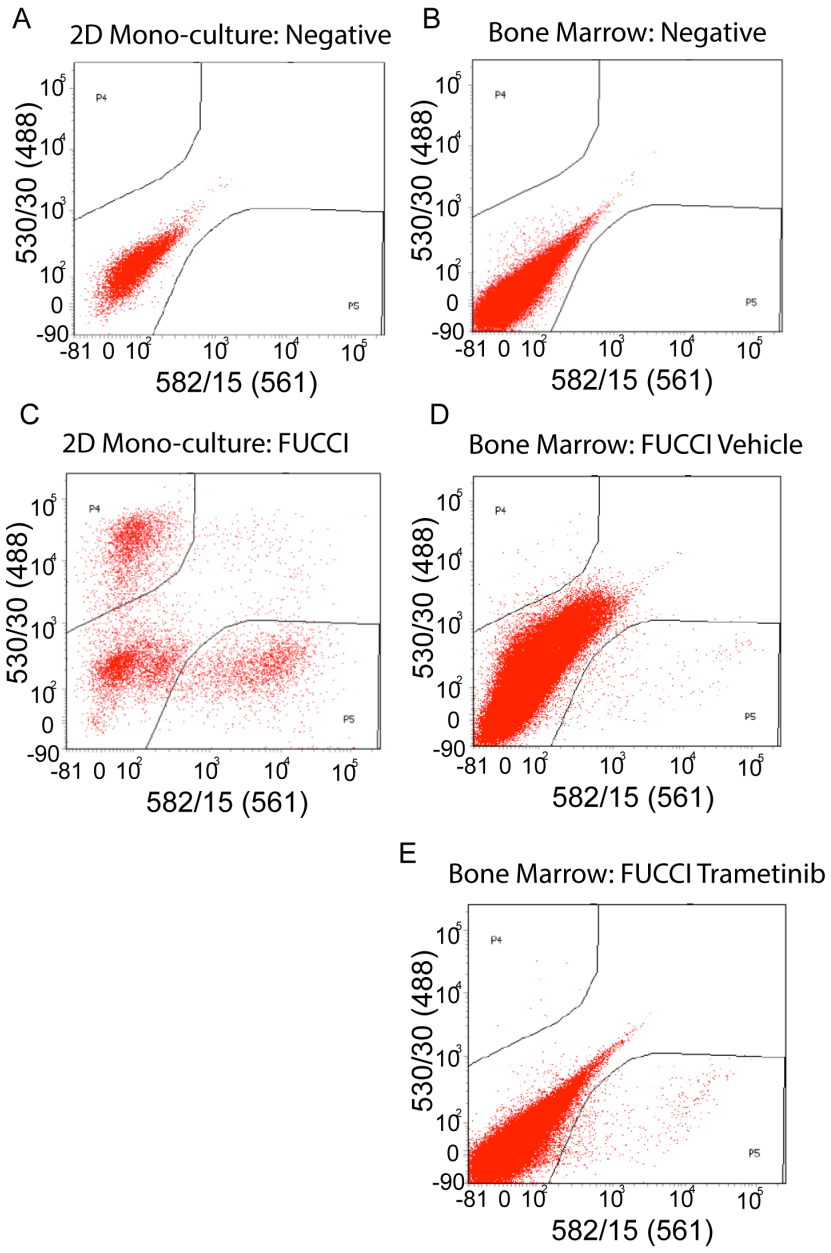

Figure C.9. Flow cytometry-based measure of FUCCI status of MDA-MB-231 cells in bone marrow of mice. Figure 4.5D represents flow cytometry data from mouse bone marrow. Representative negative control flow cytometry plots from unmarked (negative) MDA-MB-231 cells in 2D culture (A) and mouse bone marrow (B). (C) Representative flow cytometry plot of MDA-MB-231 FUCCI cells plated 24 hours prior and harvested at 80% confluence to give a benchmark of cell cycle status. Representative plots of bone marrow from vehicle treated (D) and trametinib treated (E) mice. In figure 4.5D, we calculated the fraction of dividing cells as G/(G+R), where G is number of cells in P4 (top left ROI), and R is the number of cells in P5 (bottom right ROI). We analyzed 5 x10^5 cell events for bone marrow samples. X and Y axes denote fluorescence from mKO (582/15 (561)) and AcGFP (530/30 (488)), respectively.

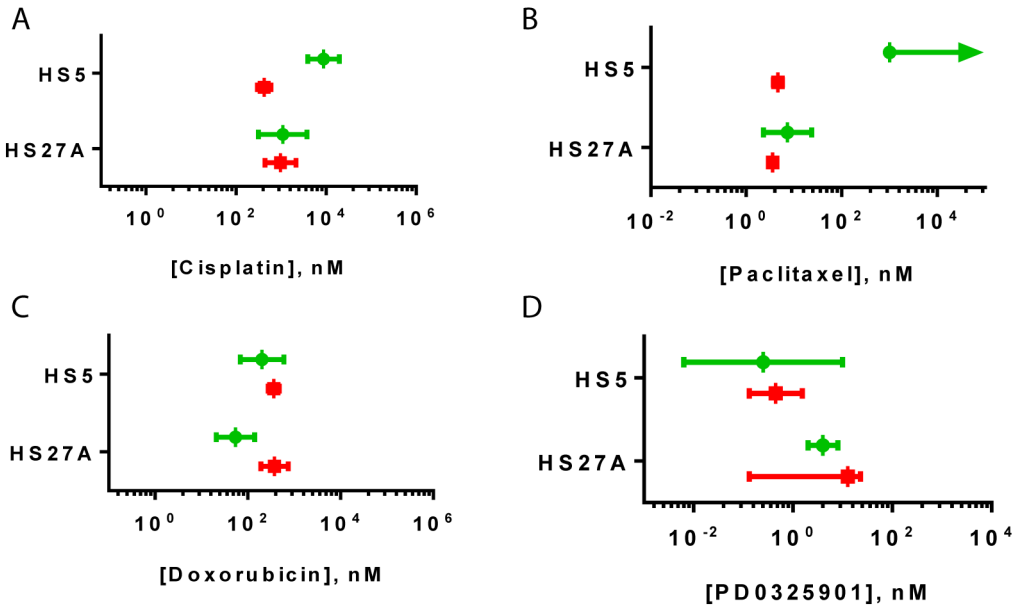

Figure C.10. Estimates for IC_{50} values for cytotoxic drugs and inhibition with PD0325901. (A-D) For both CBGreen (cancer - green) and CBRed (HS5 or HS27A - red) from Figure 4.3, we estimated the IC_{50} and 95% confidence intervals using four-parameter non-linear regression. Note that lack of typical dose-response curve for paclitaxel (B) led to ambiguity of the curve fit. Therefore, we omitted non-determined error bars and denoted an IC_{50} value of >1μM for MDA-MB-231 cells co-cultured with HS5 cells.

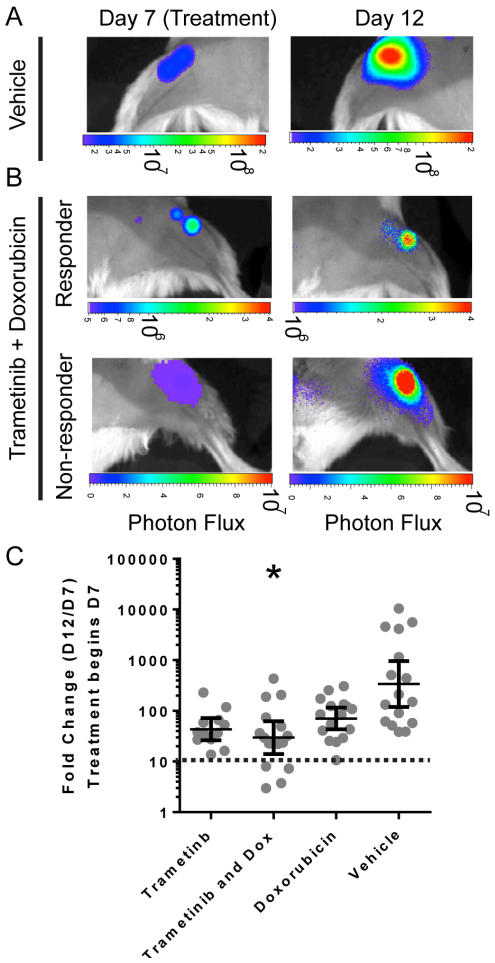

Figure C.11. Bioluminescence reveals improved treatment of breast cancer cells in bone marrow with combination doxorubicin and trametinib treatment. After visualizing experimental MDA-MB-231 bone metastases by bioluminescence imaging, we treated mice with a single dose of doxorubicin, 5 days of daily trametinib initiated on the same day as doxorubicin, both doxorubicin and trametinib, or vehicle controls. (A-B) Representative pseudo-colored bioluminescence images reveal the increased signal from the same bone regions at day 7 (left) and day 12 (right) for both vehicle (A) and (B) trametinib treated animals. The top and bottom pairs of images in panel B represent metastases responding or not-responding to treatment, respectively. Note that for each pair of images we changed the lower end of the log-scale to visualize the metastases similarly. (C) Bioluminescence measurements from matched femurs and tibias were compared between day 12 and the treatment day 7. Paired t-tests depict that only combination treatment with doxorubicin and trametinib caused a statistically significant decrease relative to the vehicle (* $p<0.05$). Dotted line demarcates lesions with < 10-fold change in signal over time, which occurred only in the combination doxorubicin and trametinib group. Individual data points are plotted with median for n = 12, 16, 16, 16 lower extremity segments (femur and tibia from each lower extremity per mouse), for trametinib, trametinib + doxorubicin, doxorubicin, and vehicle, respectively, with four lower extremity segments from each animal.

9.2 Supplemental Tables

Tables C.1-C.4 summarize effects of several different molecularly-targeted compounds for selective toxicity to MDA-MB-231 (C.1, C.3) or T47D cells (C.2, C.4) in HS5 bone marrow spheroids. We determined selectivity for toxicity to cancer versus stromal cells based on CBGreen and CBRed bioluminescence, respectively, as detailed in Figures 4.2 and C.6 after 8 days of treatment. Tables C.1-C.2 list compounds with minimal effects on either cancer or stromal cells at peak concentrations of at least 1 μM). Tables C.3-C.4 list compounds showing non-selective toxicity to both cancer and stromal cells or greater toxicity to stromal cells. Each table lists the compound and its molecular target.

Table C.1. Compounds with limited effect on MDA-MB-231 cells in HS5 spheroids (up to 1uM)

Compound	Target
Bazedoxifene	Estrogen receptor
Fulvestrant	Estrogen receptor
Tamoxifen	Estrogen receptor
MK-8669	mTOR
SB-431542	TGF-β
CP-724,714	Her2
AMD3100	CXCR4

Table C.2. Compounds with limited effect on T47D cells in HS5 spheroids (>1uM)

Compound	Target
Bazedoxifene	Estrogen receptor
Fulvestrant	Estrogen receptor
Tamoxifen	Estrogen receptor
PD0325901	MEK
MK-8669	mTOR
SB-431542	TGF-β
CP-724,714	Her2
AMD3100	CXCR4

Table C.3. Compounds with non-selective or negatively selective effects for MDA-MB-231 cells versus HS5 cells

Compound	Target	CBGReen	CBRed
AG-490	JAK2	>1uM	>1uM
GDC-0941	PI3-kinase	Limited	~100nM
MK-2206	AKT	>1uM	>1uM
Propanolol	B2 adrenergic receptors	>10uM	>10uM

Table C.4. Compounds with non-selective or negatively selective effects for T47D cells versus HS5 cells

Compound	Target	CBGReen	CBRed
AG-490	JAK2	>1uM	>1uM
GDC-0941	PI3-kinase	Limited	~100nM
MK-2206	AKT	>1uM	>1uM
Propanolol	B2 adrenergic receptors	>10uM	>10uM

Appendix D: Chapter 5 Supporting Information

10.1 Supplemental Figures

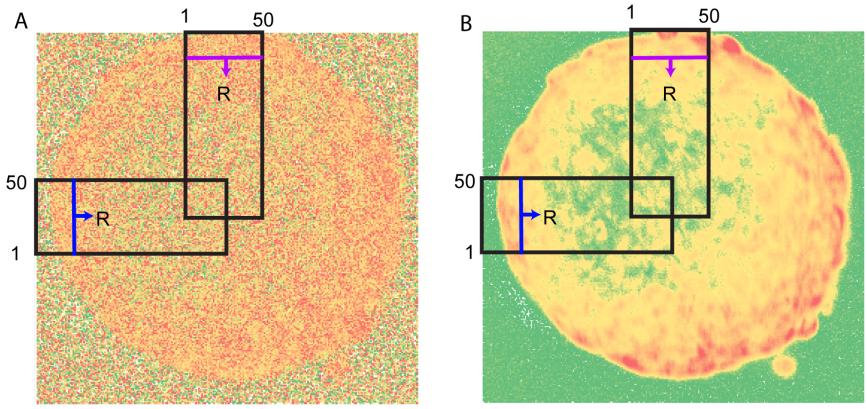

$$\phi_{NADH,R} = \frac{\sum_{i=1}^{50}(\phi_i * I_i)}{\sum_{i=1}^{50} I_i}$$

Figure D.1. Quantification of NADH phase lifetime through spheroid cross-sections. Representative spheroid profiles of color-coded (A) NADH phase lifetime and (B) photon counts. The black boxes represent one horizontal and vertical radial cross-section from this spheroid. For a given radial position, the blue and purple lines designate a 50 pixel vector of lifetimes and counts which we use to calculate a weighted average. For each radial position (R) the weighted average is calculated using the inset equation, for pixel numbers i=1 to 50. We then align spheroid edge positions and average the radial profiles from four locations on the spheroid for four spheroids to generate the radial lifetime profiles in Figures 5.2-5.3.

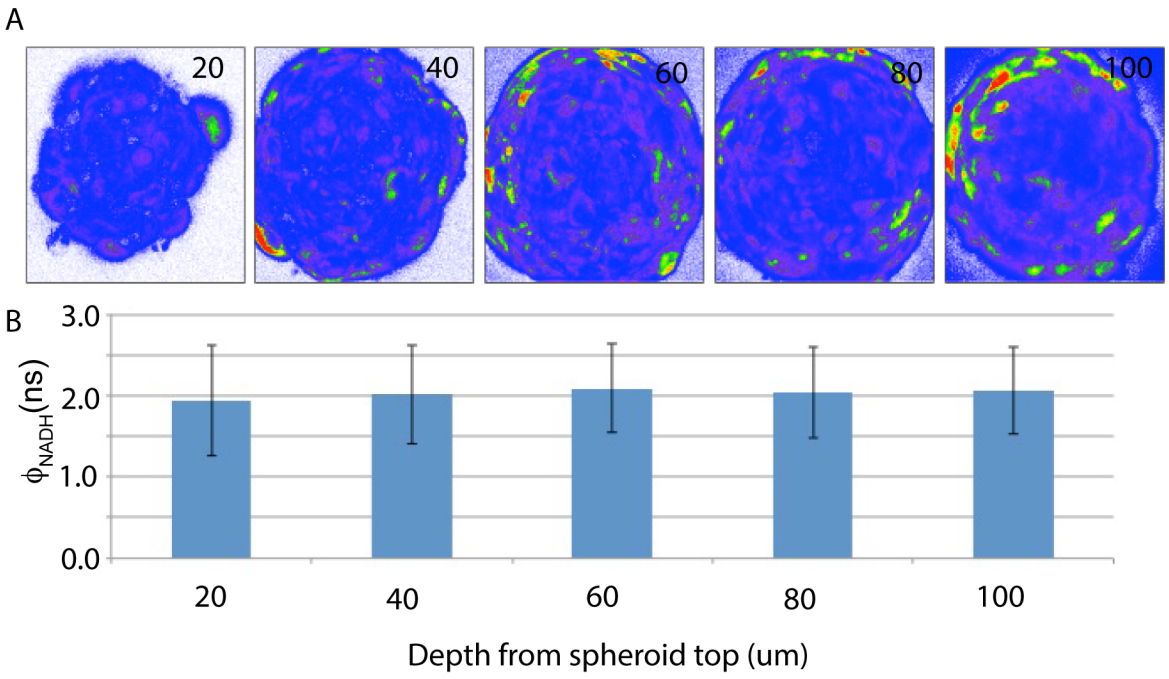

Figure D.2. Characterization of the lifetime-based metabolic imaging throughout depth of small mesenchymal stem cell spheroid. (A) Similar to Figure 5.2, we depict images of photon counts at 20, 40, 60, 80, and 100 μm depth for small, non-nutrient-limited MSC spheroids. (B) The average NADH phase lifetime was constant throughout the depth of the spheroids. NADH phase lifetimes are plotted as mean ± S.E.M. for a single cross-sections from four spheroids.

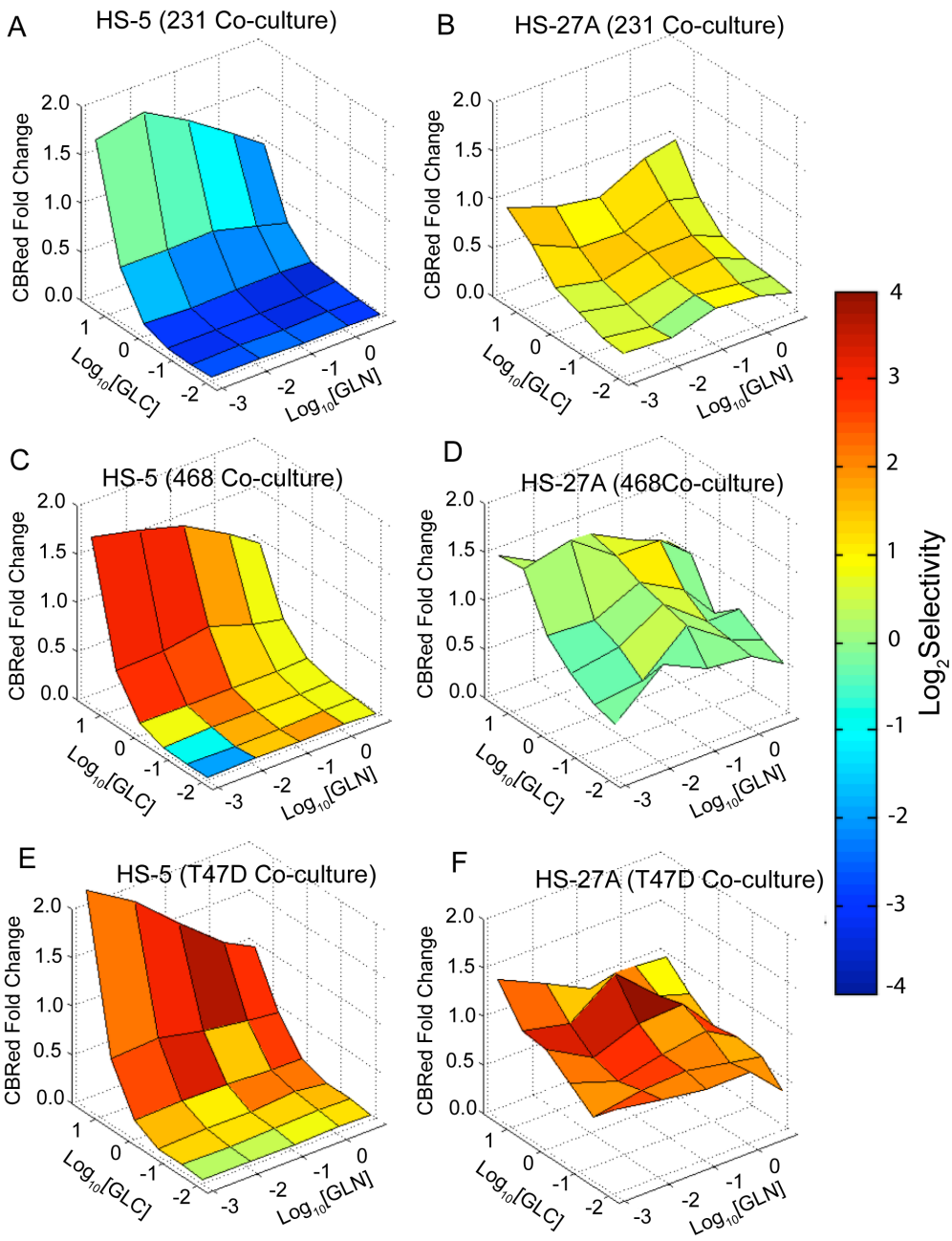

Figure D.3. Interdependence on glucose and glutamine for cancer and stromal cells in bone marrow spheroids. Similar to Figure 5.4, but for the CBRed component, We plotted combination dose-response surface plots of glucose and glutamine concentrations for CBRed signal from (A-B) MDA-MB-231, (C-D) MDA-MB-468, and (E-F) T47D cells grown in (A, C, E) HS-5 or (B, D, F) HS-27A spheroids. We plotted the CBRed fold change as compared to the high glucose and high glutamine concentration for both cancer and stromal cells. The plots are color-coded for log-2-scaled ratio of CBRed to CBGreen signal, both normalized to high glucose and high glutamine. Hot colors designate relatively lower cancer signal. In the dose-response surfaces, values are plotted as mean for 4 spheroids from one of two representative independent trials.

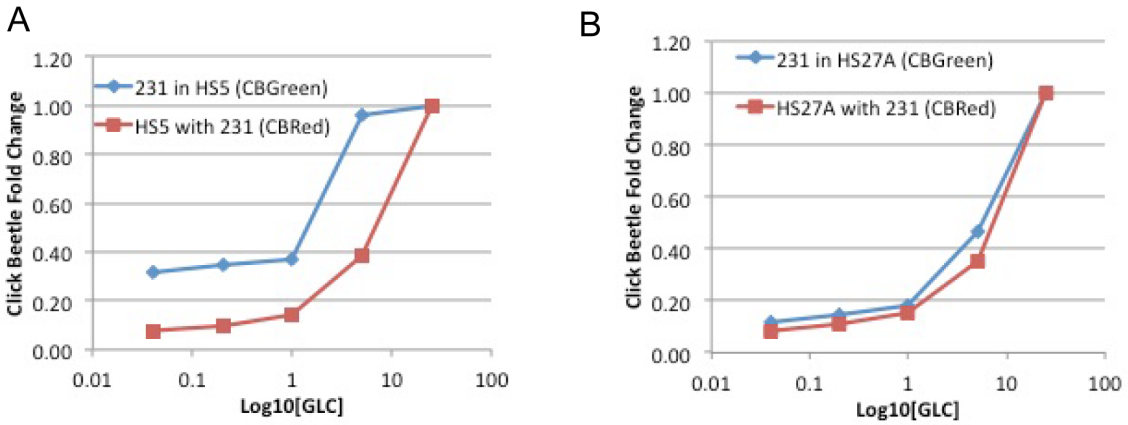

Figure D.4. Glucose and glutamine dependence of cancer and stromal cells. For direct comparison of glucose dose-response in HS-5 and HS-27A with maximal levels of glutamine, we plotted these curves together for CBGreen cancer and CBRed stromal signals for (A) HS-5 and (B) HS-27A co-cultures. Values are plotted as mean ± S.E.M. for 4 spheroids from one of two representative independent trials.